Engineering Optical Antenna for Efficient Local Field Enhancement

Tae Joon Seok

Electrical Engineering and Computer Sciences
University of California at Berkeley

Technical Report No. UCB/EECS-2013-190
http://www.eecs.berkeley.edu/Pubs/TechRpts/2013/EECS-2013-190.html

December 1, 2013

Engineering Optical Antenna for Efficient Local Field Enhancement

by

Tae Joon Seok

A dissertation submitted in partial satisfaction of the

requirements for the degree of

Doctor of Philosophy

in

Engineering – Electrical Engineering and Computer Sciences

in the

Graduate Division

of the

University of California, Berkeley

Committee in charge:

Professor Ming C. Wu
Professor Eli Yablonovitch
Professor Luke P. Lee

Fall 2012

The dissertation of Tae Joon Seok, titled Engineering Optical Antenna for Efficient Local Field Enhancement,
is approved:

Chair ____________________________________ Date ____________________

____________________________________ Date ____________________

____________________________________ Date ____________________

University of California, Berkeley

Engineering Optical Antenna for Efficient Local Field Enhancement

Abstract

Engineering Optical Antenna for Efficient Local Field Enhancement

by

Tae Joon Seok

Doctor of Philosophy in Engineering – Electrical Engineering and Computer Sciences

University of California, Berkeley

Professor Ming C. Wu, Chair

Optical antennas have been widely used for variety of applications such as sensitive photodetection, efficient light emission, high-resolution imaging, heat-assisted magnetic recording, and surface-enhanced Raman spectroscopy (SERS) because they can capture and focus propagating electromagnetic energy into sub-diffraction-limited areas and vice versa. However, widespread application of optical antennas has been limited due to lack of appropriate methods for uniform and large area fabrication of antennas, as well as difficulty in achieving an efficient design with small mode volume (gap spacing < 10nm).

In this dissertation, we theoretically derived the local field enhancement of the optical antenna and found that optimized radiation and small gap spacing are required for maximum field enhancement of the antenna. To address these parameters, we experimentally demonstrated three different designs of optical antennas.

First, we report on applying a dipole antenna on a ground plane for radiation engineering. The dipole antenna design can achieve the optimum radiation condition by tuning the spacer thickness between the antenna array and the ground plane; however, reducing the gap spacing below 10 nm is challenging if using typical nanofabrication techniques such as e-beam lithography and focused ion beam milling.

Secondly, we report on using a patch antenna on ground plane for the uniform sub-5 nm gap spacing. The patch antenna design can be easily implemented with extremely small gaps; however, the poor radiation efficiency of the patch antenna with a nanometer-scale gap degrades the performance of the antenna.

Finally, we present a novel optical antenna design—the arch-dipole antenna—which has optimal radiation efficiency and small gap spacing (5 nm) fabricated by CMOS-compatible deep-UV spacer lithography. This antenna design achieves a strong SERS signal with an enhancement factor exceeding 10^8 compared to the arch-dipole antenna array; this is two orders of magnitude stronger than that

obtained from the standard dipole antenna array fabricated by e-beam lithography. Because the antenna gap spacing—a critical dimension of the antenna—can be defined by deep-UV lithography, efficient optical antenna arrays with sub-10 nm gap can be mass-produced using current CMOS technology.

To my wife, Jung Hwa

TABLE OF CONTENTS

LIST OF FIGURES

ACKNOWLEDGMENTS

I would like to thank my advisor, Professor Ming C. Wu, for his continual mentorship and encouragement during the past years. I am heartily grateful to him for giving me the chance to be part of the integrated photonics laboratory (IPL). I would also like to thank Prof. Ture K. Gustafson, Prof. Luke P. Lee, and Prof. Eli Yablonovitch for serving on the committee in my qualifying exam and reviewing this dissertation.

I want to thank my current and former labmates at integrated photonics laboratory for their helpful discussions and suggestions. Especially, I would like to thank Dr. Arash Jamshidi for being a good colleague, a kind mentor, and a warm friend. I also want to thank Prof. Kyoungsik Yu, Dr. Myung-Ki Kim, Dr. Erwin Lau, Prof. Aaron Ohta, Dr. Steven Neale, Dr. Ming-chun (Jason) Tien, Dr. Justin Valley, Hsan-yin (Tony) Hsu, Dr. Amit Lakhani, Dr. John Wyrwas, Dr. Jeffery Chou, Karen Grutter, Anthony Yeh, Shao Ning Pei, Michael Eggleston, Alex Grine, Ryan Going, Dr. Niels Quack, Dr. Byung-wook Yoo, and Sang Yoon Han for their help and support. I would also like to thank Prof. Jeffrey Bokor, Prof. Ali Javey, Prof. Hyuck Choo, Prof. Min Hyung Lee, Dr. P. James Schuck, Dr. Stefano Cabrini, Dr. Adam M. Schwartzberg, Dr. Scott Dhuey, Dr. Wilbur A. Lam, Dr. Sun Choi, Maxwell Zhang for their helpful collaborations, and the UC Berkeley Marvel nanolab and Berkeley Sensor and Actuator Center (BSAC) staffs for their help and support. Finally, I want to acknowledge the entire optoelectronic group at Berkeley EECS, specifically, Roger Chen, Frank Rao, Dr. Chris Chase, Wilson Ko, James Ferrara, Billy Ng, Weijian Yang, Tianbo Sun, Vadim Karagodsky, Thai Tran, Devang Parekh, Nikhil Kumar, Dr. Matteo Staffaroni, Dr. Sapan Agarwal, and Dr. Owen Miller.

I would like to thank Samsung Scholarship, DARPA SERS Program for their generous funding. I would never have achieved my degree without their support.

I also want to thank my parents, my sister, and in-laws for their everlasting support. Finally, I would like to thank my wife, Jung Hwa, for her love and support. I could finish this long journey since she has been standing with me.

CHAPTER 1

Introduction

When a charged particle is placed in external electric field, the accelerated motion is induced. This remains true even if the charged particle scales down to an electron and the external field oscillates at high frequencies up to hundreds THz. This is a simplified explanation of what happens when light is illuminated on a metallic structure. The incident electromagnetic wave excites the collective oscillation of conduction electrons in the metal. The combined oscillation of conduction electrons and photons is called surface plasmon polariton (SPP). In general, the SPP is a propagating wave at the interface between metal and dielectric. When the metallic structure has a bound geometry such as a metal nanoparticle, however, the oscillating mode is localized and shows a resonant characteristic at a certain frequency; this is known as localized surface plasmon resonance (LSPR). The re-radiated (scattered) field from this LSPR interferes with the incident field, and the total field results in efficient light coupling, which can capture the incident power flux through a much greater cross section compared to the actual physical size of the metallic nano-structure.

This light-matter interaction within the metallic nano-structure breaks one of the main constraints of classical optics—the diffraction limit—and focuses light energy into sub-wavelength region at the surface of metal. As a result, nanometer-size regions with high local field enhancement are created (so-called hot spots). The small mode volume of LSPR can also significantly enhance the emission rate of an atom or a molecule placed at the high field region. Therefore, properly designed metallic nano-structures can efficiently capture and focus the far-field wave into the near field and vice versa. This is why they are called optical antennas.

Historically, the concept of the optical antenna was initiated from near-field optics using metal nanoparticles. In 1928, Synge suggested a method to improve the resolution of optical imaging using colloidal gold nanoparticles [1]. In 1985, Wessel proposed to use the optical-field confinement of a metal particle for an optical probe with spatial resolution unlimited by the diffraction [2]. He claimed for the first time that metal nanoparticles can serve as an antenna in the receiving mode. In the following years, many different ideas using metal nanoparticles or sharp metallic tips were suggested or experimentally demonstrated in near-field optical microscopy and spectroscopy [3]–[5].

The antenna theory at radio frequencies (RFs) had already been well-established before 1940 and developed even further during World War II. The optical antenna is just a counterpart of the radio frequency (RF) antenna at optical frequencies, and subsequently useful analogies were taken from the success of RF antenna theory. In 1968, whisker antennas were used in diodes for the detection of frequency mixing at infrared frequencies [6]. In the following years, theoretical and experimental research on analysis of the receiving properties of whisker antennas were published by Schwarz et al [7]–[9]. In 1976, Wang reported research that interpreted the metal-dielectric-metal bar as the dipole antenna at optical frequencies [10]. From then until today, many different optical antenna geometries that originated from RF antenna designs, such as dipole antennas [11]–[14], monopole antennas [15], [16], patch antennas [17] and Yagi-Uda antennas [18]–[20], have been reported.

Although these previous works established the foundation of this field and the various possible applications, such as sensitive photodetection [12], [21], efficient light emission [22]–[25], heat-assisted magnetic recording [26], high-resolution imaging [27]–[29], and bio-chemical sensing, have been reported [30]–[32], the practical use of optical antennas in real applications has not been realized because of a requirement for an antenna whose dimensions are smaller than currently available. A critical factor in the performance of an antenna is that it is highly dependent on its gap spacing; therefore, a small gap spacing is required for both a high local field enhancement and emission rate improvement of the emitter source. For the extremely small gap spacing, an optical antenna often consists of two metal nanoparticles with a nanometer-scale gap spacing. Therefore, optical antennas are typically fabricated using nano-fabrication technology such as electron-beam lithography and focused-ion beam milling.

However, the current resolution limit of these nano-fabrication techniques is limited by poor uniformity and reproducibility when the dimension of the gap spacing is reduced below 10 nm. Another critical obstacle preventing the practical applications of an optical antenna is the fabrication cost. Electron-beam lithography and focused-ion beam milling are slow and expensive serial writing processes, which require huge amounts of time and money proportional to the fabricated area. Therefore, mass-production capability by developing a new fabrication technique is essential to make the optical antenna as widespread a technology as the RF antenna.

Now, our question is obvious. How can we design an efficient optical antenna with a reliable fabrication method that also has the ability to “broadcast” to a suitably large-area? Answering this question will be the main goal and direction of this dissertation in the following pages.

At first, we will start with a review of the material properties of noble metals at optical frequencies. With this background, we will study basics of Plasmonics including surface plasmon polariton (SPP) mode at a planar metal-dielectric boundary and localized surface plasmon resonance (LSPR) in a spherical metal particle. Then, we will discuss the absorption and scattering by the metal nanoparticle. In Chapter 3, we will review antenna fundamentals, taking advantage of well-established RF antenna theory. Various antenna parameters and the antenna circuit model will be introduced here, which are also useful for performing optical antenna analysis. In Chapter 4, we will discuss the abilities of optical antennas to concentrate the local field by capturing the propagating light wave and accelerate the spontaneous decay rate of the emitter source placed at the high field region. Then, we will derive the local field enhancement as the critical design parameter for antenna performance and discuss the optimum conditions for the maximum field enhancement. In Chapter 5, we will introduce the gold dipole antenna array on the gold ground plane for radiation engineering. In this antenna design, the radiation of the optical antenna is engineered to be matched with the antenna absorption for optimized light coupling. In Chapter 6, we will discuss the patch antenna design for uniform and reproducible sub-5 nm antenna gap, and the trade-off between the radiation efficiency and small gap spacing. Finally, in Chapter 7, we will report a new antenna design, called the “arch-dipole antenna,” which provides both decent radiation efficiency and the uniform 5 nm gap spacing. We will present a reliable method for fabricating the arch-dipole antenna by using deep-UV spacer lithography. Surface-enhanced Raman scattering measurement from *trans*-1,2-bis (4-pyridyl) ethylene (BPE) molecules will be chosen to verify experimentally the performance specification of these novel antenna designs.

CHAPTER 2

Light-Matter Interaction by Metal Nanoparticles

When light illuminates on metal surface, it excites collective oscillations of conduction electrons. If the metal structure has an unbounded planar boundary, the excited mode propagates at the boundary of metal surface, which is known as surface plasmon polariton (SPP). On the other hand, if the metal structure has a certain shape and bound geometry such as a metal nanoparticle, the excited mode shows the resonant characteristics known as localized surface plasmon resonances (LSPRs). These surface modes have tightly confined field distributions near the metal surface, which enables light focusing beyond its diffraction limit. In addition, the induced current in the metallic particle results in the scattering (or re-radiation) of light. This scattered field interferes with the incident field and the incident power, and, as a result, is captured through the much greater cross section than the physical size of the metal nanoparticle.

In this chapter, we will first review the material properties of noble metals at optical frequencies. Then, we will discuss plasmonic modes at the metal surface and its characteristics. Finally, we will review the light coupling mechanism of metal nanoparticles by scattering and absorption.

2.1 Material Properties of Metals at Optical Frequencies

2.1.1 Drude-Sommerfeld Model

In order to investigate the optical properties of noble metals, we first consider free electrons. The physical behavior of free-electron gas can be described by Drude-Sommerfeld model, where the equation of motion for a free electron is given by

$$m\frac{\partial^2 \vec{r}}{\partial t^2} + m\Gamma\frac{\partial \vec{r}}{\partial t} = e\vec{E}e^{-i\omega t} \qquad (2.1)$$

where m, e, and Γ represent the effective mass, the charge, and the damping coefficient of the free electron, respectively, and E and ω are the amplitude and the frequency of the applied electric field. If we solve Eq. (2.1) using $\vec{r}(t) = \vec{r}_0 e^{-i\omega t}$, then $\vec{r}_0$ is given by

$$\vec{r}_0 = -\frac{e\vec{E}}{m(\omega^2 + i\Gamma\omega)} \qquad (2.2)$$

Then, the macroscopic polarization can be expressed as

$$\vec{P} = \varepsilon_0 \chi_e \vec{E} = ne\vec{r}_0 = -\frac{ne^2\vec{E}}{m(\omega^2 + i\Gamma\omega)} \tag{2.3}$$

where n is the number of electrons per unit volume. Finally, the dielectric constant is given by

$$\varepsilon_{Drude}(\omega) = 1 + \chi_e = 1 - \frac{\omega_p^2}{\omega^2 + i\Gamma\omega} \tag{2.4}$$

where $\omega_p = \sqrt{ne^2/(m\varepsilon_0)}$ is the plasma frequency. The dielectric constant can be dived into the real and imaginary terms as

$$\varepsilon_{Drude}(\omega) = 1 - \frac{\omega_p^2}{\omega^2 + \Gamma^2} + i\frac{\Gamma\omega_p^2}{\omega(\omega^2 + \Gamma^2)} \tag{2.5}$$

The dielectric constants of some noble metals at optical frequencies are plotted in Fig. 2.1. We can see that the real part of the dielectric constant is negative, which results in a small penetration depth of light into metal since the negative dielectric constant provides the imaginary part of the refractive index. The imaginary part of the dielectric constant contributes to the dissipation of the energy in the metal.

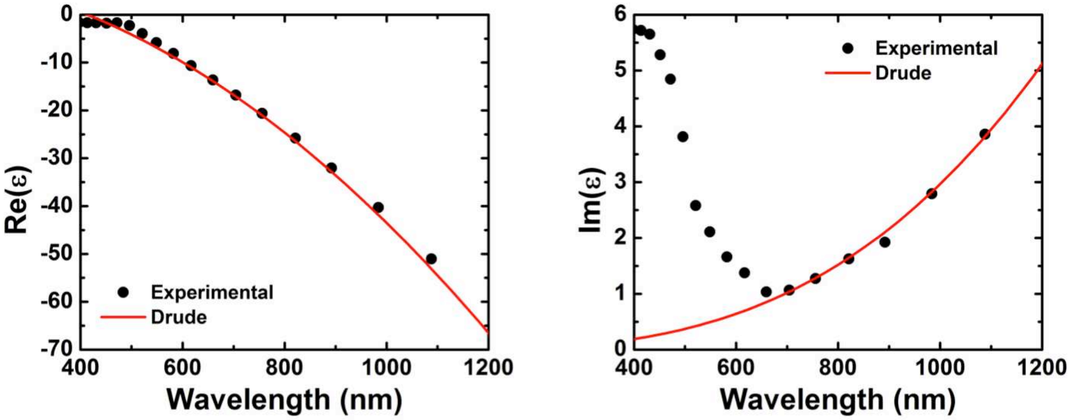

Figure 2.1 Dielectric constant of gold from Drude Model. Experimental values are taken from Ref. [33].

2.1.2 Lorentz-Drude Model

As shown in Fig. 2.1, the Drude-Sommerfeld model demonstrates the discrepancy with the experimental data at visible frequencies, although it provides accurate results at infrared frequencies. This is because the Drude-Sommerfeld model is based on free electrons, ignoring the response of bound electrons. For the case of gold, a significant jump of imaginary part of the dielectric constant exists at a wavelength shorter than 550 nm. This is due to the interband transition, which is the excitation of bound electrons to conduction electrons. Therefore, we need to introduce a new model that includes the effect of bound electrons. In the Lorentz-Drude model, the equation of motion for a bound electron is given by

$$m\frac{\partial^2\vec{r}}{\partial t^2} + m\gamma\frac{\partial\vec{r}}{\partial t} + \alpha\vec{r} = e\vec{E}e^{-i\omega t} \qquad (2.6)$$

where m is the effective mass of the bound electron, γ is the damping constant, and α is the spring constant of the bound electron. Here we find that the contribution of bound electrons to the dielectric constant becomes

$$\varepsilon_{Lorentz}(\omega) = \frac{\Omega_p^2}{(\omega_0^2 - \omega^2) - i\gamma\omega} \qquad (2.7)$$

where $\Omega_p = \sqrt{ne^2/(m\varepsilon_0)}$ (with n being the number of bound electrons per unit volume), and ω_0 is the natural frequency of bound electrons ($\omega_0 = \sqrt{\alpha/m}$). Then, the entire dielectric function from Lorentz-Drude model is expressed as

$$\varepsilon_{Drude}(\omega) = \varepsilon_\infty - \frac{\omega_p^2}{\omega^2 + i\Gamma\omega} + \Omega_p^2 \sum_{j=1} \frac{f_j}{\left(\omega_j^2 - \omega^2\right) - i\gamma_j\omega} \qquad (2.8)$$

Here, the multiple interband transitions are added with the oscillator strength f_j, and the constant offset ε_∞ is introduced instead of 1 for better fit to the experimental value. The dielectric constants of the Lorentz-Drude model are plotted in Fig. 2.2 with the contribution of a single interband transition. We can see that the Lorentz-Drude model gives more accurate results at the visible range for the real and imaginary parts of the dielectric constants.

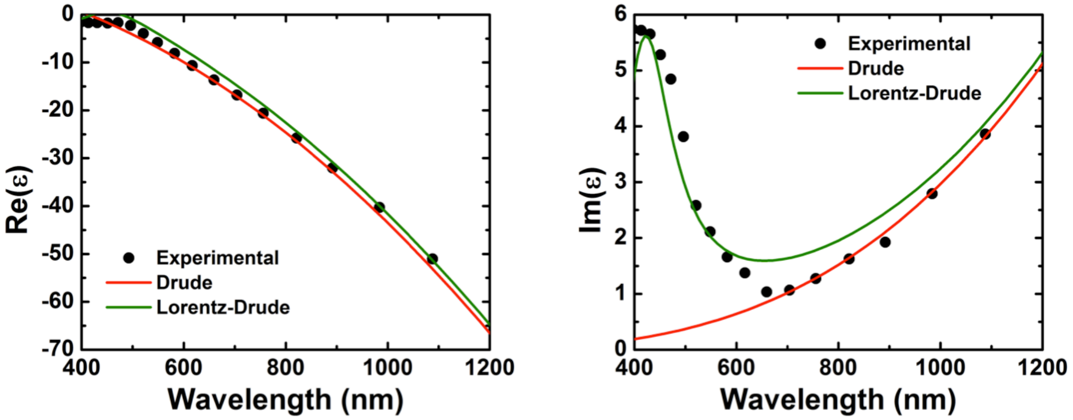

Figure 2.2 Dielectric constant of gold from Lorentz-Drude Model. Experimental values are taken from Ref. [33].

2.2 Surface Plasmon

2.2.1 Surface Plasmon Polariton at Planar Interface

When the electromagnetic wave is incident on the metal surface, collective oscillations of conduction electrons are excited and travel through the boundary of the metal surface. Because this propagating wave is coupled with the incident electromagnetic wave, it is called surface plasmon polariton (SPP). For the simplest geometry of surface plasmon, we consider a planar interface between the metal and dielectric. Figure 2.3(a) shows the schematic of SPP.

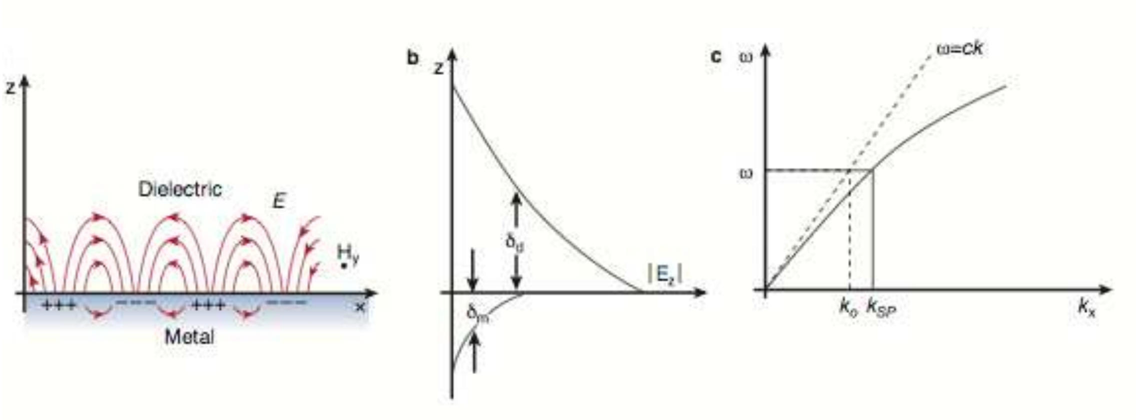

Figure 2.3 Surface plasmon polariton. a, Schematic of surface plasmon polariton. **b,** Electric field mode profile. **c,** Dispersion relation of surface plasmon polariton [34].

To find the eigenmode of the given structure, we need to solve Maxwell's equation, which for this system are given by

$$\nabla \cdot \vec{D} = 0 \tag{2.9}$$

$$\nabla \cdot \vec{B} = 0 \tag{2.10}$$

$$\nabla \times \vec{E} = -\frac{\partial \vec{B}}{\partial t} \tag{2.11}$$

$$\nabla \times \vec{H} = \frac{\partial \vec{D}}{\partial t} \tag{2.12}$$

Here, the oscillating current from conduction electrons is implied in the complex value of dielectric constant. Applying a curl operator to Eq. (2.11) and combining Eqs. (2.11) and (2.12), we obtain the wave equation, which is expressed as

$$\nabla\times\nabla\times\vec{E}=-\frac{\partial\left(\nabla\times\vec{B}\right)}{\partial t}=-\frac{\mu\varepsilon}{c^2}\frac{\partial^2\vec{E}}{\partial t^2} \tag{2.13}$$

$$\therefore\ \nabla\times\nabla\times\vec{E}-\frac{\omega^2}{c^2}\mu\varepsilon\vec{E}=0 \tag{2.14}$$

where $\vec{E}(\vec{r},t)=\vec{E}(\vec{r},\omega)e^{-i\omega t}$ is used to simplify Eq. (2.13) to Eq, (2.14). Here, the value of relative permeability μ is assumed to be 1 at optical frequencies. The guided mode at the boundary of two media propagates along the x-direction, and decays evanescently in the z-direction. First, we consider transverse magnetic (TM) wave for the solutions for the electric and magnetic fields. TM waves in half-spaces can be expressed as

$$\vec{E}=\begin{pmatrix}E_{j,x}\\0\\E_{j,z}\end{pmatrix}e^{ik_xx-i\omega t}e^{ik_{j,z}z} \tag{2.15}$$

where the subscript j indicates the medium 1 or 2 (dielectric, $z > 0$ or metal, $z < 0$). The wave vector components must follow the relation as

$$k_x^2+k_{j,z}^2=\varepsilon_j k_0^2 \tag{2.16}$$

where k_0 is the wave vector at free space ($k_0=2\pi/\lambda$). Then, we have to match the fields at the interface using boundary conditions. The boundary conditions of continuous tangential component of E and continuous perpendicular component of D give the following relations

$$E_{1,x}-E_{2,x}=0 \tag{2.17}$$

$$\varepsilon_1E_{1,z}-\varepsilon_2E_{2,z}=-\varepsilon_1\frac{k_x}{k_{1,z}}E_{1,x}+\varepsilon_2\frac{k_x}{k_{2,z}}E_{2,x}=0 \tag{2.18}$$

To obtain non-trivial solutions from Eqs. (2.17) and (2.18), the determinant of coefficient matrix must vanish; the relation is then defined as

$$\frac{k_{1,z}}{\varepsilon_1}-\frac{k_{2,z}}{\varepsilon_2}=0 \tag{2.19}$$

Combining Eqs. (2.16) and (2.19), the dispersion relation between the propagation wave vector k_x and the frequency ω is given by

$$k_x=k_0\sqrt{\frac{\varepsilon_1\varepsilon_2}{\varepsilon_1+\varepsilon_2}} \tag{2.20}$$

and we find the normal component of the wave vector k_z as

$$k_{j,z}=k_0\sqrt{\frac{\varepsilon_j^2}{\varepsilon_1+\varepsilon_2}} \tag{2.21}$$

Therefore, the electromagnetic field is strongly confined in the z-direction as shown in Fig. 2.3(b) if the normal component of the wave vector given in Eq. (2.21) has a large imaginary value. A typical dispersion relation of surface plasmon is also plotted in Fig. 2.3(c).

From Eqs. (2.20) and (2.21) we can extract the conditions that must be satisfied to have a guided mode at the interface. For simplicity, we assume that the imaginary part of the dielectric constant is negligible compared to the real part. In order to have a propagating mode along the interface, the propagation constant must have a real component. This is achieved when the sum and the product of the dielectric constants from Eq. (2.20) are either both positive or both negative. To include a bound mode at the interface, the normal component of the wave vector must be imaginary in both media. This requires that the sum of the dielectric constants from Eq. (2.21) must be negative Therefore, we can conclude that the conditions for surface plasmon mode are given by

$$\varepsilon_1(\omega) + \varepsilon_2(\omega) < 0 \tag{2.22}$$

$$\varepsilon_1(\omega) \cdot \varepsilon_2(\omega) < 0 \tag{2.23}$$

Note that the dielectric constants must be negative for one and positive for the other one, and the magnitude of the negative one must be greater than that of the other one. As shown in the previous section, the dielectric constants of noble metals have large negative real parts. Consequently, SPP can exist at the interface between a noble metal and a dielectric.

We derived the dispersion relation and the conditions for the mode existence from TM wave. A similar approach can be done using a transverse electric (TE) wave, however, the conditions for the bound mode cannot be satisfied since the relative magnetic permeability has the value of 1 for both the metal and the dielectric at optical frequencies. Therefore, the mode solution for the TE wave does not exist.

Surface plasmon propagation can be also achieved from multi-layer systems such as insulator-metal-insulator (IMI), metal-insulator-metal (MIM), and so on. The discussion in detail for multi-layer surface plasmon mode can be found in Refs. [35]–[37].

2.2.2 Localized Surface Plasmon Resonance of Spherical Particle

In the previous section, we discussed surface plasmon at the planar interface between the metal and the dielectric where the electromagnetic field is strongly confined in the direction normal to the boundary. In the real applications of nano-optics such as optical antennas, however, the field confinement is achieved in two or three dimensions by a metallic nanostructure. In this section, we will discuss the localized surface plasmon resonance with an example of a spherical particle. Figure 2.4 shows the schematic of spherical particle of radius *a* and the electric field profile of gold spherical particle with plane wave excitation.

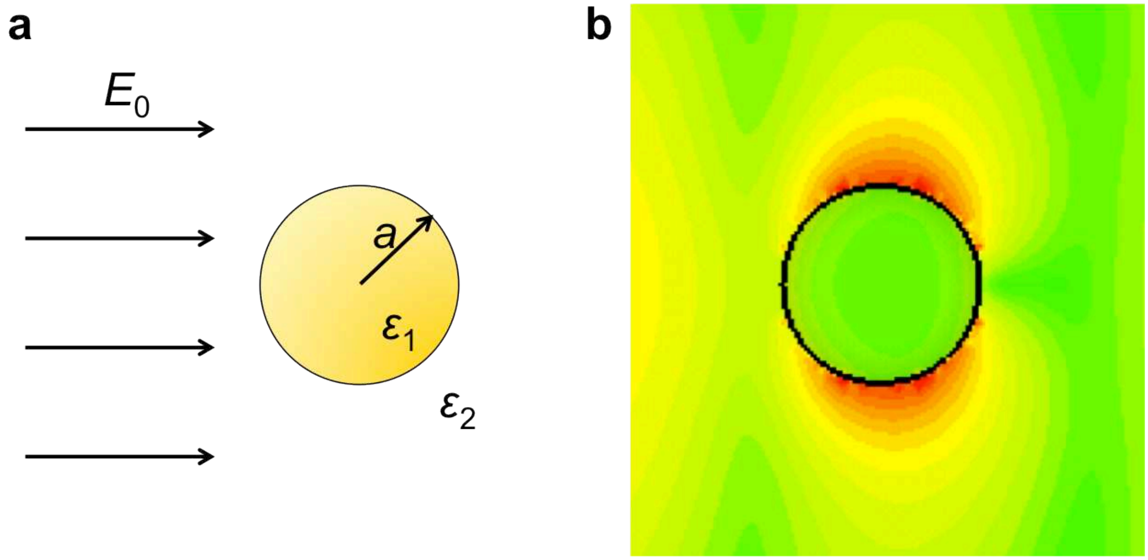

Figure 2.4 Localized surface plasmon of spherical particle. a, Schematic of spherical particle with plane wave excitation. **b,** Magnitude distribution of confined electric field.

In order to find the plasmon resonance for the spherical particle, we start with the Laplace equation of potential in spherical coordinates.

$$\frac{1}{r^2\sin\theta}\left[\sin\theta\frac{\partial}{\partial r}\left(r^2\frac{\partial}{\partial r}\right)+\frac{\partial}{\partial\theta}\left(\sin\theta\frac{\partial}{\partial\theta}\right)+\frac{1}{\sin\theta}\frac{\partial^2}{\partial\varphi^2}\right]\Phi(r,\theta,\varphi)=0 \tag{2.24}$$

The solutions are given by

$$\Phi(r,\theta,\varphi)=\sum_{l,m}b_{l,m}\Phi_{l,m}(r,\theta,\varphi) \tag{2.25}$$

where $b_{l,m}$ are constant coefficients, and $\Phi_{l,m}$ are of the form

$$\Phi_{l,m}=\begin{Bmatrix} r^{l} \\ r^{-l-1}\end{Bmatrix}\begin{Bmatrix} P_l^m(\cos\theta) \\ Q_l^m(\cos\theta)\end{Bmatrix}\begin{Bmatrix} e^{im\varphi} \\ e^{-im\varphi}\end{Bmatrix} \tag{2.26}$$

And where $P_l^m(\cos\theta)$ and $Q_l^m(\cos\theta)$ are the Legendre functions of the first and second order. For the boundary conditions, the continuity of tangential electric fields and the normal electric displacements at the surface of the sphere require that

$$\left[\frac{\partial\Phi_1}{\partial\theta}\right]_{r=a}=\left[\frac{\partial\Phi_2}{\partial\theta}\right]_{r=a} \tag{2.27}$$

$$\varepsilon_1\left[\frac{\partial\Phi_1}{\partial r}\right]_{r=a}=\varepsilon_2\left[\frac{\partial\Phi_2}{\partial\theta}\right]_{r=a} \tag{2.28}$$

where Φ_1 is the potential inside the sphere, and Φ_2 is the potential outside the sphere. The outside potential consists of the potentials of the incident and scattered fields ($\Phi_2 = \Phi_0 + \Phi_{scat}$). Assuming the incident plane wave of electric field E_0 and applying the boundary conditions, the solutions for potentials are given by

$$\Phi_1 = -E_0 \frac{3\varepsilon_2}{\varepsilon_1 + 2\varepsilon_2} r \cos\theta \tag{2.29}$$

$$\Phi_2 = -E_0 r \cos\theta + E_0 \frac{\varepsilon_1 - \varepsilon_2}{\varepsilon_1 + 2\varepsilon_2} a^3 \frac{\cos\theta}{r^2} \tag{2.30}$$

Then, the electric fields can be calculated from $\vec{E} = -\nabla\Phi$ to be

$$\mathrm{E}_1 = E_0 \frac{3\varepsilon_2}{\varepsilon_1 + 2\varepsilon_2} (\cos\theta\, \hat{n}_r - \sin\theta\, \hat{n}_\theta) \tag{2.31}$$

$$\mathrm{E}_2 = E_0(\cos\theta\, \hat{n}_r - \sin\theta\, \hat{n}_\theta) + E_0 \frac{\varepsilon_1 - \varepsilon_2}{\varepsilon_1 + 2\varepsilon_2} \frac{a^3}{r^3} (2\cos\theta\, \hat{n}_r + \sin\theta\, \hat{n}_\theta) \tag{2.32}$$

We can see that the first term in Eq. (2.32) is the incident field $E_0\hat{n}_x$,and the second term represents the scattered field. Note that this quasi-static approach is valid only when the size of the particle is smaller than the skin depth of the metal. The simulated field profile of the gold spherical particle in air is shown in Fig. 2.4(b), which confirms that the strong electric field is confined at the surface of the gold particle.

Once we know the scattered fields, we can calculate the scattered power and the scattering cross section. By definition [38], the scattering cross section is given by

$$\sigma_{sca} = \frac{P_{scat}}{I_0} = \frac{k^4}{6\pi\varepsilon_0^2} |\alpha(\omega)|^2 \tag{2.33}$$

where $\alpha(\omega)$ is the polarizability of the sphere, and I_0 is the power density of the incident light, which is

$$\alpha(\omega) = 4\pi\varepsilon_0 a^3 \frac{\varepsilon_1(\omega) - \varepsilon_2}{\varepsilon_1(\omega) + 2\varepsilon_2} \tag{2.34}$$

The absorption cross section is calculated from the dissipated power by the sphere and can be written as

$$\sigma_{abs} = \frac{P_{abs}}{I_0} = \frac{k}{\varepsilon_0} \mathrm{Im}[\alpha(\omega)] \tag{2.35}$$

The extinction refers to the power removed from the incoming beam due to the presence of a particle. The extinction cross section is the sum of the scattering cross section and the absorption cross section, which is given by

$$\sigma_{ext} = \sigma_{sca} + \sigma_{abs} = \left\{\frac{8}{3}(ka)^4 \left|\frac{\varepsilon_1(\omega) - \varepsilon_2}{\varepsilon_1(\omega) + 2\varepsilon_2}\right|^2 + 4(ka)\,\mathrm{Im}\left[\frac{\varepsilon_1(\omega) - \varepsilon_2}{\varepsilon_1(\omega) + 2\varepsilon_2}\right]\right\} \cdot \pi a^2 \quad (2.36)$$

Note that the scattering cross section is proportional to $(ka)^4$, whereas the absorption cross section is proportional to ka. Therefore, extinction is dominated by absorption if the particle size is much smaller than the wavelength ($ka << 1$), and scattering contributes significantly to extinction for a large particle. The term πa^2 is the physical cross section of the sphere with radius a. The extinction cross section of the sphere can be much greater than its physical cross section when $-\varepsilon_1$ approaches to $2\varepsilon_2$. This implies that the small scattering particle can interact with light very efficiently at resonance. The detailed discussion about cross sections will follow in the next section.

2.3 Interaction between Light and Metal Nanoparticle

At the end of the previous section, we discussed the scattering and the absorption of small spherical particles. In general, metal nanoparticles of any shape can also interact with light. In a physical picture, the scattering can be understood as the re-radiation due to the induced current in the metal particle by incident light and the scattered (or re-radiated) fields interfere with the incident fields. As a result, some amount of power is removed from incident wave through scattering and absorption; this is called extinction [39]. In this section, we discuss the general relation of the scattering and the absorption from the electromagnetic field theory. As a starting point, consider light scattering by a metal particle of an arbitrary geometry as shown in Fig. 2.5.

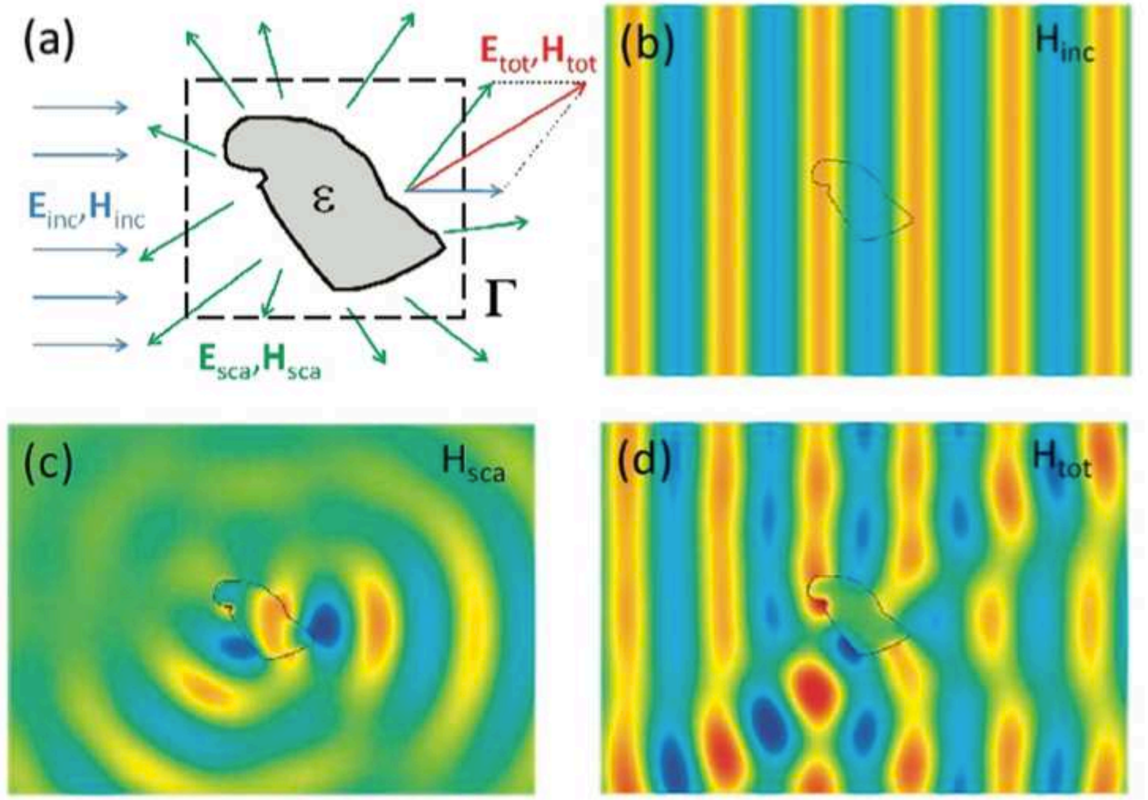

Figure 2.5 Scattering of light by a metal nanoparticle. a, Schematic of scattering process by a metal nanoparticle. **b-d,** Simulated incident, scattered, and total magnetic fields [40].

We assume that the plane wave of electromagnetic fields E_{inc} and H_{inc} is incident on the metal nanoparticle, and the scattered fields by the particle are represented by E_{sca} and H_{sca}. Then, we can find the total fields as the sum of the incident and scattered fields, which are expressed as

$$\vec{E}_{tot} = \vec{E}_{inc} + \vec{E}_{sca} \tag{2.37}$$

$$\vec{H}_{tot} = \vec{H}_{inc} + \vec{H}_{sca} \tag{2.38}$$

The power density flow of the electromagnetic wave can be obtained from the Poynting vector of total fields, which is given by

$$\begin{aligned} \vec{S}_{tot} &= \frac{1}{2}\mathrm{Re}\{\vec{E}_{tot}\times\vec{H}_{tot}^{*}\} \\ &= \frac{1}{2}\mathrm{Re}\{(\vec{E}_{inc}+\vec{E}_{sca})\times(\vec{H}_{inc}+\vec{H}_{sca})^{*}\} \end{aligned} \tag{2.39}$$

$$= \frac{1}{2}\mathrm{Re}\{\vec{E}_{inc}\times\vec{H}_{inc}^{*}\} + \frac{1}{2}\mathrm{Re}\{\vec{E}_{sca}\times\vec{H}_{sca}^{*}\}$$
$$+ \frac{1}{2}\mathrm{Re}\{\vec{E}_{inc}\times\vec{H}_{sca}^{*} + \vec{E}_{sca}\times\vec{H}_{inc}^{*}\}$$
$$= \vec{S}_{inc} + \vec{S}_{sca} + \vec{S}_{ext}$$

where $\vec{S}_{inc} = {}^{1}/_{2}\,\mathrm{Re}\{\vec{E}_{inc}\times\vec{H}_{inc}^{*}\}$ and $\vec{S}_{sca} = {}^{1}/_{2}\,\mathrm{Re}\{\vec{E}_{inc}\times\vec{H}_{inc}^{*}\}$ are the time-averaged Poynting vectors of the incident and scattered waves, and $\vec{S}_{ext} = {}^{1}/_{2}\,\mathrm{Re}\{\vec{E}_{inc}\times\vec{H}_{sca}^{*} + \vec{E}_{sca}\times\vec{H}_{inc}^{*}\}$ corresponds to the electromagnetic power density due to the interference of the incident and scattered fields.

In order to find the relation for the different energy channels, we integrate Eq. (2.39) on any closed surface, Γ, which contains the metal nanoparticle.

$$\oiint \vec{S}_{tot}\cdot d\vec{s} = \oiint \vec{S}_{inc}\cdot d\vec{s} + \oiint \vec{S}_{sca}\cdot d\vec{s} + \oiint \vec{S}_{ext}\cdot d\vec{s} \qquad (2.40)$$

In Eq. (2.40), the term on left-handed side becomes the dissipated power by absorption ($\oiint \vec{S}_{tot}\cdot d\vec{s} = -P_{abs}$), and the term $\oiint \vec{S}_{inc}\cdot d\vec{s}$ becomes zero because the incoming light is a plane wave. The power scattered by the particle is given by $\oiint \vec{S}_{sca}\cdot d\vec{s} = P_{sca}$, and the interference term in the scattering process ($\oiint \vec{S}_{ext}\cdot d\vec{s} = -P_{ext}$). shows the power as extinct. Therefore, we rewrite Eq. (2.40) as

$$P_{ext} = P_{sca} + P_{abs} \qquad (2.41)$$

Again, we confirm that P_{ext} corresponds to the total power extinct from the incident wave by scattering and absorption.

The concept of effective cross sections is often used to consider the power dissipations in different channels. An effective cross section is defined as the ratio of the dissipated power to the power density of the incident wave. Therefore,

$$\sigma_{sca} = P_{sca}/I_0 \qquad (2.42)$$

$$\sigma_{abs} = P_{abs}/I_0 \qquad (2.43)$$

$$\sigma_{ext} = P_{ext}/I_0 \qquad (2.44)$$

where I_0 is the power density of the incident wave ($= |\vec{S}_{inc}|$). Using Eq. (2.41), we define the relation between effective cross sections as

$$\sigma_{ext} = \sigma_{sca} + \sigma_{abs} \qquad (2.45)$$

In order to increase the coupling of light for a metal nanoparticle, large cross sections are required. Because the interaction of light and a metal particle is basically the result of interference phenomenon between the incident and scattered wave, the large cross sections of a metal particle (or an optical antenna) must be designed so that the radiation pattern to be spatially are well-matched with the incident wave. In general, the spatial mode matching requires the expression of electromagnetic fields and integration of two modes at the entire coupling region. However, if the incident illumination is a plane wave, the effective cross section can be introduced by incorporating the concept of directivity in antenna theory. As shown in the Chapter 3, the effective cross sections are proportional to the directivity of the antenna.

CHAPTER 3

Antenna Fundamentals

With the great success of (RF antennas, comprehensive antenna theory has successfully explained both theoretically and experimentally how an antenna works [41]–[43]. Although optical antennas have several distinctions, e.g., such as optical material properties, types of attached loads or generators, their physical behavior based on quantum electrodynamics (QED) regime, and so on, their light-matter interaction still relies on the identical physical mechanism: antennas radiate (or capture) electromagnetic wave from excited (or induced) current distribution. Therefore, aspects of RF antenna theory can be used to understand radiation and absorption characteristics of an optical antenna.

This chapter reviews the fundamentals of antenna theory. First, we will briefly take a look at the overview of antennas. Secondly, we will introduce key parameters that define the characteristics necessary for antenna. Finally, we will discuss the antenna circuit models for transmitting and receiving modes.

3.1 Overviews of Antenna

3.1.1 Antenna Radiation and Retardation Effect

The physics of antenna radiation can be understood as the result of retardation effect, which happens when the circuit elements have comparable sizes with the wavelength [44]. When we consider low frequencies, the circuit elements usually have much smaller dimensions than the wavelength. Then, the propagation time from one part of the circuit element to another is negligible. Figure 3.1 illustrates an example of a loop antenna. At low frequencies, the distance between point A and B is so small in comparison with wavelength, that the phase delay due to the travelling for the magnetic field by current element at point A to point B is insignificant. Then, the induced field from time-varying magnetic field is 90 degrees out of phase with current in B, which results in the inductive effect without power dissipation. At high frequencies, however, the loop dimension becomes comparable to wavelength, and the phase delay due to the propagation of magnetic field from point A to B cannot be ignored. The retarded magnetic field induces the electric field, which is not exactly 90 degrees out of phase with the current at B. This in-phase component of the induced field contributes to the power dissipation, which corresponds to the radiated power by the antenna.

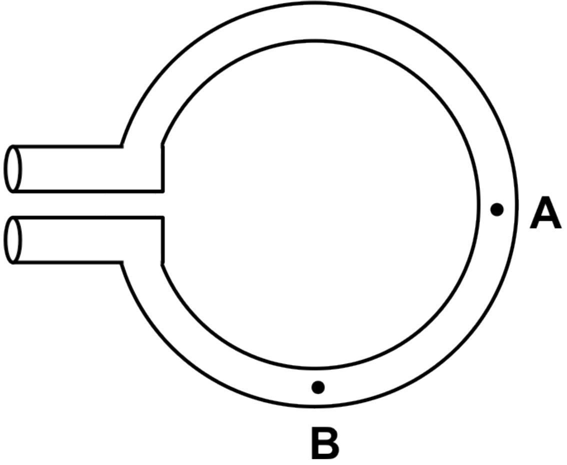

Figure 3.6 Retardation effect in loop antenna. Phase retardation is occurred between current at A and induced field at B when antenna size is comparable with wavelength.

If the distribution of current in circuit is known, fields and power radiated by the circuit can be calculated. From the relation between the radiated power and the current at the terminals of radiating part (the antenna part), the power dissipation by radiation can be expressed by a resistive term in the circuit. This is called radiation resistance. (A detailed discussion about radiation resistance will be addressed in a later section.) In reality, in order to obtain the actual current distribution, calculation of the radiation resistance is required to solve the boundary-value problem; it is sometimes difficult to obtain the exact analytical solution. Therefore, reasonable assumptions for current distributions are often used to calculate radiation characteristics. The assumed distribution depends on the shape and relative size to wavelength of antennas. For examples, a triangular current distribution is assumed for a small dipole antenna and a sinusoidal current distribution for a half-wave dipole antenna.

3.1.2 Categories of Antennas

Essentially, an antenna is a device that transfers energy propagation between guided waves and free-space waves. By reciprocity, an antenna can be used in both the transmitting mode and receiving mode; however, it is usually required to optimize antenna performance parameters. Unfortunately, the performance of antenna cannot be significantly improved without sacrificing other performance parameters. A detailed description of the antenna performance parameters will be discussed below. Here, we will introduce various types of antennas categorized by specific characteristics. Though there are several ways to classify antennas, e.g., according to their applications and technologies, here we categorize antennas into two separate classes.

The first classification is by spatial radiation characteristics of antennas. According to their angular radiation pattern, antennas are generally in one of two categories: omnidirectional and directional antennas. Omnidirectional antennas radiate (or receive) more or less in all directions, whereas directional antenna radiate (or receive) preferentially in a particular direction. Therefore, it is important to know the radiation pattern of an antenna to distinguish how a specific antenna operates. Omnidirectional antennas have merits for broadcasting systems that to send signals through broadside directions at low frequencies since a directional antenna at these frequencies would be too large and not cost effective. Directional antennas, which usually have better gain and are preferred when transmitting (or receiving) directions, are relatively preferred in applications for point-to-point communications. Figure 3.2 shows some examples of omnidirectional and directional antennas.

a. Omnidirectional Antennas

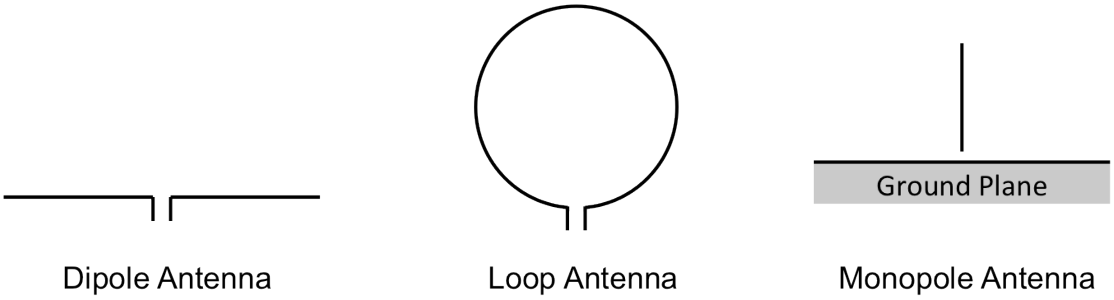

b. Directional Antennas

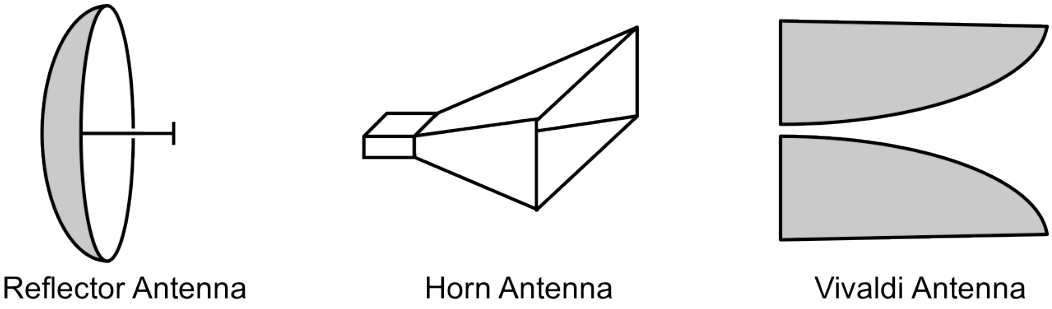

Figure 3.7 Omnidirectional and directional antennas. a, Omnidirectional antennas. **b,** Directional antennas.

Antennas also can be categorized by their spectral radiation characteristics. The bandwidth of antenna is defined as the range of frequencies over which important performance parameters are acceptable. Resonant antennas have good input impedance and radiation properties over a narrow band of frequencies. In general, resonant antennas have low to moderate gains and broad radiation patterns. In contrast, broadband antennas have acceptable radiation characteristics over a 2:1 bandwidth ratio of upper to lower operating frequencies. Broadband antennas are preferred when applications demand that they operate over a wide range of frequencies. Various types of resonant and broadband antennas are shown in Fig. 3.3.

a. Resonant Antennas

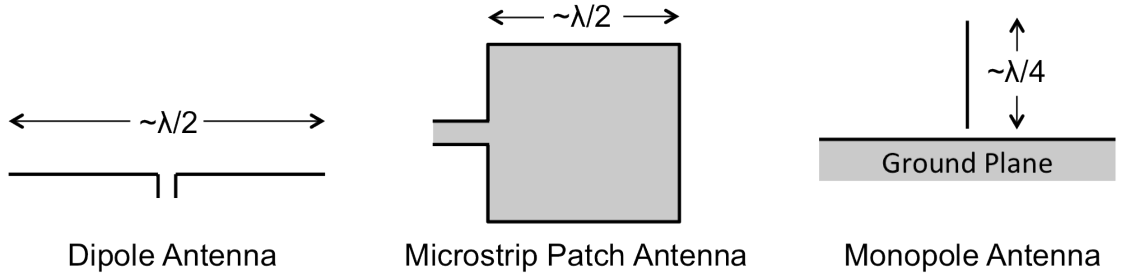

b. Broadband Antennas

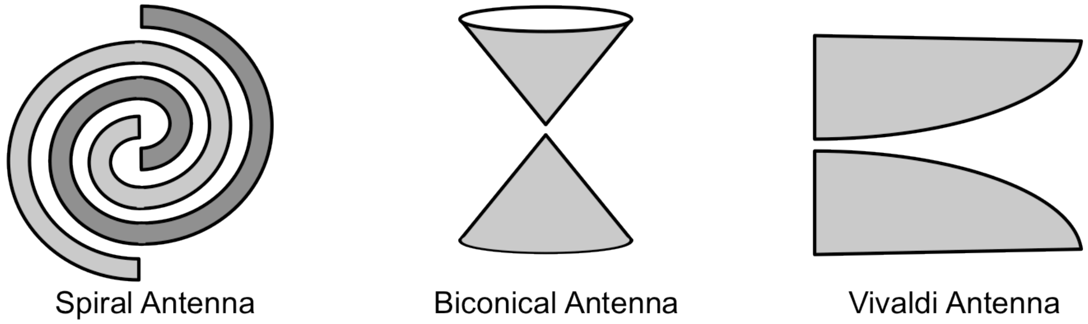

Figure 3.8 Resonant and broadband antennas. a, Resonant antennas. **b,** Broadband antennas.

Because there are trade-offs between antenna parameters, improving one parameter, in general, requires sacrificing one or more other parameters. For example, if one wants to increase the gain of antenna, it reduces the isotropy of radiation pattern by enhanced directivity. For example, broadband antennas are made with combined linear elements or continuously varying geometry to cover a wide operating bandwidth. However, since only a portion of a broadband antenna contributes for radiation at a given frequency, the efficiency of the antenna is low. Therefore, these limitations are an important consideration when designing an antenna for specific applications. Most applications of optical antennas are based on their abilities to concentrated light into the nanoscale region and/or enhancing the emission rate of the adjacent emitter. Therefore, the high gain and efficiency are, in general, preferred key design parameters. In following sections, antenna performance parameters will be discussed in detail.

3.2 Antenna Performance Parameters

3.2.1 Radiation Pattern

A radiation pattern refers to a directional dependence of the strength of the radiated waves. Since radiation pattern is the far-field property of antenna, a spherical coordinate is used to represent the angular distribution of the radiated field or power. Because the radiated field is inversely proportional to the distance ($1/r$), the field distribution at a constant distance must be considered when determining the radiation pattern. Also, it is convenient to normalize the expression for field distribution such that its maximum becomes unity. Then, the radiation pattern can be expressed as

$$F(\theta,\phi)=\frac{E}{E(\max)} \tag{3.46}$$

where $F(\theta, \phi)$ is the normalized field pattern, and $E(\max)$ is the maximum value of the magnitude of E over a sphere of observation radius r. In general, $F(\theta, \phi)$ can be complex-valued.

The radiation pattern can be also described by the radiated power. The power pattern gives the angular distribution of the power density and can be found from the r-component of the Poynting vector at the considered direction. Since the Poynting vector at far-field region is $(1/2)EH^{*}=|E|^{2}/2\eta$, the normalized power pattern becomes

$$P(\theta,\phi)=|F(\theta,\phi)|^{2} \tag{3.47}$$

The typical radiation pattern of an antenna is illustrated in Fig. 3.4(a), which has a single narrow main beam and minor side lobes. This pattern indicates that the antenna is a directional antenna. Figure 3.4(b) shows the analytically calculated radiation pattern of the ideal dipole radiator. The ideal dipole has a “doughnut” shaped radiation pattern so that the pattern in phi plane is isotropic; the pattern in theta plane is shown in Fig. 3.4(b).

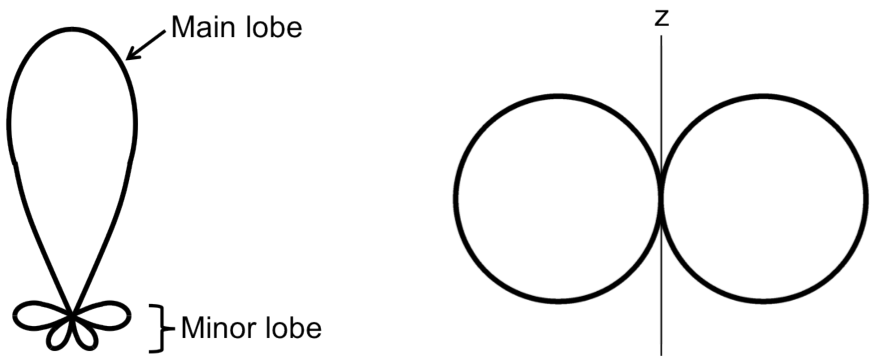

a. Example of Radiation Pattern

b. Radiation Pattern of Ideal Dipole

Figure 3.9 Examples of radiation pattern polar plots. a, Example of a radiation pattern which has directional main beam. **b,** Radiation pattern polar plot of *z*-aligned ideal dipole radiator in theta plane.

3.2.2 Directivity

The previous section discussed the radiation pattern of the antenna. Once the angular distribution of the radiated power is known, it is possible to calculate how much power density is radiated in a certain direction. This characteristic of an antenna is called its directivity. In order to define the directivity in an analytical expression, it is convenient to introduce the concept of radiation intensity. Radiation intensity is defined from

$$U(\theta,\phi) = \frac{1}{2} Re\left(\vec{E} \times \vec{H}\right) \cdot r^2 \hat{r} = S(\theta,\phi) r^2 \qquad (3.48)$$

Therefore, radiation intensity is the power radiated in a given direction per unit solid angle. Since Poynting vector S of the antenna at the far-field region is inversely proportion to the square of distance ($1/r^2$), radiation intensity is independent of distance r. Using the normalized field pattern, radiation intensity can be also expressed as

$$U(\theta,\phi) = U_m |F(\theta,\phi)|^2 \qquad (3.49)$$

where U_m is the maximum radiation intensity, and $F(\theta,\ \phi)$ is the normalized field pattern derived from Eq. (3.1). Radiation intensity was defined in Eq. (3.3), therefore, the total radiated power can be calculated by integrating the radiation intensity over entire solid angle around the antenna:

$$P = \iint U(\theta,\phi) d\Omega = U_m \iint |F(\theta,\phi)|^2 d\Omega \qquad (3.50)$$

Then, directivity is defined as the ratio of the radiation intensity in a certain direction to the average radiation intensity per unit solid angle:

$$D(\theta,\phi) = \frac{U(\theta,\phi)}{U_{ave}} \tag{3.51}$$

where U_{ave} is the average radiation intensity, which can be calculated as $U_{ave}=P/4\pi$. Although directivity $D(\theta,\ \phi)$ is a function of the angular coordinate that specifies a certain direction, directivity D is often used without any directional information. In this case, D refers to maximum directivity. By introducing a beam solid angle defined by $\Omega_A = \iint |F(\theta,\phi)|^2 d\Omega$, the maximum directivity can be expressed as:

$$D = \frac{4\pi}{\Omega_A} \tag{3.52}$$

Directivity is determined by radiation pattern in the transmitting mode of the antenna. However, directivity is also closely related to the receiving capability related to the reciprocal property of antenna. In many cases, optical antennas are used in the receiving mode to capture and focus light; therefore, it is important to design optical antenna with good directivity, which results in an efficient reception of light. The relationship between directivity and the receiving capability of antenna will be addressed in the section that discussed the effective aperture of antenna.

3.2.3 Input Impedance, Radiation Resistance and Radiation Efficiency

The input impedance of an antenna is the equivalent impedance seen at its terminal. Therefore, proper input terminals of an antenna must be defined before discussing its input impedance. As usual, the input impedance of an antenna consists of real and imaginary parts.

$$Z_A = R_A + jX_A \tag{3.53}$$

The real part R_A (input resistance) contributes to the power dissipation of the antenna, and the imaginary part X_A (input reactance) represents the power stored in the near field of the antenna. The input resistance can be calculated from the dissipated power of an antenna by:

$$R_A = \frac{2P}{|I_A|^2} \tag{3.54}$$

where P is the average power dissipated in an antenna, and I_A is the current at the input terminals. In general, the dissipated power by an antenna consists of radiative and ohmic losses. Then, the radiation resistance R_{rad} and the ohmic resistance R_{ohmic} of an antenna can be expressed as:

$$R_{rad} = \frac{2P_{rad}}{|I_A|^2} \tag{3.55}$$

$$R_{ohmic} = \frac{2P_{ohmic}}{|I_A|^2} = \frac{2(P - P_{rad})}{|I_A|^2} \tag{3.56}$$

where P_{rad} is the average radiation power, and P_{ohmic} is the dissipated power due to ohmic losses. Note that these resistances are defined using common currents I_A, which implies series resistances in the circuit model.

Equation (3.10) defined radiation resistance using the input terminal current; however, radiation resistance can be defined relative to the current at any point on the antenna. In some cases, radiation resistance relative to the maximum current on the antenna is also frequently used.

In terms of maximizing efficiency, radiated power is of interest whereas ohmic losses need to be minimized. Radiation efficiency is defined by the ratio of the radiated power to the total dissipated power by the antenna, which can be expressed as:

$$e_r = \frac{P_{rad}}{P} = \frac{P_{rad}}{P_{rad} + P_{ohmic}} = \frac{R_{rad}}{R_{rad} + R_{ohmic}} \tag{3.57}$$

At radio frequencies, ohmic losses can be ignored for many antennas since metals have the material property of being good conductors at low frequencies and radiation resistance is much greater than ohmic resistance. However, ohmic losses are not negligible at optical frequencies and radiation efficiencies must be considered.

This section has shown that the input impedance or the radiation resistance of an antenna is usually determined at its input terminals, which do not exist for optical antennas since optical antennas, in general, consist of isolated metal nanoparticles. However, as described above, radiation resistance can be defined relative to the current at any point of the antenna, and the connection between the resistance and the dissipated power is still valid and useful for study of optical antennas.

3.2.4 Antenna Effective Aperture

When an antenna is operating in receiving mode, the concept of effective aperture is convenient to consider the power captured by the antenna. The definition of the effective aperture (effective area) is expressed as:

$$A_e = \frac{P_A}{I_0} \tag{3.58}$$

where P_A is the power absorbed by the antenna, and I_0 is the power density of the incident wave. Effective aperture typically depends on the load resistance, and the maximum power transfer occurs when the conjugate matching condition is achieved. Here, we will derive the relationship between directivity and maximum effective aperture. For the derivation, consider a system of transmitting and receiving antennas shown in Fig. 3.5.

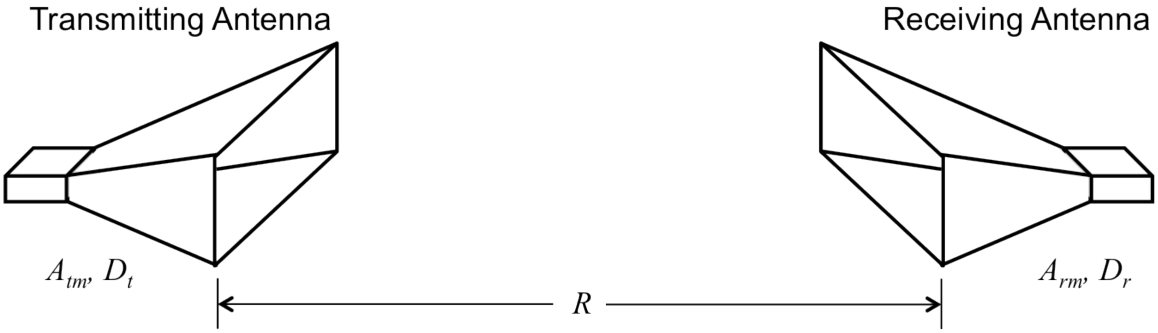

Figure 3.10 Transmitting and receiving antennas. System of transmitting and receiving antennas separated by a distance R.

In this system, maximum effective apertures and directivities of each antenna are represented by A_{tm}, A_{rm}, and D_t, D_r, respectively. The power density from the transmitting antenna is defined at the receiving antenna as:

$$I_0 = \frac{P_t D_t}{4\pi R^2} \qquad (3.59)$$

where P_t is the total radiated power by transmitting antenna. Assuming the case of maximum power transfer, the power collected by receiving antenna becomes

$$P_r = I_0 A_r = \frac{P_t D_t A_{rm}}{4\pi R^2} \qquad (3.60)$$

We can also express this equation as :

$$D_t A_{rm} = \frac{P_r}{P_t} 4\pi R^2 \qquad (3.61)$$

If the receiving antenna is used as a transmitter and the transmitting antenna is used as a receiver, then by virtue of reciprocity we can write

$$D_r A_{tm} = \frac{P_r}{P_t} 4\pi R^2 = D_t A_{rm} \qquad (3.62)$$

Therefore, we can define the relationship for the ratio of directivity to maximum effective aperture as:

$$\frac{D_t}{A_{tm}} = \frac{D_r}{A_{rm}} \qquad (3.63)$$

Here, we chose arbitrary antennas for the transmitter and receiver; therefore, the equation must be satisfactory for any antennas. This means that the ratio of directivity to maximum effective antenna has a constant value regardless of the type of an antenna. We can calculate this value from short dipole antenna, of which the directivity (3/2) and the maximum effective aperture ($3\lambda^2/8\pi$) are already known.

$$\frac{D}{A_{em}} = \frac{3/2}{3\lambda^2/8\pi} = \frac{4\pi}{\lambda^2} \qquad (3.64)$$

Therefore, the maximum effective aperture of any antenna becomes

$$A_{em} = \frac{\lambda^2}{4\pi} D \tag{3.65}$$

Note that the maximum effective aperture is dependent only on the directivity. This means that the maximum effective aperture is determined solely by the spatial mode matching between incident plane wave and radiation pattern of the antenna regardless of the load. Unmatched load decreases the transferred power, which is reflected on the reduced effective aperture.

3.3 Equivalent Circuit Model for Antenna

3.3.1 Circuit Model for Transmitting Antenna

For transmitting mode, assume that the antenna is attached to a generator with internal impedance Z_g, which consists of resistance R_g and reactance X_g. Then, the equivalent circuit of this system can be represented as shown in Fig. 3.6.

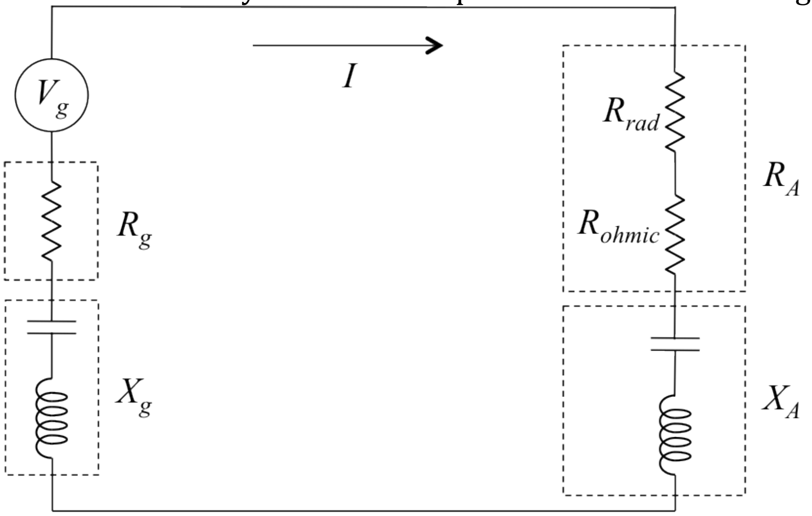

Figure 3.11 Equivalent circuit for transmitting antenna. Antenna in transmitting mode driven by a generator.

In order to find the power radiated by the antenna, the power dissipated in the radiation resistance must be calculated. As a first step, we find the circuit current given by

$$I = \frac{V_g}{Z_g + Z_A} = \frac{V_g}{R_g + R_{rad} + R_{ohmic} + j(X_g + X_A)} \tag{3.66}$$

and its magnitude by

$$|I| = \frac{|V_g|}{\left[(R_g + R_{rad} + R_{ohmic})^2 + (X_g + X_A)^2\right]^{1/2}} \tag{3.67}$$

where V_g is the voltage of the generator. Then, the power dissipated by radiation is given by

$$P_{rad} = \frac{|V_g|^2 R_{rad}}{2\left[(R_g + R_{rad} + R_{ohmic})^2 + (X_g + X_A)^2\right]} \tag{3.68}$$

and the power dissipated by ohmic loss due to antenna and generator internal resistance is given by

$$P_{ohmic} = \frac{|V_g|^2 R_{ohmic}}{2\left[(R_g + R_{rad} + R_{ohmic})^2 + (X_g + X_A)^2\right]} \tag{3.69}$$

$$P_g = \frac{|V_g|^2 R_g}{2\left[(R_g + R_{rad} + R_{ohmic})^2 + (X_g + X_A)^2\right]} \tag{3.70}$$

It can be easily shown that the maximum power transfer to antenna occurs when the conjugate matching is achieved, which is

$$R_g = R_{rad} + R_{ohmic} \tag{3.71}$$

$$X_g = -X_A \tag{3.72}$$

3.3.2 Circuit Model for Receiving Antenna

The previous section discussed the equivalent circuit of transmitting antennas. However, the case of the receiving antenna is more complicated due to the absence of an explicit voltage source. Instead, the receiving antenna circuit is actually driven by induced current due to the incident wave. For the discussion of equivalent circuit of receiving antenna, consider once more the transmitting and receiving antennas illustrated in Fig. 3.5. For convenience, denote the transmitting and receiving antennas as antenna 1 and 2, respectively. Then, the system can be represented as consisting of two ports, as indicated Fig. 3.7; this satisfies

$$V_1 = Z_{11}I_1 + Z_{12}I_2 \tag{3.73}$$

$$V_2 = Z_{21}I_1 + Z_{22}I_2 \tag{3.74}$$

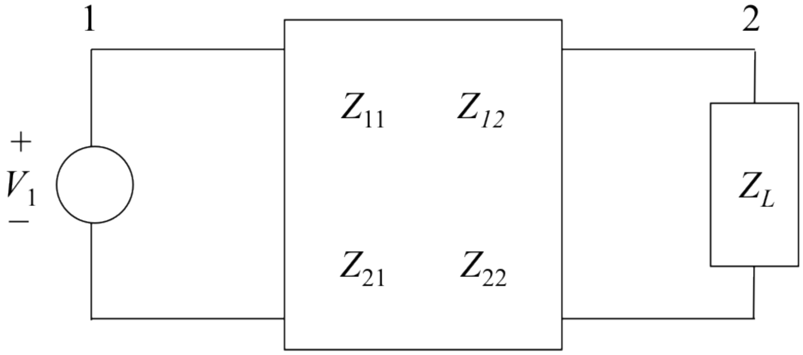

Figure 3.12 Equivalent representation for transmitting and receiving antennas.

Consider the case of a large distance between the transmitting and receiving antennas where Z_{12} in Eq. (3.28) is very small and negligible. Then, Eq. (3.28) can be expressed as:

$$V_1 \approx Z_{11} I_1 \tag{3.75}$$

where Z_{11} is the input impedance of the transmitting antenna. However, the term $Z_{21}I_1$ in Eq. (3.29) cannot be ignored. Instead, Eq. (2.29) is now represented by Thévenin's equivalent circuit, as shown in Fig. 3.8. Thus, $Z_{21}I_1$ is the induced voltage source in the receiving antenna circuit.

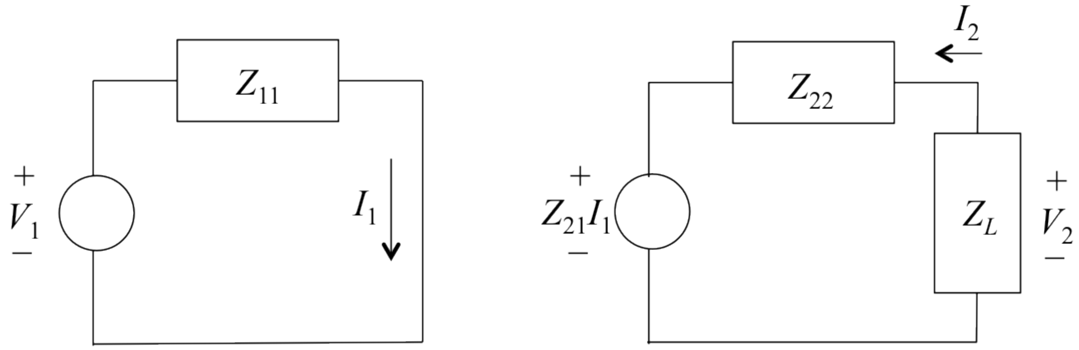

Figure 3.13 Approximate equivalent circuit for transmitting and receiving antennas.

The receiving antenna is typically connected to a load with internal impedance Z_L, which consists of resistance R_L and reactance X_L. The detailed equivalent circuit for the receiving antenna is shown in Fig. 3.9.

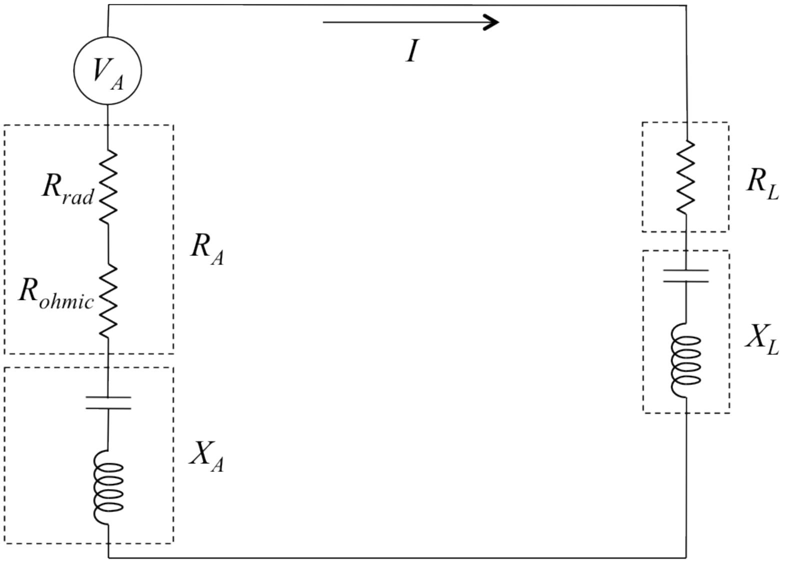

Figure 3.14 Equivalent circuit for receiving antenna. Antenna in receiving mode connected to a load.

From the equivalent circuit, we first find the current, which is given by

$$I = \frac{V_A}{Z_A + Z_L} = \frac{V_A}{R_{rad} + R_{ohmic} + R_L + j(X_A + X_L)} \tag{3.76}$$

where V_A (=$Z_{21}I_1$) is the voltage induced by the antenna. Then, the power delivered to the load can be calculated to be

$$P_L = \frac{|V_A|^2 R_L}{2[(R_L + R_{rad} + R_{ohmic})^2 + (X_L + X_A)^2]} \tag{3.77}$$

and the power dissipated in the antenna is given by

$$P_{ohmic} = \frac{|V_A|^2 R_{ohmic}}{2[(R_L + R_{rad} + R_{ohmic})^2 + (X_L + X_A)^2]} \tag{3.78}$$

$$P_{rad} = \frac{|V_A|^2 R_{rad}}{2[(R_L + R_{rad} + R_{ohmic})^2 + (X_L + X_A)^2]} \tag{3.79}$$

Note that P_{rad} is the scattered (or re-radiated) power by antenna. This scattered power does not exist as a separate measurable independent quantity of real power that enters into any statement of power conservation. However, the scattered wave determines the amount of captured power by the antenna through interference with the incident wave.

Again, the maximum power transfer to the attached load occurs when the conjugate matching condition is achieved, which is

$$R_L = R_{rad} + R_{ohmic} \tag{3.80}$$

$$X_L = -X_A \tag{3.81}$$

Now, let us assume that the receiving antenna is attached to a conjugate matched load and the antenna has negligible ohmic losses. Then, the power delivered to the load is

$$P_L = \frac{|V_A|^2}{8R_{rad}} \tag{3.82}$$

The absorbed power under this condition can be also expressed from the definition of maximum effective aperture; therefore

$$P_L = A_{em} I_o \tag{3.83}$$

where A_{em} is the maximum effective aperture, and I_o is the power density of incident wave. A comparison of Eqs. (2.37) and (2.38) demonstrates that

$$V_A = 2\sqrt{2R_{rad} A_{em} I_o} \tag{3.84}$$

Therefore, the induced voltage in the equivalent circuit is proportional to the square root of the radiation resistance and the maximum effective aperture. The equivalent circuit is useful in computing the power transfer and the condition for its optimum case. In many cases, the optical antenna is operating in the receiving mode, and the equivalent circuit of the receiving antenna can be used to derive the local field enhancement of the antenna. The derivation of the local field enhancement of the optical antenna will be discussed in the following chapter.

CHAPTER 4

Optical Antennas and Field Enhancement

Optical antennas are nanoscale structures consisting of metallic particles that interact with electromagnetic waves at optical frequencies. Optical antennas, similar to RF antennas, can operate as both receiving and transmitting modes. In receiving mode, optical antennas capture free-space electromagnetic wave and focus light energy into their high field region beyond their diffraction limit. In transmitting mode, optical antennas accelerate the spontaneous emission of a quantum emitter and radiate electromagnetic wave in preferred direction when the emitter is placed in the vicinity of high field region of optical antennas.

This chapter will discuss the optical antenna's distinctive receiving and transmitting properties. Then, the local field enhancement of optical antenna will be derived as a critical design parameter for the performance of optical antenna, followed by the discussion of how to optimize the field enhancement. Finally, possible applications of optical antennas and challenges for current optical antenna technology will be reviewed.

4.1 Coupling and Focusing Light by Optical Antenna

4.1.1 Coupled-Mode Theory for Antenna and Effective Cross Sections

In receiving mode, an optical antenna captures electromagnetic waves propagating in free space and stores the electromagnetic energy in its near fields oscillating between the electric and magnetic fields. The capacitive or inductive reactance of optical antenna corresponds to the energy stored in the electric or magnetic field, and the resistance contributes to the power dissipation by radiation and absorption (ohmic loss) of metal. Therefore, an optical antenna acts as a RLC resonator with the resonance frequency $\omega_0 = 1/\sqrt{LC}$, as shown in Fig. 4.1(a). This section applies coupled-mode theory to investigate the coupling of light by optical antennas. The coupled mode theory is a useful technique to analyze the coupling between resonators and propagating waves [45].

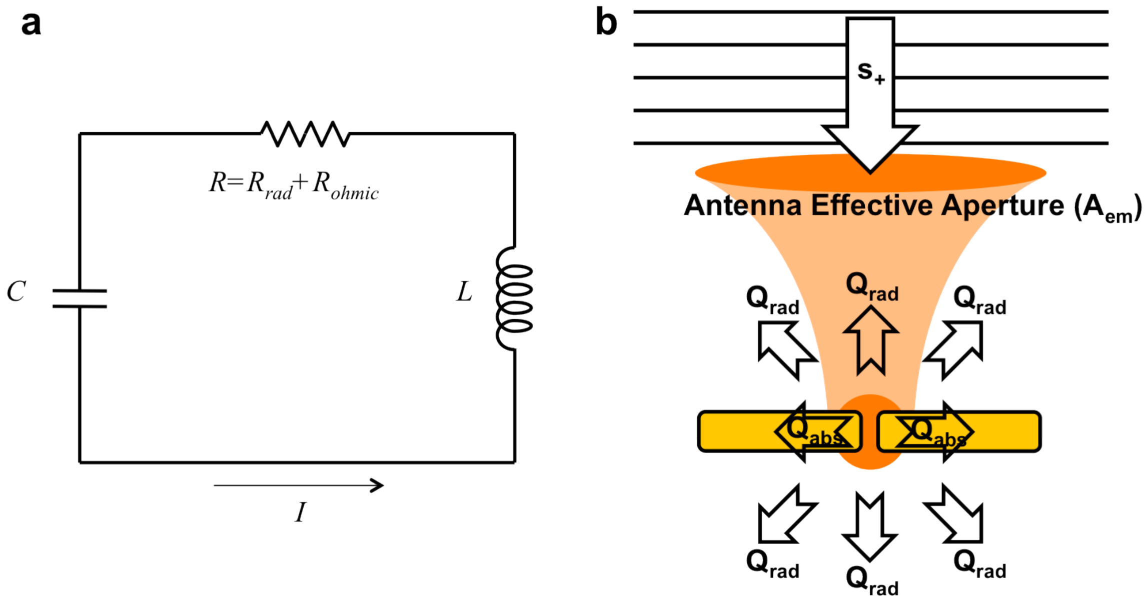

Figure 4.15 Equivalent circuit and schematic of optical antenna for coupled-mode theory. a, Simplified circuit model for optical antenna. **b,** Schematic and modeling of optical antenna using coupled-mode theory.

Figure 4.1(b) illustrates the schematic and modeling of an optical antenna using coupled-mode theory. The mode amplitude of an optical antenna with the maximum effective aperture A_{em}, illuminated by an excitation beam of spot size A_i, is given by coupled-mode theory as

$$\frac{da}{dt} = j\omega_0 a - \frac{1}{2}\left(\frac{1}{\tau_{rad}} + \frac{1}{\tau_{abs}}\right) a + \sqrt{\frac{A_{em}/A_i}{\tau_{rad}}}\, s_+ \qquad (4.85)$$

where a and s_+ are the mode amplitude in the cavity and the wave amplitude traveling toward the resonator, respectively, ω_0 is the resonance frequency of the cavity, and $1/\tau_{rad}$ and $1/\tau_{abs}$ express the rate of decay due to radiation and absorption, respectively. With the excitation source of frequency ω, we have:

$$a = \frac{\sqrt{\frac{A_{em}/A_i}{\tau_{rad}}}\, s_+}{j(\omega - \omega_0) + \frac{1}{2}\left(\frac{1}{\tau_{rad}} + \frac{1}{\tau_{abs}}\right)} \qquad (4.86)$$

Then, the energy stored in the cavity on resonance can be calculated:

$$|a|^2 = \frac{4\frac{A_{em}/A_i}{\tau_{rad}} |s_+|^2}{\left(\frac{1}{\tau_{rad}} + \frac{1}{\tau_{abs}}\right)^2} \qquad (4.87)$$

From the stored mode energy, the power dissipated by scattering and absorption is determined thus:

$$P_{sca} = \frac{|a|^2}{\tau_{rad}} = \frac{4\frac{A_{em}/A_i}{\tau_{rad}^2}|s_+|^2}{\left(\frac{1}{\tau_{rad}} + \frac{1}{\tau_{abs}}\right)^2} \tag{4.88}$$

$$P_{abs} = \frac{|a|^2}{\tau_{abs}} = \frac{4\frac{A_{em}/A_i}{\tau_{rad}\tau_{abs}}|s_+|^2}{\left(\frac{1}{\tau_{rad}} + \frac{1}{\tau_{abs}}\right)^2} \tag{4.89}$$

Using the definition of effective cross sections $\sigma = P/I_0$ with the relations $I_0 = |s_+|^2/A_i$ and $1/\tau = \omega/Q$, the effective cross sections are given by

$$\sigma_{sca} = \frac{P_{sca}}{I_0} = 4A_{em}\frac{(1/\tau_{rad})^2}{(1/\tau_{rad} + 1/\tau_{abs})^2} = 4A_{em}\frac{Q^2}{Q_{rad}^2} \tag{4.90}$$

$$\sigma_{abs} = \frac{P_{abs}}{I_0} = 4A_{em}\frac{(1/\tau_{rad})(1/\tau_{abs})}{(1/\tau_{rad} + 1/\tau_{abs})^2} = 4A_{em}\frac{Q^2}{Q_{rad}Q_{abs}} \tag{4.91}$$

$$\sigma_{ext} = \sigma_{sca} + \sigma_{abs} = 4A_{em}\frac{1/\tau_{rad}}{1/\tau_{rad} + 1/\tau_{abs}} = 4A_{em}\frac{Q}{Q_{rad}} \tag{4.92}$$

where Q is the total quality factor that is given by $Q = (1/Q_{rad} + 1/Q_{abs})^{-1}$. The maximum power transfer to absorption occurs when there is no reflection to the resonator. This happens when Q_{rad} is equal to the Q_{abs}, which is the condition for critical coupling. Under the condition for critical coupling ($Q_{rad} = Q_{abs}$), it can be easily seen from Eq. (4.7) that the absorption cross section σ_{abs} is recovered by the maximum effective aperture A_{em}. The additional discussion about general free-space resonant scattering using coupled-mode theory can be found in Ref. [46].

Using coupled-mode theory, we derived that the mode energy stored in optical antenna and the effective cross sections of the antenna is a function of the maximum effective aperture and the relative loss rate between the radiation and the absorption. Therefore, it is important to design an optical antenna with a large effective aperture and critically matched quality factors in order to optimize the light coupling. As shown in Chapter 3, the maximum effective aperture is proportional to the directivity; therefore, it can be improved by directivity engineering, such as applying the array factor or using external guide to capture more light. For the critically coupled condition, the radiation engineering of an optical antenna is required since the absorption is typically limited by material's inherent loss [47]. The antenna designs to achieve radiation engineering will be discussed in later chapters.

4.1.2 Light Focusing beyond Diffraction Limit

The wave vector of surface plasmon propagating at the metal boundary was derived in Chapter 2. From Eq. (2.21), the normal component of wave vector in the dielectric medium is given by

$$k_{d,\perp} = k_0 \sqrt{\frac{\varepsilon_d^2}{\varepsilon_m + \varepsilon_d}} \qquad (4.93)$$

where k_0 is the wave vector at free-space, and ε_d and ε_m are the dielectric constants of the dielectric and metallic media, respectively. The electromagnetic field decays exponentially since the normal wave vector has imaginary value. It can be inferred from Eq. (4.9) that the fields decay even faster when $-\mathrm{Re}\{\varepsilon_m\}$ approaches to ε_d. This phenomenon overcomes the diffraction limit and results in the concentration of electromagnetic energy into the sub-wavelength region. Figure 4.2 illustrates the coupling and focusing light of an optical antenna. An optical antenna efficiently captures free-space propagating electromagnetic wave on resonance, as shown in Fig. 4.2(a), and concentrates the electromagnetic fields at the metal surface [Fig. 4.2(b)].

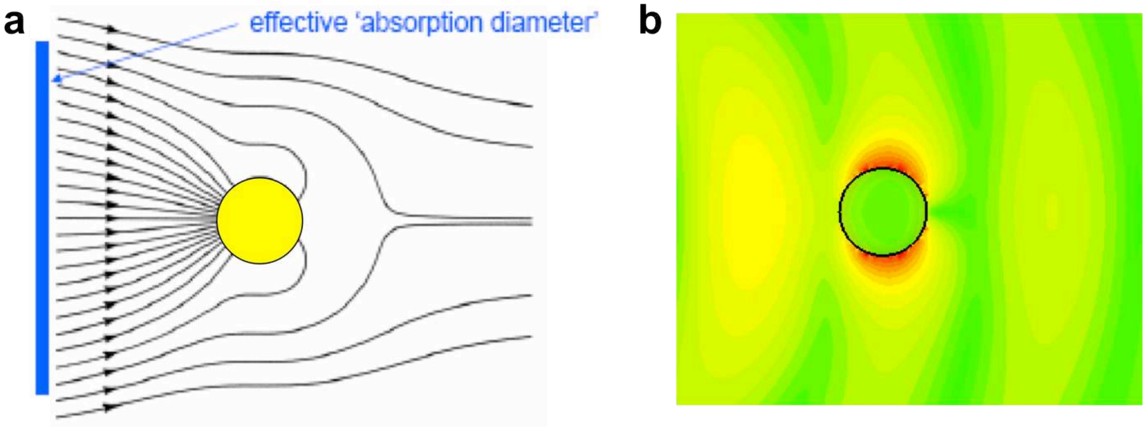

Figure 4.16 Light focusing of optical antenna on resonance. a, Power streamline on resonance. **b,** Electric field distribution.

As a result, the local field at high field region of the optical antenna is significantly enhanced. The enhancement of the local field depends on how efficiently the optical antenna captures the electromagnetic wave and how tightly it confines the energy in the modal volume. There properties are determined by material and geometry of optical antenna. As discussed in previous sections, the coupling of the incident wave is determined by the radiation pattern and the quality factors of optical antenna. The near-field confinement depends on the excited resonant mode and the modal volume of the optical antenna. Since the strong local field can be used for various areas such as sensitive bio-chemical sensing and sensitive photo-detection, it is important to design efficient optical antenna with high field enhancement. The derivation of local field enhancement will be shown in detail later in this section.

4.2 Enhanced Spontaneous Emission by Optical Antenna

4.2.1 Spontaneous Emission in Free Space

Spontaneous emission is the process whereby an atom or molecule in an excited state undergoes a transition to a lower state and emits a photon. The spontaneous emission can be explained by quantum electrodynamics (QED), in which not only atomic levels but also the electromagnetic field is quantized in space. The quantization of the electromagnetic field is called second quantization. In quantum electrodynamics, the electromagnetic field in space is described in terms of an infinite set of harmonic oscillators and each level of this harmonic oscillator corresponds to a state of number (n) of photons of energy $\hbar\omega$. In the ground state (n=0), each oscillator still has zero-point energy of $\hbar\omega/2$ and the vacuum field E_{vac} is regarded to contribute to the zero-point energy. Spontaneous emission can be understood as the downward transition of an atom (or molecule) induced by the vacuum field.

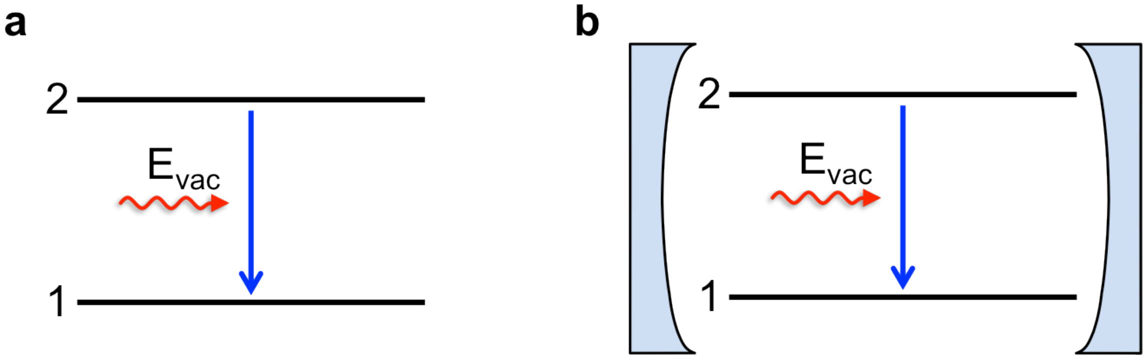

Figure 4.17 Two level system in free space and a cavity. a, In free space. **b,** In a cavity.

Consider an atom of a simple two-level system as shown in Fig. 4.3(a). Then, using Fermi's golden rule, the probability of spontaneous emission can be expressed as

$$\Gamma_0 = \frac{2\pi}{\hbar} |D_{21} E_{vac}|^2 \rho \qquad (4.94)$$

where D_{21} is the matrix element of the electric dipole of the atom between two levels, E_{vac} is the vacuum electric field, and ρ is the mode density per unit energy.

Using the vacuum energy relation $\varepsilon_0|E_{vac}|^2V=\hbar\omega/2$ and the mode density expression $\rho=\omega^2V/\pi^2\hbar c^3$, the spontaneous emission probability can be calculated as

$$\Gamma_0=\frac{\omega^3}{3\pi\hbar c^3}\frac{|D_{21}|^2}{\varepsilon_0} \tag{4.95}$$

Here, the factor of 3 in denominator comes from the average of the arbitrary polarizations.

4.2.2 Spontaneous Emission in a Cavity: Purcell Effect

The mode profile of the vacuum field is significantly altered in a cavity whose size is comparable to the wavelength, and it also causes the dramatic change of spontaneous emission rate. The research on the atom-field interaction in a cavity resulted in the development of a new field in atomic physics and quantum optics called cavity quantum electrodynamics.

One of the principle ideas underlying cavity quantum electrodynamics appeared in 1946 [48]. E. Purcell suggested that the rate of spontaneous emission in a system that is coupled to a resonant electrical circuit can be increased by a factor

$$F=\frac{3\lambda^3}{4\pi^2}\left(\frac{Q}{V}\right) \tag{4.96}$$

where λ is the wavelength of the transition, Q is the quality factor of the resonator, and V is the volume of the resonator. Therefore, the emission rate is enhanced by the ratio $Q\lambda^3/V$, which can be very large with small mode volume. This enhanced spontaneous emission has been experimentally observed in the millimeter wave regime for Rydberg atoms of sodium coupled to a Febry-Perot cavity [49]. Here, we prove this factor by comparing the spontaneous emission rate in free space and in a resonator.

In the previous section, we calculated the probability of spontaneous emission in free space, which is given by

$$\Gamma_0=\frac{\omega^3}{3\pi\hbar c^3}\frac{|D_{21}|^2}{\varepsilon_0} \tag{4.97}$$

Now, let us consider the spontaneous emission of an atom in a cavity [Fig. 4.3(b)]. The mode structure of the vacuum field is changed in the cavity. Therefore, we need to use the different vacuum field, which is given from $\varepsilon_0|E_{vac}|^2V_{eff}=\hbar\omega/2$ where V_{eff} is the effective mode volume of the cavity. And also, the mode density seen by the atom in the cavity becomes $1/\hbar\Delta\omega$, where $\Delta\omega$ is the bandwidth of the cavity. Then, using Fermi's golden rule, the spontaneous emission probability is given from by:

$$\Gamma=\frac{\pi}{\hbar}\frac{|D_{21}|^2}{\varepsilon_0}\frac{\omega/\Delta\omega}{V_{eff}}=\frac{\pi}{\hbar}\frac{|D_{21}|^2}{\varepsilon_0}\frac{Q}{V_{eff}} \tag{4.98}$$

Finally, the enhancement of spontaneous emission rate is expressed as

$$F = \frac{\Gamma}{\Gamma_0} = \frac{3\lambda^3}{8\pi}\frac{Q}{V_{eff}} \tag{4.99}$$

This result shows the factor of $\pi/2$ difference compared to Eq. (4.12), which is probably due to the normalization of the vacuum field. However, the essential trend of the spontaneous emission rate enhancement is identical. The enhancement factor is proportional to the quality factor of the cavity and inversely proportional to the cavity mode volume. Therefore, the spontaneous emission rate can be significantly increased if the size of the cavity scales down more and more.

It is possible to create high-quality optical cavities using micro-disks [50] and photonic crystals [51][52]. Unfortunately, because of the diffraction limit of light, these approaches are not an efficient means of enhancing the spontaneous emission and result in a large mode volume of the cavity. Since optical antennas are capable of confining the light in a narrow region much smaller than the wavelength scale, they offer great opportunities to enhance significantly the spontaneous emission rate.

4.3 Field Enhancement of Optical Antenna

In the previous sections, we have demonstrated that optical antennas have great advantages in receiving and concentrating free-space electromagnetic wave, and in improving emission property of quantum emitter placed in the high field region. To design an efficient optical antenna, the local field enhancement at the high field region of the optical antenna needs to be optimized since the field enhancement is the direct indication of focused light energy from captured electromagnetic wave. The vacuum field is also enhanced similar to the mode profile of the local field, resulting in the enhanced spontaneous decay rate of an emitter. In this section, we will derive the field enhancement of the optical antenna using the coupled-mode theory and the antenna circuit model, and we will also discuss strategies to maximize the field enhancement of optical antenna.

4.3.1 Field Enhancement Derivation from Coupled-Mode Theory

Section 4.1.1 demonstrated that the mode energy stored by optical antenna on resonance can be expressed using coupled-mode theory where

$$|a|^2 = \frac{4\frac{A_{em}/A_i}{\tau_{rad}}|s_+|^2}{\left(\frac{1}{\tau_{rad}} + \frac{1}{\tau_{abs}}\right)^2} \tag{4.100}$$

Substituting the incident power $|s_+|^2 = \frac{1}{2}\varepsilon_0|E_i|^2cA_i$ in Eq. (4.16), the mode energy can be written as

$$|a|^2 = \frac{4\frac{A_{em}/A_i}{\tau_{rad}}\cdot\frac{1}{2}\varepsilon_0|E_i|^2cA_i}{\left(\frac{1}{\tau_{rad}}+\frac{1}{\tau_{abs}}\right)^2} = \frac{2A_{em}\left(\frac{1}{\tau_{rad}}\right)\varepsilon_0|E_i|^2c}{\left(\frac{1}{\tau_{rad}}+\frac{1}{\tau_{abs}}\right)^2} \qquad (4.101)$$

Using the effective mode volume V_{eff}, the mode energy can be rewritten as

$$|a|^2 = \frac{1}{2}\varepsilon_0|E_{loc}|^2V_{eff} \qquad (4.102)$$

where E_{loc} is the local field at the high field region of optical antenna. Equating Eqs. (4.17) and (4.18), local field enhancement on resonance can be given by

$$\frac{|E_{loc}|^2}{|E_i|^2} = \frac{4A_{em}\left(\frac{1}{\tau_{rad}}\right)c}{\left(\frac{1}{\tau_{rad}}+\frac{1}{\tau_{abs}}\right)^2V_{eff}} = \frac{2A_{em}\lambda_{res}Q^2}{\pi Q_{rad}V_{eff}} \qquad (4.103)$$

where λ_{res} is the resonance wavelength and the relation $1/\tau=\omega/Q$.

Using $A_{em} = \frac{\lambda^2}{4\pi}D$, the field enhancement can be rewritten in a more comprehensive form as

$$\frac{|E_{loc}|^2}{|E_i|^2} = \frac{2}{3}D\left(\frac{Q}{Q_{rad}}\right)\left(\frac{3\lambda^3Q}{4\pi^2V_{eff}}\right) \qquad (4.104)$$

Therefore, the local field enhancement of optical antenna is proportional to the directivity D, the radiation efficiency Q/Q_{rad}, and the Purcell factor, $3\lambda^3Q/4\pi^2V_{eff}$.

4.3.2 Field Enhancement Derivation from Circuit Model

The local field enhancement of optical antenna can be also derived from the antenna circuit model, as shown in Fig. 4.4, where the voltage source in the circuit model of receiving antenna is given by $|V_A| = 2\sqrt{2R_{rad}A_{em}I_0}$ in Section 3.3.2.

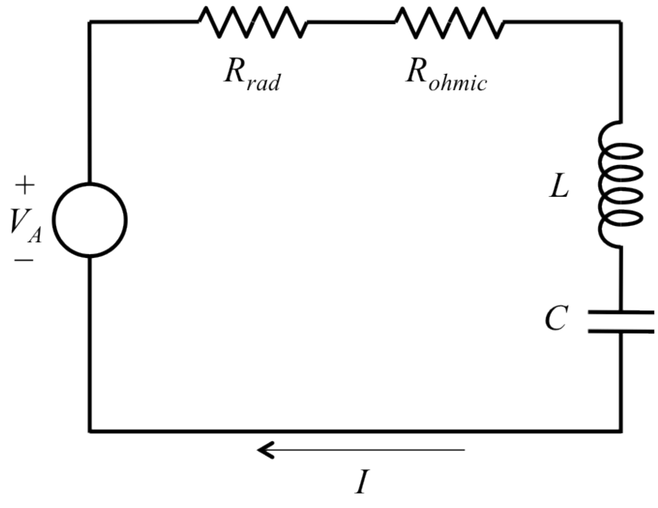

Figure 4.18 Circuit model for optical antenna in receiving mode.

From the circuit model, the current in the loop is given by

$$I = \frac{V_A}{R_{rad} + R_{ohmic} + j(\omega L - \frac{1}{\omega C})} \tag{4.105}$$

On resonance ($\omega = 1/\sqrt{LC}$), the magnitude of current is rewritten as

$$|I| = \frac{|V_A|}{R_{rad} + R_{ohmic}} \tag{4.106}$$

Chapter 3 discussed using the power dissipated by resistive parts to calculate scattered and absorbed power. Next, we turn to the near field stored by the reactive parts of the circuit. The electric field energy is stored in the capacitance and the magnetic field energy in the inductance. Therefore, the time-averaged energy stored by antenna is calculated thus:

$$U = \frac{1}{4}(C|V|^2 + L|I|^2) = \frac{1}{2}C|V|^2 = \frac{|I|^2}{2\omega^2 C} \tag{4.107}$$

where V is the voltage applied only on capacitance, and $C|V|^2 = L|I|^2$ was obtained from the resonance condition. By definition of effective mode volume, the mode energy can be also expressed as

$$U = \frac{1}{2}\varepsilon_0 |E_{loc}|^2 V_{eff} \tag{4.108}$$

Equating Eqs. (4.23) and (4.24) and using $|V_A| = 2\sqrt{2R_{rad}A_{em}I_0}$ and $I_0 = \frac{1}{2}\varepsilon_0 |E_i|^2 c$, we obtain the following expression

$$\begin{aligned} U = \frac{|I|^2}{2\omega^2 C} &= \frac{|V_A|^2}{2\omega^2 C(R_{rad} + R_{ohmic})^2} \\ &= \frac{4R_{rad}A_{em}I_0}{\omega^2 C(R_{rad} + R_{ohmic})^2} = \frac{4R_{rad}A_{em} \cdot \frac{1}{2}\varepsilon_0 |E_i|^2 c}{\omega^2 C(R_{rad} + R_{ohmic})^2} \\ &= \frac{1}{2}\varepsilon_0 |E_{loc}|^2 V_{eff} \end{aligned} \tag{4.109}$$

Therefore, the field enhancement is given by

$$\frac{|E_{loc}|^2}{|E_i|^2} = \frac{4A_{em}R_{rad}c}{\omega^2 (R_{rad} + R_{ohmic})^2 C V_{eff}} \tag{4.110}$$

Using the relation Q=$1/\omega RC$, the field enhancement can be expressed as

$$\frac{|E_{loc}|^2}{|E_i|^2} = \frac{2A_{em}\lambda_{res}Q^2}{\pi Q_{rad} V_{eff}} \tag{4.111}$$

Note that this result is identical to Equation (4.19), which is derived from coupled-mode theory.

4.3.3 Conditions for Maximum Field Enhancement

Using the equation derived for the field enhancement, there are five parameters that can be optimized to achieve maximum field enhancement:

1. The antenna needs to be excited on resonance (λ_{res}) [53], which can be achieved by tuning the antenna dimensions [54] or loading the antenna gap with appropriate materials [55], [56].

2. The effective mode volume of the antenna (V_{eff}) needs to be reduced, which can be achieved by shrinking the size of antenna gap [57]–[59].

3. The maximum effective aperture (A_{em}) needs to be optimized through matching the antenna's radiation pattern with the excitation signal. For example, the radiation pattern can be engineered for good directivity since the effective aperture is proportional to the directivity of the antenna [60], [61].

4. Determine the optimum condition for an antenna's relevant loss rates (i.e. Q, Q_{rad}, Q_{abs}) by taking the derivative of Eq. (4.27) with respect to Q_{rad} and equate it to 0. Assuming that the maximum effective aperture (A_{em}), effective mode volume (V_{eff}), and the Q_{abs} vary slowly compared to Q_{rad}, the maximum field enhancement condition is achieved when Q_{rad} becomes equal to Q_{abs}:

$$Q_{rad} = Q_{abs} \tag{4.112}$$

This is the identical condition for critical coupling from coupled-mode theory. From the circuit model, it can be found that the current in the circuit is maximized when this condition is achieved. This is also analogous to the impedance matching concept in antenna theory [62]–[64].

5. At the optimum Q condition ($Q_{rad} = Q_{abs} = 2Q$), the expression for the field enhancement reduces to:

$$\frac{|E_{loc}|^2}{|E_i|^2} = \frac{A_{em}\lambda_{res}Q}{\pi V_{eff}} = \frac{A_{em}\lambda_{res}Q_{abs}}{2\pi V_{eff}} \tag{4.113}$$

Therefore, the optimized field enhancement for given material is directly proportional to absorption quality factor (Q_{abs}), which is supported by previously reported [65] research on high field enhancement with low loss materials (such as silver).

In following chapters, 5, 6 and 7, antenna designs that achieve these conditions and can be readily fabricated using s will be discussed.

4.4 Applications and Challenges of Optical Antennas

In this section, we discuss various possible applications using optical antennas. As a nanoscale receiver and/or transmitter, optical antennas have been widely used in sensitive photodetection, high-resolution imaging, heat-assisted magnetic recording, efficient light emission, and bio-chemical sensing. Here, we briefly review some of promising potential uses for optical antennas.

The optical antenna is a useful tool for photodetection due to its receiving capability (Fig. 4.5) [12]. Optical antenna efficiently captures light and focuses it into sub-wavelength region, which enables shrinking dramatically the size of photodetector. With the reduced size, the signal-to-noise ratio of the photodetector is improved, thus improving the performance, power consumption, and speed. The nanoscale size of the nano-photodetector makes possible the integration in photonic circuits.

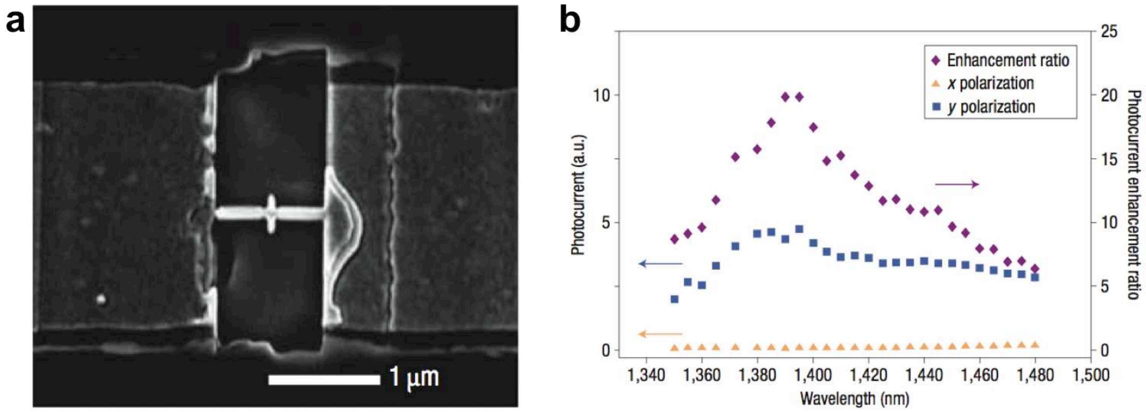

Figure 4.19 Photodetector using optical antenna. a, SEM image of Ge photodetector with optical antenna. **b,** Measured photocurrent responses for light polarization in the y and x directions [12].

High-resolution imaging is another potential area where optical antennas could be applied. The resolution of optical microscopy using a far-field lens-based technique is limited by constraints of the diffraction limit. The optical antenna breaks this barrier by focusing light into the sub-diffraction-limited area. It has been recently reported that a monopole antenna assembled in a scanning probe microscope can improve the spatial resolution up to ~30 nm (Fig. 4.6) [66].

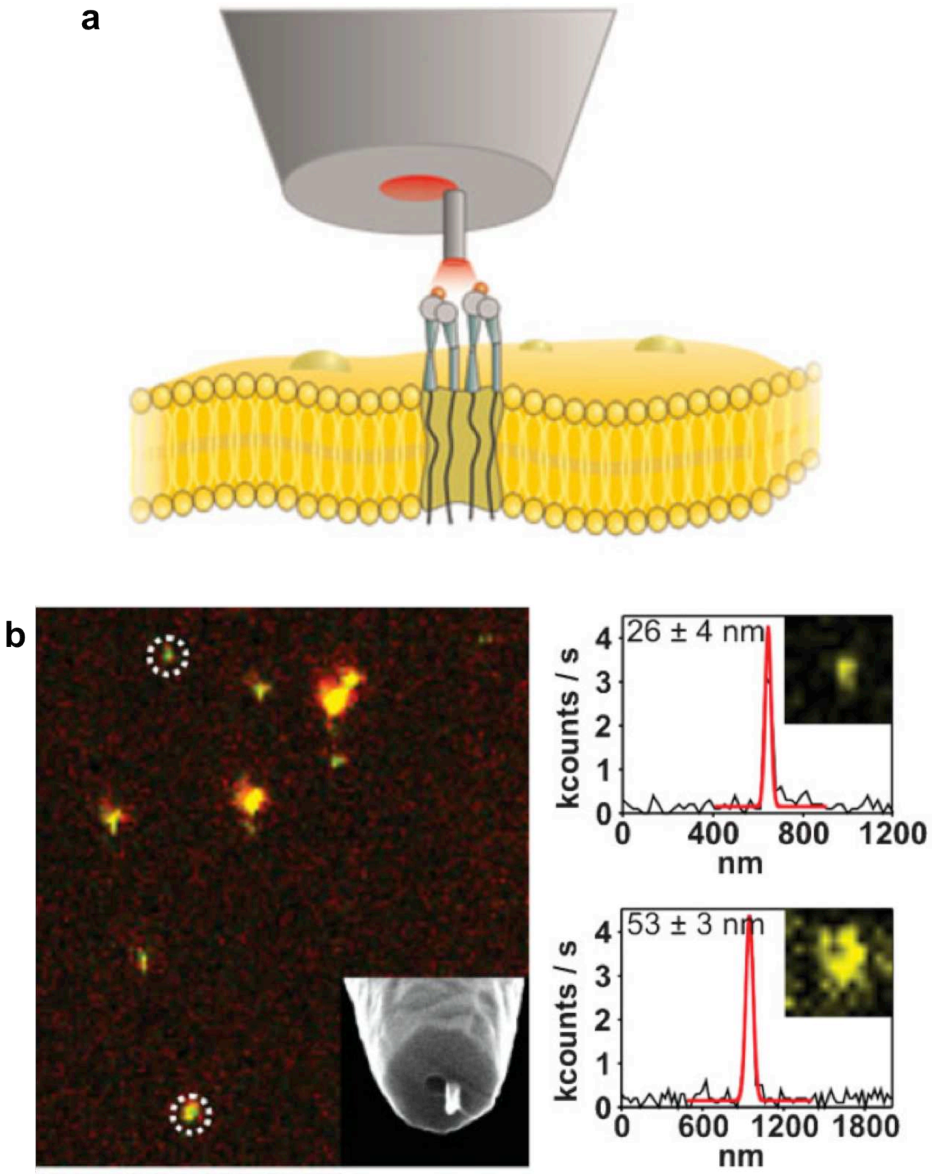

Figure 4.20 High resolution bio-imaging with optical antenna. a, Schematic illustration. **b,** Fluorescently labeled antibodies imaged by the antenna probe. Inset shows the SEM image of the monopole antenna probe. Two right plots show cross-sections of the two circled spots [66].

Improved spatial resolution by optical antennas can be also applied to magnetic recording. In order to increase the storage density of hard disk drives, recordings with extremely high spatial resolution is required. Using an optical antenna, optical energy can be delivered and confined to a small spot that is much smaller than the diffraction limit. This has been demonstrated in heat-assisted magnetic recording (HAMR) with a data areal density of ~375 Tb/m^2 (Fig. 4.7) [26].

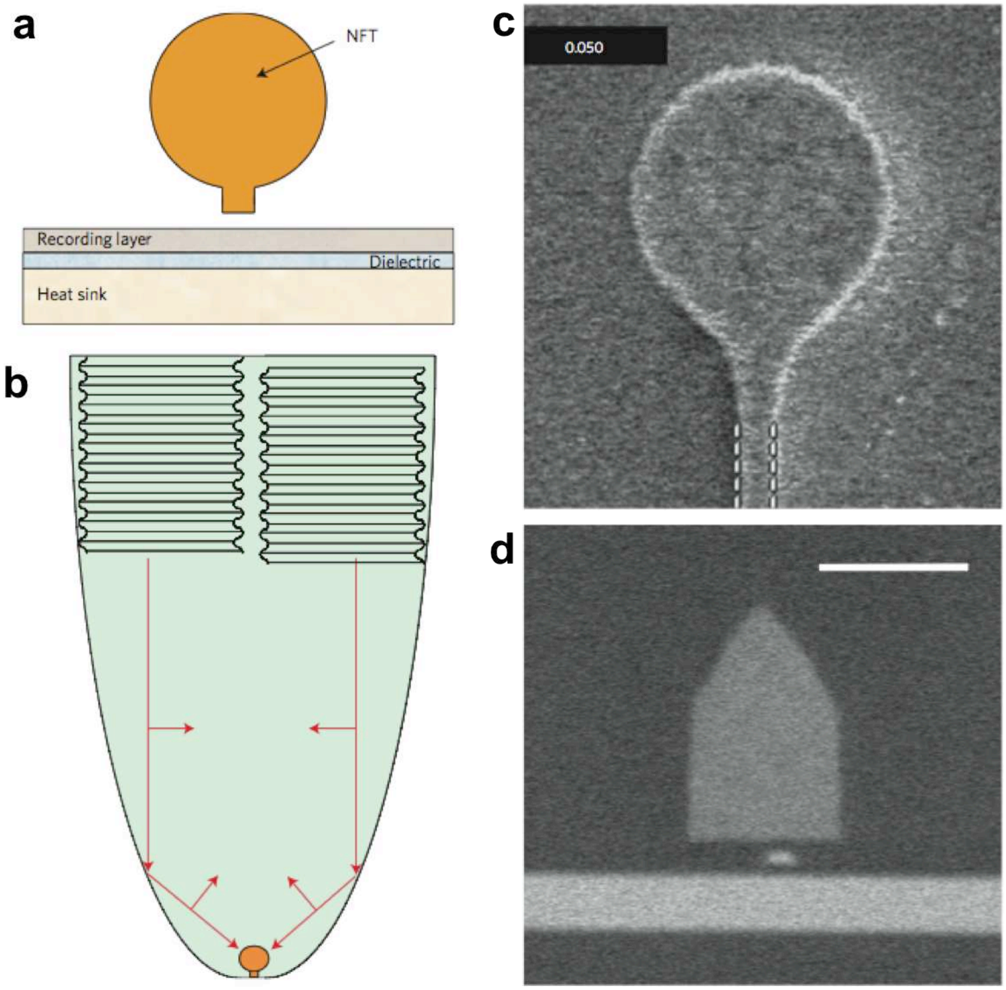

Figure 4.21 Heat-assisted magnetic recording with optical antenna. a, b, Schematic illustration. **c,** SEM image of fabricated device. The distance between dashed lines is 50 nm. **d,** SEM of the cross sectional view of fabricated device (small rectangle). Scale bar, 300 nm [26].

The transmitting feature of optical antennas holds promise in applications for efficient light emitting. As discussed in Section 4.2, the rate of spontaneous emission is significantly altered with optical antennas. With its extremely small mode volume, the rate of spontaneous emission of the optical antenna can exceed that of stimulated emission, which is limited by nonlinear gain saturation. Therefore, the modulation speed of nanoscale light emitting device (nanoLED) using an optical antenna can be faster than that of conventional lasers [67]. Since nanoLEDs do not require a certain bias above threshold, nanoLEDs are more energy-efficient than lasers.

Some applications gain benefits from both the receiving and transmitting capability of optical antennas. One example is fluorescence detection. The focused light in the high field region of an optical antenna can excite with improved efficiency a fluorescent molecule. The optical antenna also enhances the emission rate of the molecule. As reported by Kinkhabwala et al., the detection of single molecule fluorescence experiences 1340-fold enhancement using gold bowtie antenna (Fig. 4.8) [68].

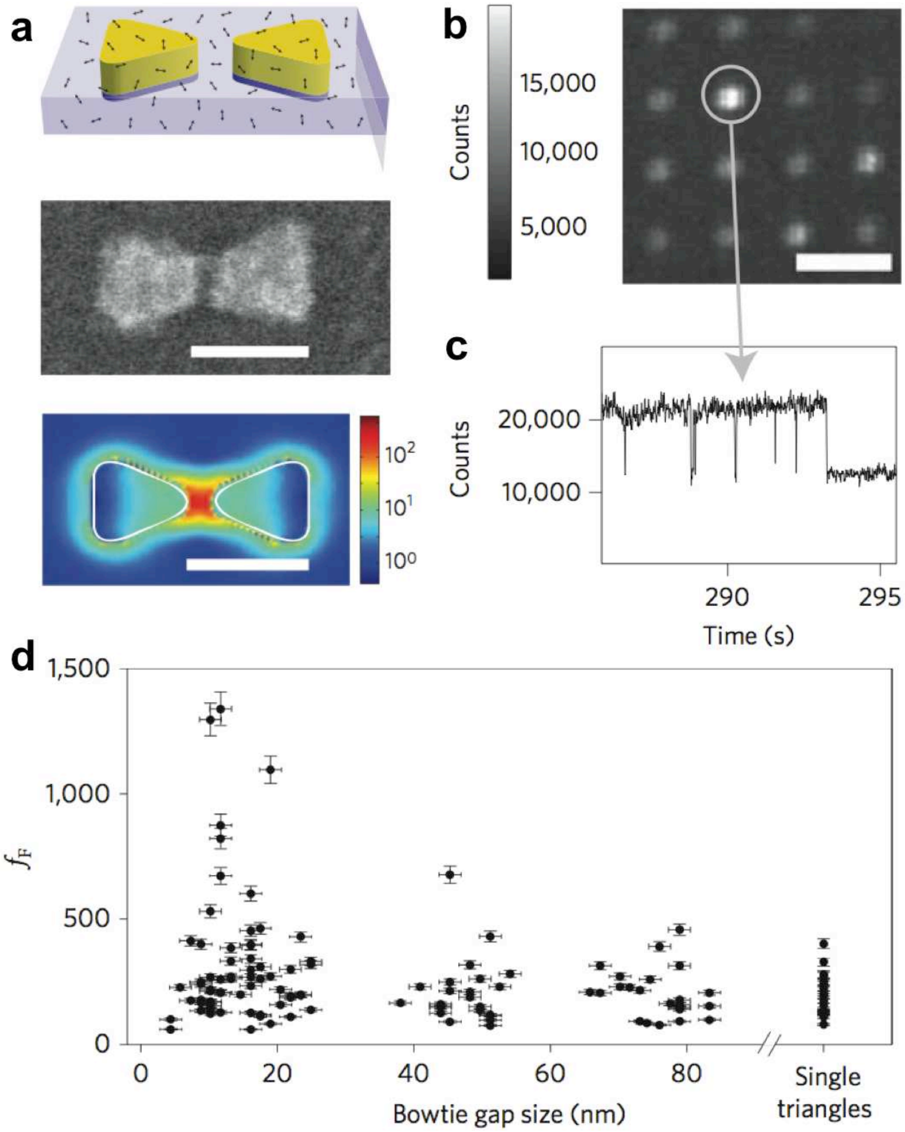

Figure 4.22 Single-molecule fluorescence detection using optical antenna. a, Schematic, SEM, and simulated field intensity distribution of gold bowtie antenna. Scalebar, 100 nm. **b,** Confocal scan of 16 bowtie antennas. EM image of fabricated device. The distance between dashed lines is 50 nm. **c,** Flourescence time trace of the TPQDI/PMMA-coated bowtie antenna circled in (**b**). **d,** Plots of single-molecule fluorescence enhancement as a function of the bowtie gap size [68].

Another potential application using both the receiving and transmitting capability of an optical antenna is SERS. Raman scattering is often called the fingerprint of a molecule since it provides unique spectra of the target molecule. However, the cross section of Raman scattering is so much smaller than that of fluorescence that large enhancement of Raman signals from metallic surface is required for sensitive detection, which is called surface-enhanced Raman scattering. The optical antenna is a powerful tool for application in SERS because it improves both the pump and the emission efficiency. In following chapters, the SERS measurement will be used to verify experimentally the performance of different optical antenna designs.

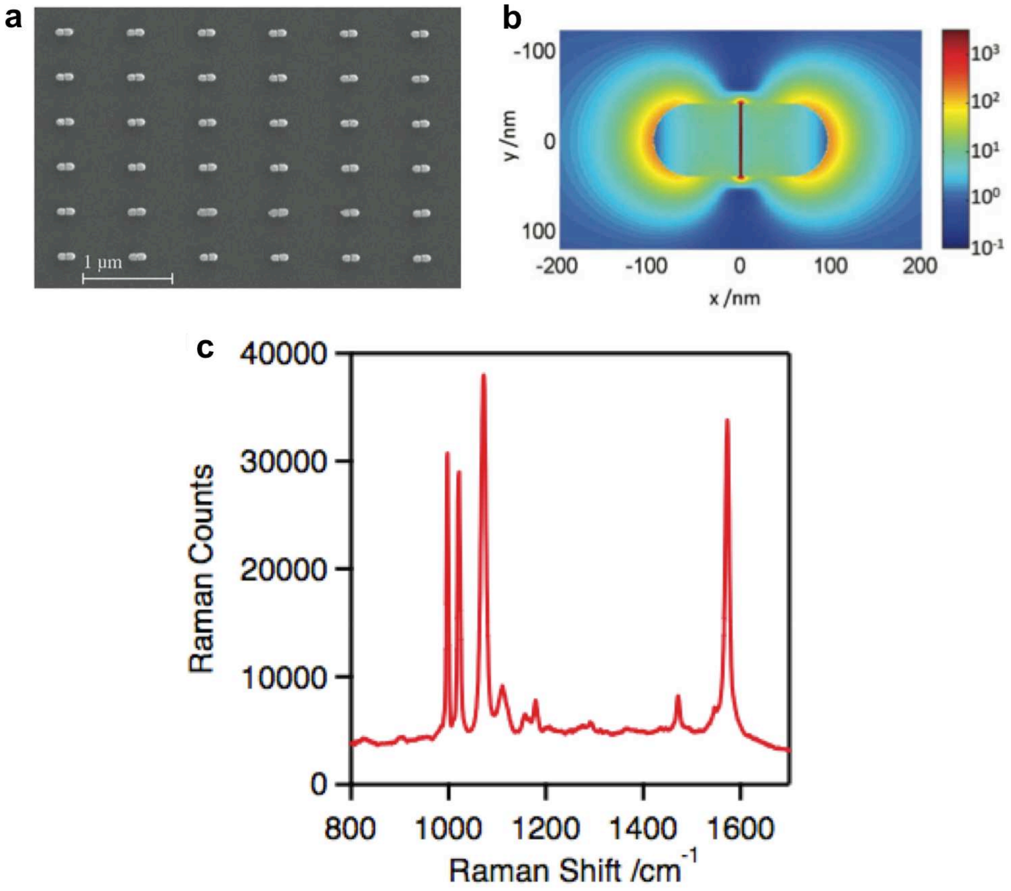

Figure 4.23 Surface-enhanced Raman scattering detection using optical antenna. a, SEM of fabricated gold dipole antenna array. **b,** Simulated electric field intensity distribution of dipole antenna of 3 nm gap. **c,** Benzen-thiol Raman signal measured from fabricated dipole antenna array [59].

Although various optical antenna geometries and applications have been intensively studied over the past few years with many of them seemingly ideal for applications using optical antennas, several challenges remain; (1) there is the reliability issue of reproducible nanoscale dimensions below 10 nm; (2) high production costs must be solved before optical antennas can be employed in real-world applications. These challenges mainly stem from the fabrication method currently used for optical antennas. Because their dimensions are scaled down to a few nanometers (Fig. 4.10), optical antennas are typically fabricated using nano-fabrication techniques such as electron-beam (e-beam) lithography and focused ion beam (FIB) milling. The inherent technical limits in nano-fabrication techniques have, until now, been a serious stumbling block in widespread application of optical antennas.

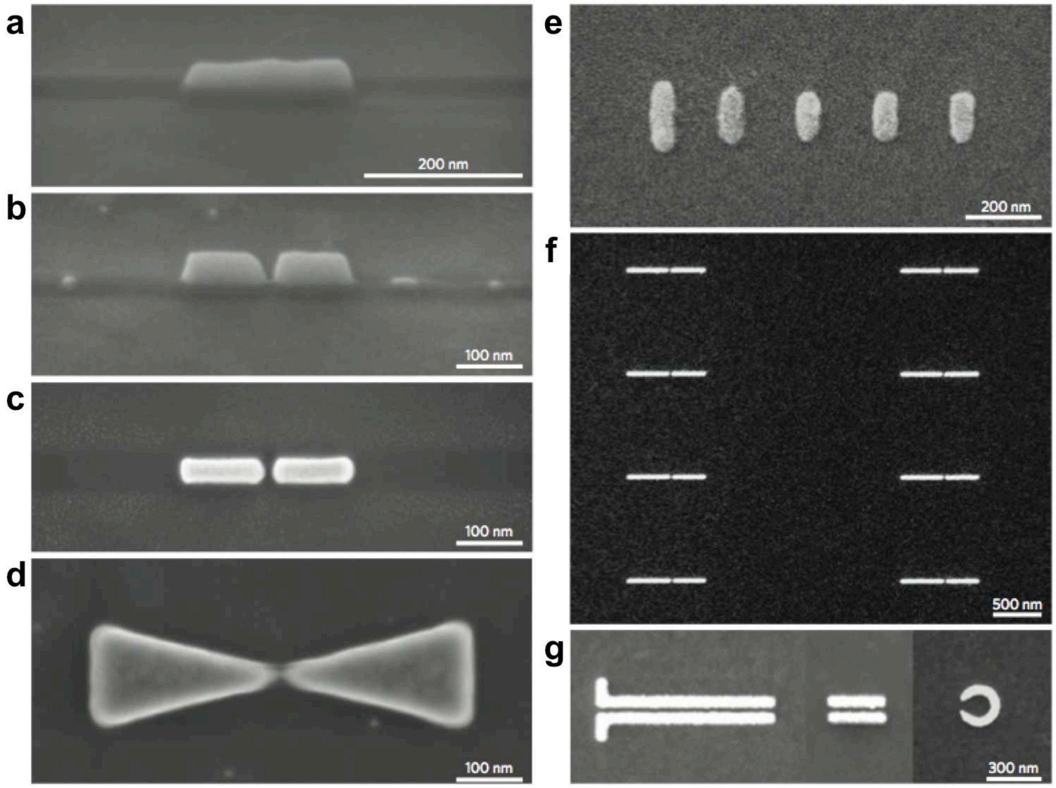

Figure 4.24 SEM images of optical antennas fabricated by nano-fabrication technologies. a-d, Optical antennas fabricated by focused-ion beam milling. **e-g,** Optical antennas fabricated by electron-beam lithography and subsequent lift-off [69].

The first issue to solve is the resolution limit of nano-fabrication techniques. The local field enhancement of an optical antenna is critically dependent on its mode volume. To achieve an extremely small mode volume, optical antennae are usually made with two or more metal particles of nanometer-scale gap between them. In order to improve the performance of an antenna, the gap of the antenna must be reduced further. Fabrication of sub-10 nm gap with good uniformity and reproducibility by e-beam lithography or focused ion beam milling is still a challenge. Innovative fabrication methods to solve this issue are necessary before widespread application of optical antennas can occur.

Another challenge is the fabrication cost for optical antennas. Electron-beam lithography and focused ion beam milling are serial writing processes, which require huge amounts of time and money, and mass production is almost impossible. Although alternative nano-fabrication techniques, such as nanoimprint lithography, have been developed to achieve high-throughput nano-patterning, in general their resolution limit is inferior to e-beam lithography or focused ion beam milling.

Chapter 7 will introduce a novel design and fabrication technique that addresses these challenges.

CHAPTER 5

Optical Dipole Antenna on Ground Plane

The dipole antenna is one of the most common types of antennas, which typically consists of two metal bars with a feed gap between them. Dipole antennas have resonant spectral characteristic and broadside radiation patterns. Due to their relatively simple structure and current distribution, behaviors of dipole antennas have been well understood analytically and practically in radio frequencies. Characteristics of dipole antennas at optical frequencies have been also explored in many materials by changing the antenna dimensions [54], [70], loading the antenna gap with appropriate materials [55], [56], shrinking the size of antenna feed gap [57], [59] and so on. As a result, it has been shown that optical dipole antennas have resonant characteristic similar to their radio frequency counterpart, and strong capability of local field enhancement as a distinct antenna property at optical frequencies.

In this chapter, we report a method for radiation engineering of optical antennas to maximize the local field enhancement. As described in Section 4.3.3, the power dissipated by radiation needs to be matched to the power absorbed by material loss for the maximum field enhancement. To achieve this condition, we must be able to control the radiated power of optical antenna since the absorption is relatively fixed to the material loss of the metal. Here, we show that this can be demonstrated by gold dipole antenna arrays on ground plane. In this structure, the radiation of dipole antenna is controlled by the thickness of the spacer between the antenna array and the ground plane. As an experimental verification of maximum field enhancement, measurements of reflectance and surface-enhanced Raman scattering will be discussed.

5.1 Radiation Engineering Using Ground Plane

From Eq. (4.19), the local field enhancement of optical antenna is given by

$$\frac{|E_{loc}|^2}{|E_i|^2} = \frac{2A_{em}\lambda_{res}Q^2}{\pi Q_{rad}V_{eff}} \qquad (5.114)$$

In order to maximize the field enhancement shown in (5.1), it has been shown that we have to achieve the matching condition between radiation and absorption (Q_{rad}=Q_{abs}) assuming slowly varying A_{em}, V_{eff}, and Q_{abs}. Here, we introduce a ground plane to control the radiation of optical antennas to be matched with the absorption.

As a starting point, we will study the radiation characteristics of a typical optical antenna fabricated on a glass substrate. To estimate the amount of mismatch between Q_{rad} and Q_{abs} for a gold dipole antenna (with 260nm length, 40nm width, 25nm thickness, and 15nm gap) on a quartz glass substrate, we have used time domain simulations based on finite integration technique (CST Microwave Studio) to calculate Q, Q_{rad}, and Q_{abs} as shown in (Fig. 5.1). The total quality factor of the antenna (Q) and the radiation Q of the antenna are calculated to be Q = 10.7 and Q_{rad} = 18.3, respectively. The total quality factor of the antenna, Q, consists of the radiation (Q_{rad}) and absorption (Q_{abs}) with the relation $Q^{-1} = Q_{rad}^{-1} + Q_{abs}^{-1}$. Therefore, the absorption Q of the antenna can be calculated as: $Q_{abs}^{-1} = Q^{-1} - Q_{rad}^{-1} = 10.7^{-1} - 18.3^{-1} = 25.8^{-1}$. This mismatch between the radiation Q and absorption Q reduces the energy coupling into optical antennas, leading to smaller field enhancements.

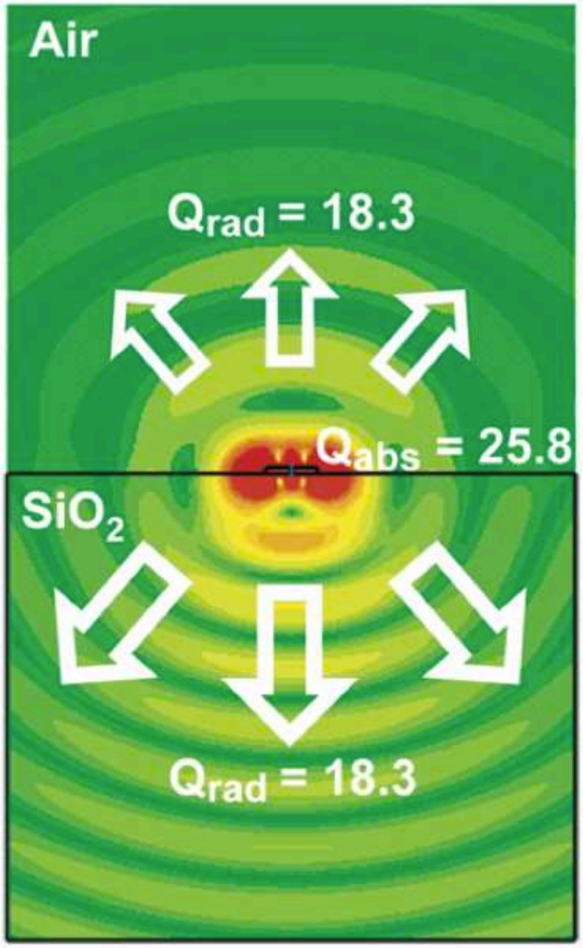

Figure 5.25 Simulation of gold dipole antenna on glass substrate.

To improve the antenna efficiency through Q matching, we need to controllably tune either the radiation Q or absorption Q of the antenna. Since absorption Q of the antenna is dictated by the metal loss (gold or silver) [47], the radiation Q of the antenna needs to be tuned. We achieve this radiation engineering of optical antennas using dielectric spacer coated metal ground planes (Fig. 5.2(a)). Metallic ground planes have been used previously to enhance the fluorescence or SERS of molecules placed a distance of quarter-wavelength ($\lambda/4$) away from the ground plane using a dielectric spacer [71], [72]. The $\lambda/4$ distance results in constructive interference between the top and bottom reflected emissions of the molecule and increases the effective aperture A_{em}. However, in addition to reflecting the bottom radiation, the ground plane can be used to control the radiation Q of the antenna and tune it to match the absorption Q of antenna. For example, as the dielectric spacer thickness is reduced beyond the quarter-wavelength ($\lambda/4$) thickness, the antenna dipole and the antenna image dipole radiation cancel each other more and more (Fig. 5.2(b)). Therefore, as the dielectric spacer thickness is reduced, the radiation Q of the antenna is increased and at the optimum dielectric spacer thickness, the radiation and absorption Q of the antenna would be matched, which leads to the maximum field enhancement condition.

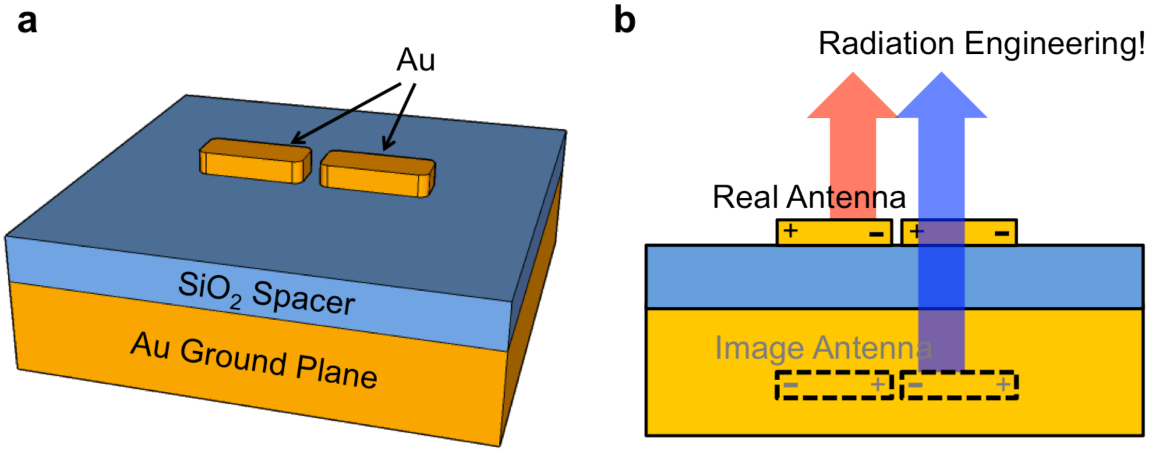

Figure 5.26 Dipole antenna on ground plane. a, Schematic of gold dipole antenna on silicon dioxide coated gold ground plane. **b,** Conceptual picture of radiation engineering.

5.2 Numerical Simulation of Dipole Antenna on Ground Plane

We have used numerical simulation to verify this idea for a gold dipole antenna array on dielectric (SiO_2) coated gold ground plane. Gold dipole antenna arrays with 260nm length, 40nm width, 25nm thickness, 15nm gap, and 600nm pitch as shown in Fig. 5.3(a) were simulated using a finite integration technique based software (CST Microwave Studio). The dipole antenna array is excited by a plane wave from the top which is polarized along with dipole antenna's long axis. As indicated in Fig. 5.3(b), the electric field is mainly confined at the antenna feed gap on resonance.

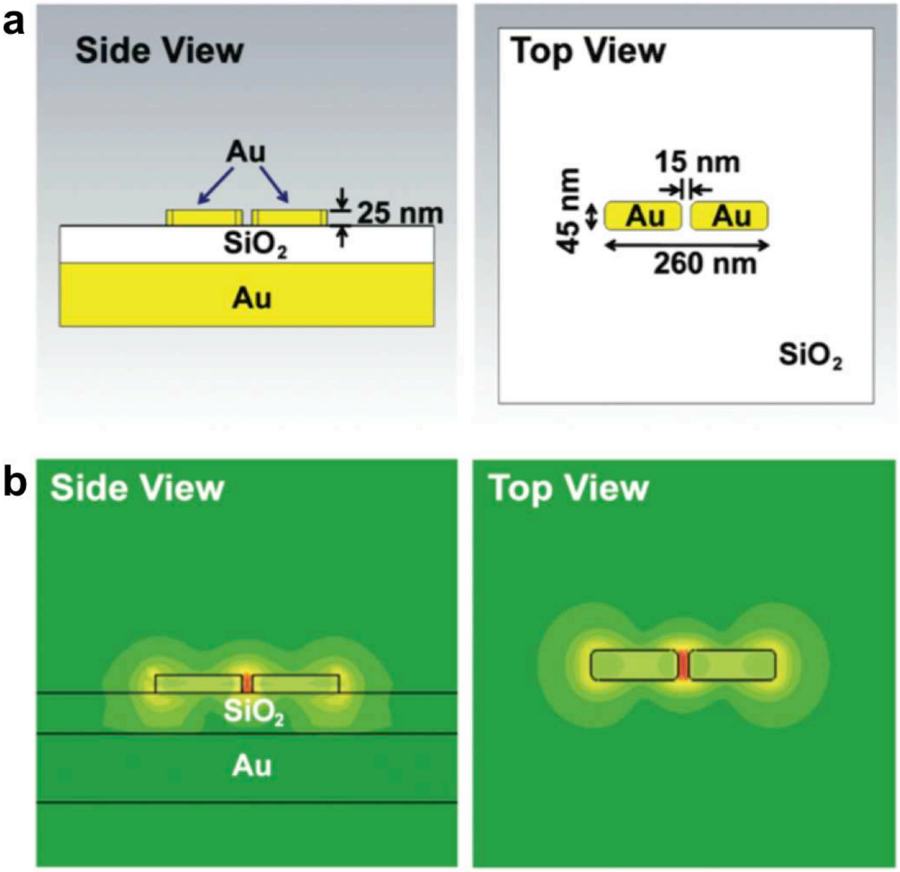

Figure 5.27 Simulation of dipole antenna on ground plane. a, The schematic picture of simulated structure. The260nm long, 45 nm wide, and 25 nm thick gold dipole antennas with 15 nm gap on gold ground plane were simulated using a time domain solver based software. Periodic boundary condition was used to calculate an antenna array with 600 nm pitch. **b,** Electric field magnitude distribution of simulated dipole antennas.

The total Q, radiation Q, and absorption Q of the antenna array are calculated as the thickness of SiO_2 spacer layer is varied from 20nm to 150nm. As shown in Fig. 5.4(a), the radiation Q increases as the thickness of spacer decreases which is expected from the radiation cancellation between the real and the image dipole antenna. The radiation Q matches with the absorption Q at the spacer layer thickness of 60nm. The field intensity enhancement is also maximized at this optimum spacer thickness (60nm) which agrees well with the theory (Fig. 5.4(b)). It is important to note that the optimum dielectric spacer thickness (60nm) is less than half of the quarter-wavelength thickness of 150nm.

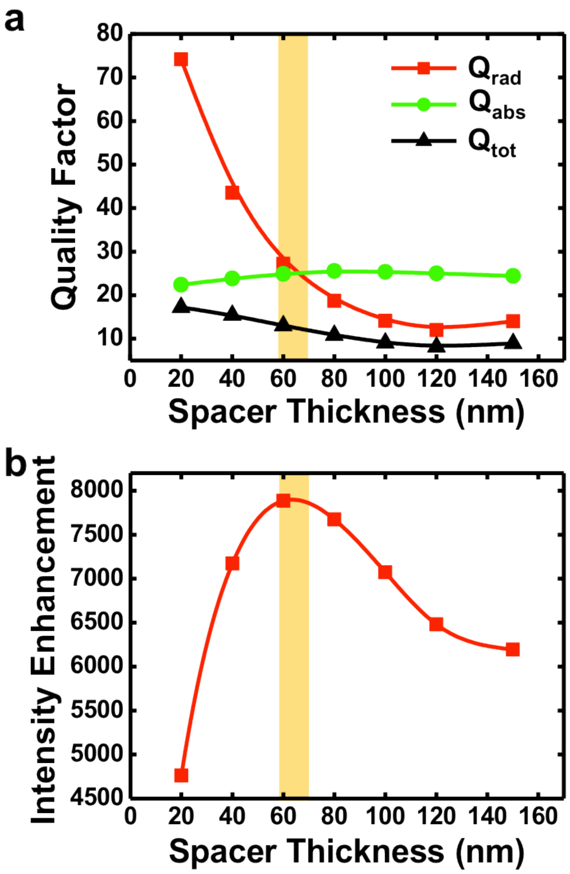

Figure 5.28 Numerical calculation of quality factors and field intensity enhancement. a, Quality factor plot as a function of SiO_2 dielectric spacer thickness. **b,** Field intensity enhancement plot as a function of SiO_2 dielectric spacer thickness. Electric field is measured at the center of dipole antenna gap. The field intensity enhancement has a maximum peak at the optimum spacer thickness for Q-matching ($Q_{rad} = Q_{abs}$) condition.

Before moving to the experimental demonstration of this structure, let us check the validity of the assumption we made when the Q-matching condition was extracted for maximum field enhancement at this point. The assumption we used is that Q_{abs}, A_{em}, and V_{eff} are constants or slowly varying relative to Q_{rad}. At first, it can be confirmed from Fig. 5.4(a) that the variation of Q_{abs} is much smaller than that of Q_{rad}.

For the maximum effective aperture A_{em}, we consider the directivity since the effective aperture is proportional to the directivity. It has been shown that the complete (normalized) pattern of an array antenna is

$$F(\theta,\varphi) = g_a(\theta,\varphi) f(\theta,\varphi) \tag{5.115}$$

where $g_a(\theta, \varphi)$ is the normalized pattern of a single element antenna of the array (the element pattern) and $f(\theta, \varphi)$ is the normalized array factor [43]. The total pattern is dominated by the array factor if the element pattern is much broader than the array factor and the main beams are aligned. Increasing the array size by adding antenna elements narrows the beamwidth of the array factor and increases the directivity ($D = 4\pi / \iint |F(\theta,\varphi)|^2 d\Omega$). If the antenna array is close to infinite, the beamwidth of the array factor becomes extremely narrow and the total radiation pattern becomes approximately a plane wave. Therefore, the antenna arrays with different dielectric spacer layer thicknesses have approximately the same radiation patterns and effective apertures.

Figure 5.5 shows the simulation results (using CST Microwave Studio) for the effective mode volume of an infinite antenna array as a function of various dielectric spacer thicknesses. Even though there is a slight increase in the mode volume as the spacer thicknesses increase (due to the increase in the energy stored in the spacer layer), the mode volume varies slowly over a large range of dielectric spacer thicknesses (20nm to 150nm) which is expected since the majority of the energy is stored in the antenna gap spacing.

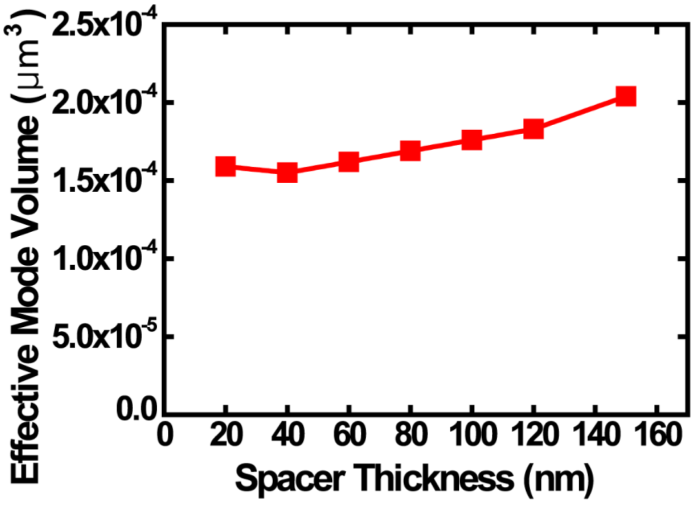

Figure 5.29 Effective mode volume simulations of infinite antenna arrays as a function of dielectric spacer thickness. Gold dipole antenna arrays on gold ground plane were simulated using a time domain solver based software (CST Microwave Studio). Periodic boundary condition was used to calculate an antenna array with 600 nm pitch. The plotted mode volume is calculated for one antenna element in the array.

5.3 Fabrication of Dipole Antenna on Ground Plane

To experimentally verify the *Q*-matching condition, gold optical dipole antenna arrays were fabricated on SiO_2 spacer coated gold ground planes using high resolution e-beam lithography and a lift-off process. For the ground plane, a 100nm thick gold layer was evaporated on a Si wafer, and SiO_2 layers of various thicknesses (20, 60, 100, and 150nm) were deposited using plasma-enhanced chemical vapor deposition (PECVD). We patterned 260nm long and 45nm wide optical dipole antennas using e-beam lithography followed by evaporation of 3nm thick germanium and 25 nm thick gold. Germanium adhesion layers reduce the roughness of gold surface [73] as shown in Fig. 5.6. The total size of the optical antenna array field is 300μm×300μm and identical dipole antennas were distributed with a 600nm pitch (square array). Fig. 3a shows the SEM picture of fabricated optical dipole antenna array and the typical dimensions of a single antenna are shown in the inset. Each antenna has a length of 260nm, width of 45nm, and gap of 15nm.

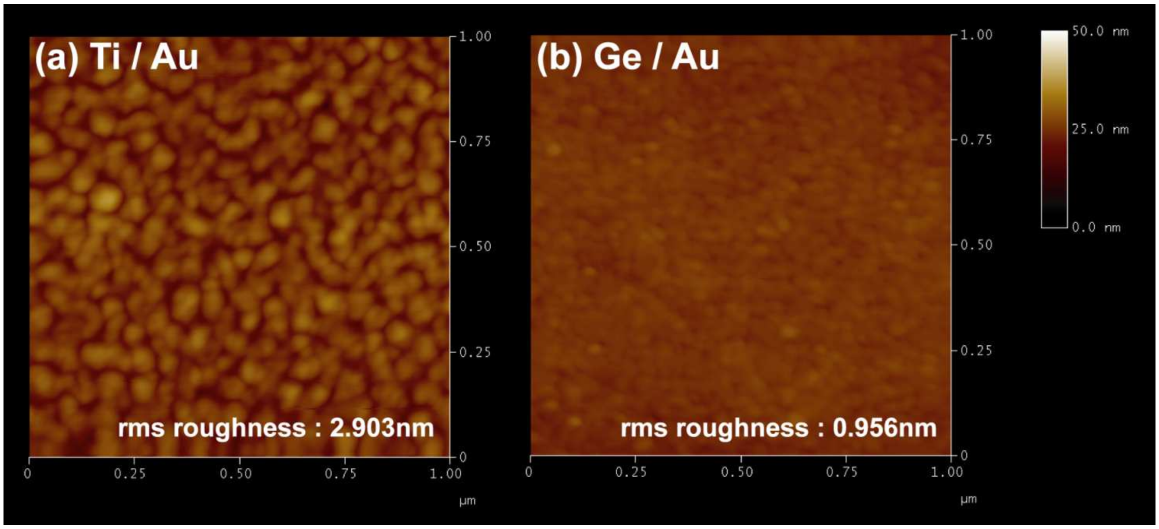

Figure 5.30 Comparison of the gold smoothness for titanium versus germanium adhesion layers. a, AFM measurement of 3 nm Ti and 30 nm Au evaporation on Si substrate. **b,** AFM measurement of 3 nm Ge and 30 nm Au

evaporation on Si substrate. Ge adhesion layer reduces the root-mean-square (rms) surface roughness of the Au layer by 3x compared to Ti adhesion layer.

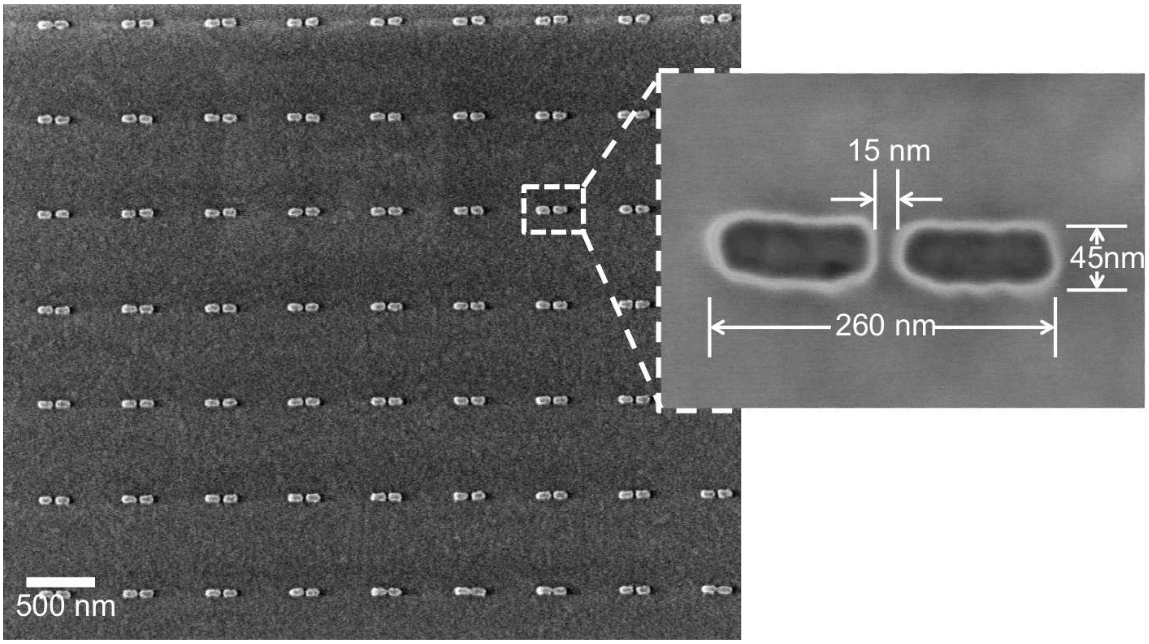

Figure 5.31 SEM image of fabricated dipole antenna array. SEM image of fabricated gold antenna array on a dielectric (SiO_2) coated gold ground plane. The zoomed-in image shows a typical dipole antenna with 260 nm length, 45 nm width, and 15 nm gap.

5.4 Experimental Measurement

5.4.1 Reflectance Measurement

We use reflectance measurements to characterize the optical antennas and the effect of Q-matching since this measurement method is less sensitive to variations in parameters such as gap spacing caused by non-uniformities in e-beam lithography exposure. The illumination from a halogen lamp was focused on the antenna array using a 5×, NA=0.13 objective lens and the reflection from the antenna array was collected through the same objective lens and sent to the spectrometer using a multi-core optical fiber. Fig. 5.8 shows the normalized reflection spectrum (reflectance) of the antenna arrays for various dielectric spacer thicknesses, each spectrum is calculated by dividing the reflection from the antenna arrays with the reflection from an area on the dielectric coated ground plane without any antennas. Reflectance spectra show two major dips for each array. The larger dip position at longer wavelength corresponds to the antenna resonance and smaller dip corresponds to surface plasmon resonance supported by the periodic array.

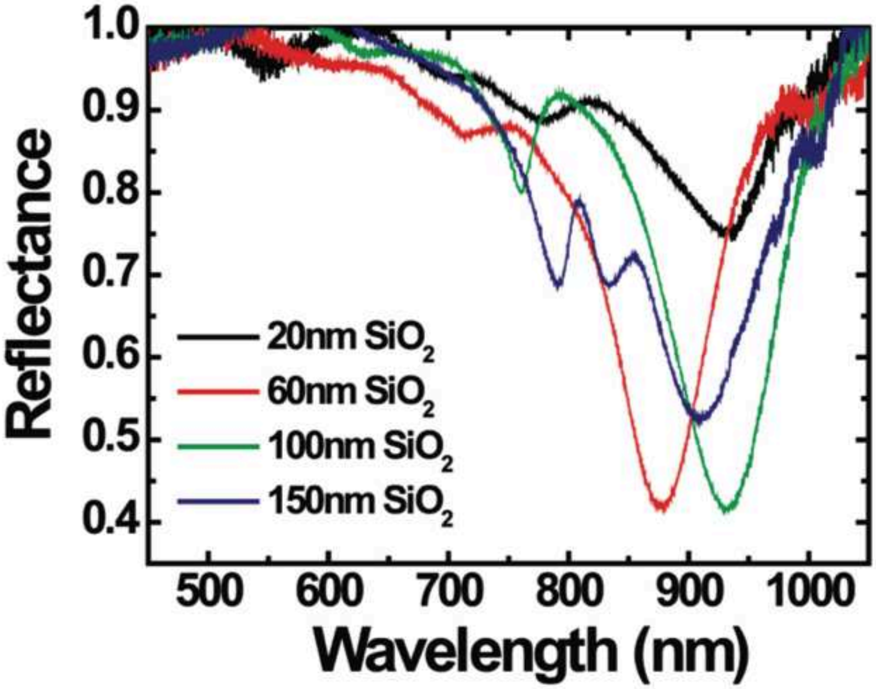

Figure 5.32 Reflectance spectra of dipole antenna arrays for various dielectric (SiO_2) spacer thicknesses. The 60 nm and 100 nm SiO_2 thicknesses display the largest reflection dip, corresponding to the strongest field enhancement as predicted by the theory. Reflectance spectra show two major dips for each array. The larger dip position at longer wavelength corresponds to the antenna resonance and smaller dip corresponds to surface plasmon resonance supported by the periodic array.

5.4.2 Extraction of Quality Factors from Reflectance Measurement

Various parameters such as resonance wavelength, total Q, radiation Q, and absorption Q of the antenna can be extracted from the reflectance measurements. The resonance wavelength and total Q are extracted directly by fitting a Lorentzian curve to the reflectance spectrum. Radiation Q is calculated using reflectance equation from modified coupled-mode theory as the following.

Only a certain portion of the plane wave excitation can couple to the optical antenna array, therefore, we will use the mode that is spatially matched to the antenna radiation pattern, denoted by s_{+rad}, as the input port of our coupled-mode theory framework. The other part of excitation is denoted by $s_{+uncoupled}$, and the modes through the ports s_{+rad} and $s_{+uncoupled}$ are orthogonal since they are not interacting each other. Due to the orthogonality between these modes, the total incident power ($|s_+|^2$) is the sum of the powers from each mode ($|s_+|^2 = |s_{+rad}|^2 + |s_{+uncoupled}|^2$) and the relation between spatially matched input s_{+rad}, and total excitation s_+ is given by $|s_{+rad}|^2/|s_+|^2 = A_{em}/A_i$ where A_{em} and A_i are the maximum effective aperture of the antenna and the area of the excitation beam, respectively. The uncoupled mode ($s_{+uncoupled}$) is assumed to be reflected from the ground plane of the system ($s_{-uncoupled} = -s_{+uncoupled}$). It has been already shown in coupled-mode theory that reflected wave can be expressed as [45]:

$$\begin{aligned} s_{-rad} &= -s_{+rad} + \sqrt{\frac{1}{\tau_{rad}}}\,a = \\ &-s_{+rad} + \frac{\frac{1}{\tau_{rad}}}{j(\omega-\omega_0)+\frac{1}{2}\left(\frac{1}{\tau_{rad}}+\frac{1}{\tau_{abs}}\right)} s_{+rad} \end{aligned} \tag{5.116}$$

where a is the mode amplitude in the cavity and $1/\tau_{rad}$ and $1/\tau_{abs}$ are the rates of decay due to antenna radiation and absorption, respectively. These modes s_{-rad} and $s_{-uncoupled}$ of reflected waves are also orthogonal due to the orthogonality between s_{+rad} and $s_{+uncoupled}$, and the total reflected power becomes the sum of the powers from each reflected mode. Then, we can calculate the reflectance as:

$$\begin{aligned} R(\omega) &= \frac{|s_{-uncoupled}|^2 + |s_{-rad}|^2}{|s_+|^2} \\ &= 1 - \frac{A_{em}}{A_i} + \frac{A_{em}}{A_i}\left|-1 + \frac{\frac{1}{\tau_{rad}}}{j(\omega-\omega_0)+\frac{1}{2}\left(\frac{1}{\tau_{rad}}+\frac{1}{\tau_{abs}}\right)}\right|^2 \\ &= 1 - \frac{A_{em}}{A_i} + \frac{A_{em}}{A_i}\left|-1 + \frac{\frac{\omega}{Q_{rad}}}{j(\omega-\omega_0)+\frac{\omega}{2Q}}\right|^2 \end{aligned} \tag{5.117}$$

On resonance ($\omega = \omega_0$),

$$R(\omega_0) = 1 - \frac{A_{em}}{A_i} + \frac{A_{em}}{A_i}\left|-1 + \frac{2Q}{Q_{rad}}\right|^2 \tag{5.118}$$

$$\therefore 1 - R(\omega_0) = 4\frac{A_{em}}{A_i}\frac{Q}{Q_{rad}}\left(1 - \frac{Q}{Q_{rad}}\right) \tag{5.119}$$

Therefore, the magnitude of reflectance dip (1-R) has the form of a quadratic equation of Q_{rad}. This quadratic equation has a maximum peak at $Q_{rad} = 2Q$ and the maximum peak value is A_{em}/A_i. This condition of maximum peak is exactly identical to the Q matching condition for the maximum field enhancement ($Q_{rad} = Q_{abs}$). With known parameters Q, R, and A_{em}/A_i, we can extract Q_{rad} from this quadratic equation. In fact, two solutions of the quadratic equation represent Q_{rad} and Q_{abs} due to mathematical symmetry of these two quality factors. The larger solution is Q_{rad} for the undercoupled case, and the smaller solution is Q_{rad} for the overcoupled case. Total quality factor Q and reflectance R can be extracted from a Lorentzian fit of the measured reflectance spectrum. Coupling ratio A_{em}/A_i cannot reach 1 since there exists spatial mismatch between excitation light and antenna radiation pattern due to finite size of antenna array and fabrication variations from individual antennas. We assume that A_{em}/A_i has the value of 0.65 from the maximum peak of Fig. 5.9(b).

Using the equation (5.1), we find that

$$\begin{aligned}1 - R = 4\frac{A_{em}}{A_i}\frac{Q}{Q_{rad}}\left(1 - \frac{Q}{Q_{rad}}\right) &= 4\frac{A_{em}}{A_i}\frac{Q}{Q_{rad}}\frac{Q}{Q_{abs}} \\ &= \frac{2\pi V_{eff}}{A_i\lambda_{res}Q_{abs}}\frac{|E_{loc}|^2}{|E_i|^2}\end{aligned} \qquad (5.120)$$

Therefore, the magnitude of reflectance dip is linearly proportional to field intensity enhancement. Consequently, we can assume that the field enhancement is also maximized when the size of the reflectance dip is maximized.

Note that the reflectance dip can be also rewritten using the absorption cross section σ_{abs} as

$$1 - R = 4\frac{A_{em}}{A_i}\frac{Q}{Q_{rad}}\frac{Q}{Q_{abs}} = \frac{\sigma_{abs}}{A_i} \qquad (5.121)$$

The extracted radiation Q, absorption Q, and total Q of the antenna arrays are shown in Fig. 5.9(a) as a function of dielectric spacer thickness. The optimum dielectric spacer thickness at which the antenna array's radiation Q and the absorption Q are matched is approximately 80nm. The size of dip in the reflectance measurements is proportional to the maximum field enhancement, as shown in Fig. 5.9(b), the maximum dip in reflectance measurement is also achieved for a dielectric spacer close to 80nm which is consistent with the Q-matching condition. It is important to note that this optimum thickness (~80nm) is roughly half of the quarter-wavelength thickness and results in approximately 20% larger field enhancement.

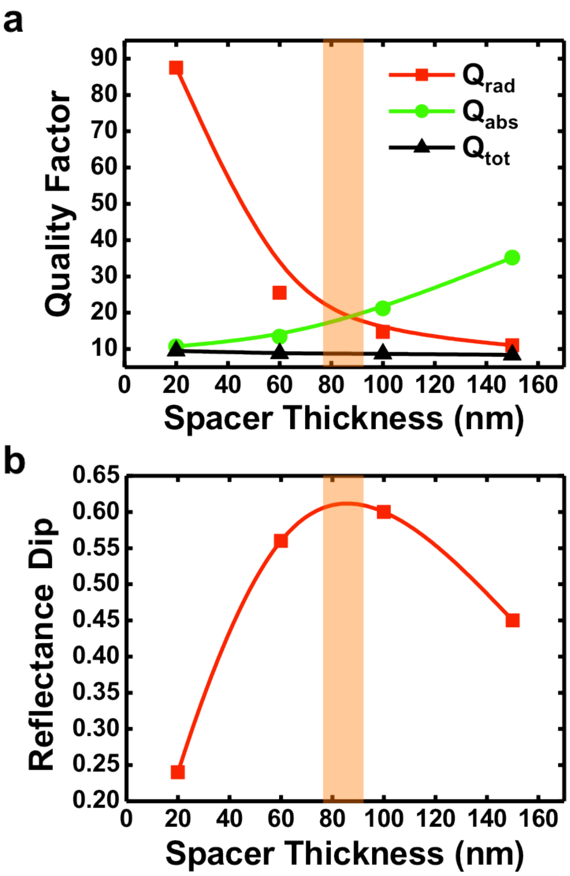

Figure 5.33 Experimental values of quality factors and reflectance dip. a, Experimental values of radiation, absorption, and total quality factors as a function of the dielectric spacer thickness. The trend follows closely the simulation with the Q-matching ($Q_{rad} = Q_{abs}$) condition achieved at ~80 nm dielectric thickness. **b,** Reflectance dip of optical antennas as a function of the dielectric spacer. The maximum reflectance dip, corresponding to maximum field enhancement, is achieved for the Q-matched dielectric thickness.

5.4.3 SERS Measurement

For additional experimental verification of antenna performance, surface-enhanced Raman scattering (SERS) was measured from fabricated optical antenna arrays. SERS has been known as a powerful technique to detect biological and chemical molecule as Raman spectrum provides a unique fingerprint of the target molecule. In order to enhance the sensitivity of SERS, various approaches such as rough surface of metal layer [74], [75], metal nanoparticle aggregates [76], [77], and

DNA-tailored nanoparticle synthesis [58], [78] have been previously studied. Though these methods could promise high SERS enhancement enabling single molecule detection, the controllability of hot spot locations still remains challenging [79]. To address this challenge, top-down fabrication of optical antennas has been used to generate SERS hotspots with the engineered spatial arrangement and the reproducible enhancement factors [59]–[61], [65], [32].

We used *trans*-1,2-bis (4-pyridyl) ethylene (BPE) as the target molecule of SERS measurement. For the sample preparation, fabricated antenna arrays were immersed in a 6 mM solution of BPE in methanol for 2 hours. After 2 hours incubation, the samples were rinsed using methanol, and then blow-dried with nitrogen gun. The excitation from 785 nm laser was focused on the antenna array using a 10x objective and the Raman signal was collected through the same objective lens for 10 sec for SERS measurement. Measured SERS signals from dipole antenna arrays with different spacer thicknesses are plotted in Fig. 5.10(a). The strongest SERS signal is measured from the dipole antenna array on 100 nm thick spacer layer (Fig. 5.10(b)). This is because the radiation quality factor becomes equal to the absorption quality factor around this spacer thickness, which agrees well with the tendency of reflectance measurement.

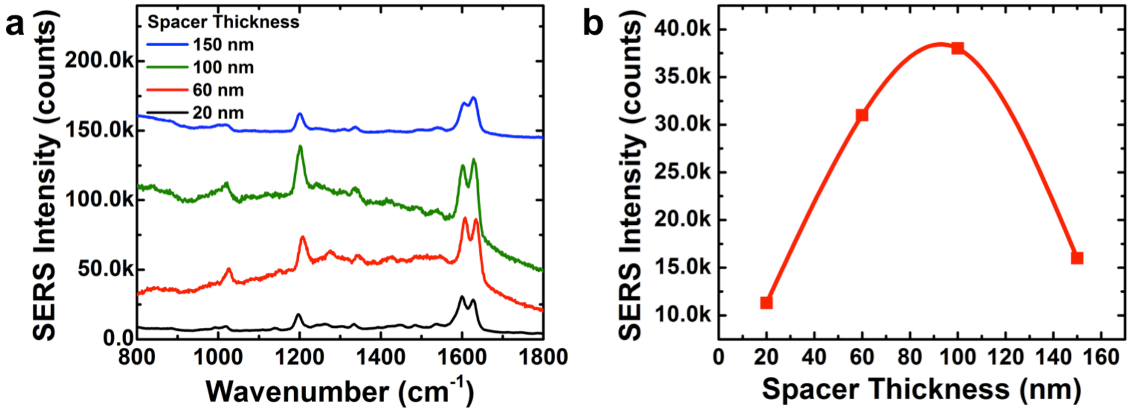

Figure 5.34 SERS measurement from dipole antenna arrays. a, Measured BPE SERS spectra from fabricated gold dipole antenna arrays with various spacer thicknesses. **b,** 1200 cm^{-1} peak SERS intensity as a function of the spacer thickness. The SERS signal is maximized when the spacer thickness becomes around 100 nm, which achieves matched quality factors of radiation and absorption.

From the measured SERS spectra, SERS enhancement factor has been calculated using the following equation,

$$EF = \frac{I_{SERS}}{I_{neat}} \times \frac{N_{neat}}{N_{SERS}} \tag{5.122}$$

where I_{SERS} and I_{neat} are the Raman intensities of the SERS and neat signals of the 1200 cm^{-1} peak, and N_{SERS} and N_{neat} are the numbers of BPE molecules contributing to the SERS and neat Raman signals. For N_{SERS}, the monolayer coating of BPE molecules was assumed with the packing density of 3.30×10^6 µm^{-2} [80]. The number of molecules on entire antenna surfaces was taken account to calculate average SERS enhancement factor. The calculated SERS enhancement factors are plotted as a function of dielectric thickness in Fig. 5.11. The best SERS enhancement factor is observed to be 3.4×10^6 from the dipole antenna array of the 100 nm thick spacer.

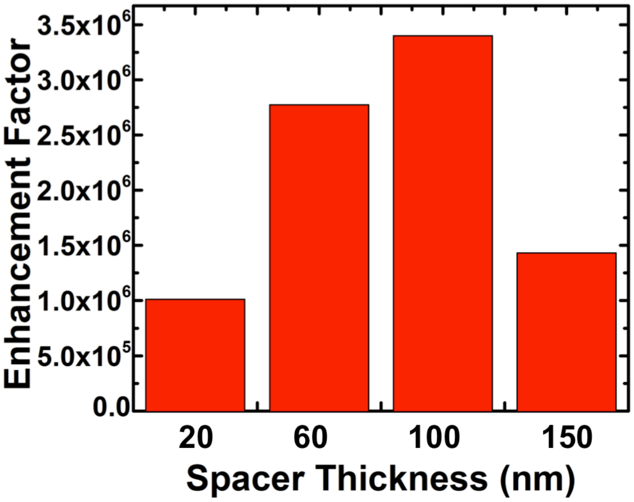

Figure 5.35 Measured SERS enhancement factor of dipole antenna arrays. The SERS enhancement factors are calculated using Raman signal intensity of 1200 cm^{-1} peak.

5.5 Summary

In summary, a new condition to achieve maximum field enhancement for optical antennae through matching the radiation Q and absorption Q of the antenna has been introduced. This matching is achieved experimentally by fabricating an array of dipole antennas on a dielectric coated ground plane and tuning the thickness of the dielectric spacer to control the antenna's radiation Q. For the experimental characterization, reflectance and the SERS signal obtained from the BPE molecule are measured from the fabricated dipole antenna arrays with various spacer thicknesses. A comparison of the reflectance dip and 1200 cm^{-1} Raman peak intensity are plotted in Fig. 5.12. In this plot, the square of the reflectance dip is taken into the account since the reflectance dip is proportional to field intensity enhancement, whereas the SERS signal is proportional to the square of field intensity enhancement. Both measurements show similar trends in the spacer thickness variation, which indicates that the maximum field enhancement is achieved at the optimum dielectric thickness of ~80nm with the Q-matching condition $Q_{rad} = Q_{abs}$. This is slightly higher than the optimum thickness obtained from the simulation and is probably due to the loss of fabricated metal, which was greater in the simulation compared to the theoretical value. In general, however, the trends showed good agreement between the theory and simulated values. The optimum spacer thickness is ~50% smaller than the quarter-wavelength thickness.

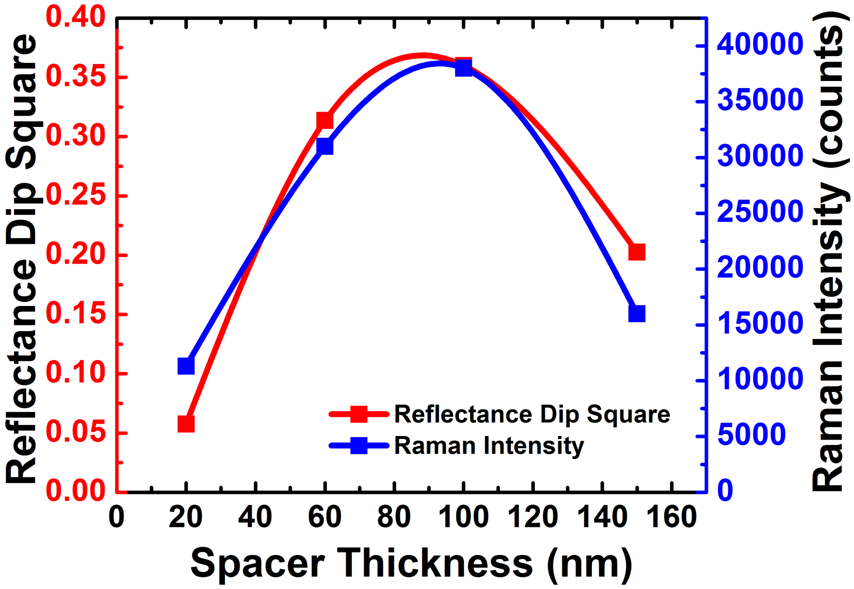

Figure 5.36 Comparison between reflectance and SERS enhancement. Reflectance and SERS measurements show similar trends in the spacer thickness variation, which indicates that the maximum field enhancement is achieved at the optimum dielectric thickness of ~80nm with the Q-matching condition $Q_{rad} = Q_{abs}$.

CHAPTER 6

Optical Patch Antenna

In the previous chapter, the field enhancement of an optical antenna was optimized when the amount of radiation was matched to that of absorption. In order to control the radiation property of an optical antenna, dipole antenna arrays were implemented on a ground plane and tuned the thickness of the spacer layer between the antenna array and the ground plane. From the experimental study of reflectance and the SERS measurements, we demonstrated that the enhancement is maximized at the optimum thickness of dielectric spacer layer.

Although the local field enhancement for the given dipole antenna design is achieved by engineering radiation of the antenna, the measured SERS enhancement factor ($\sim 10^6$) is still inferior to SERS substrates despite having been assembled using nanoparticles with nanometer-scale gaps. This is because the enhancement is critically dependent on the gap spacing of the dipole antenna. The gap spacing of the fabricated dipole antennas was chosen to have dimensions of ~15 nm, which is relatively reproducible using electron-beam lithography. To approach the enhancement level of single molecule detection, however, the gap spacing of the optical antenna must be reduced further. Current nano-fabrication techniques such as electron-lithography and focused ion beam milling, cannot readily reduce the gap spacing and achieving uniformity for sub-10 nm dimensions is limited

In this chapter, we discuss a method to resolve this fabrication issue by introducing a different design: the optical patch antenna where the gap spacing is defined by the dielectric spacer layer.

6.1 Optical Patch Antenna for Uniform Sub-5 nm Gap Spacing

To demonstrate the efficacy of a uniform and reproducible antenna gap, we investigate an optical patch antenna that consists of a nanopatch on top of a ground plane (Fig. 6.1). The gap spacing of the patch antenna is defined vertically by the thickness of dielectric layer between the patch and the ground plane. Although similar designs of nanodisk arrays on dielectric coated ground planes have been reported by Chu et al. [65], [81], the physical approach to achieve high field enhancement is different. The patch antenna design investigated here aims to improve the field enhancement by realizing sub-5 nm gap spacing for the antenna resonance mode. Chu et al. used double resonances by interaction between antenna resonance mode and surface plasmon mode, and their structures have relatively thick dielectric spacer layers (~30 nm).

For the patch antenna design investigated here, it was essential to reproduce the uniform and reproducible formation of gap spacing with the precise control over the dimensions of the gap spacing. Since the gap dielectric layer is deposited by atomic layer deposition (ALD), which has sub-nm accuracy of the thickness control, optical antennas with a uniform sub-5 nm gap can be easily reproduced.

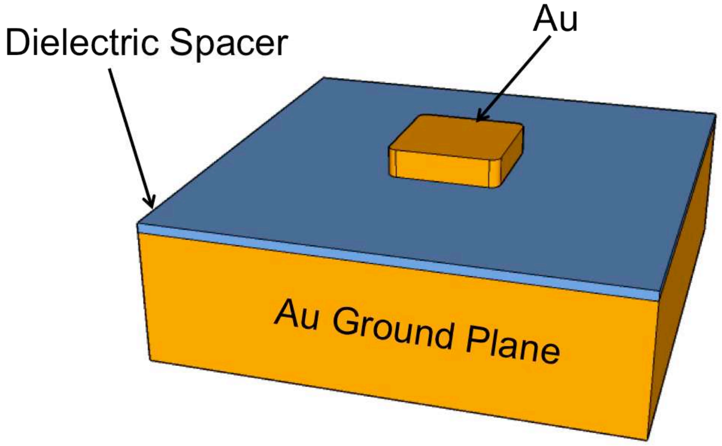

Figure 6.37 Schematic of optical patch antenna. The vertical gap spacing of the patch antenna is defined by the thickness of the dielectric spacer layer.

6.2 Numerical Simulation of Patch Antenna

In order to investigate the field enhancement of the patch antenna, numerical simulations of patch antenna array with various gap spacings (1, 2, 5, 10, and 20 nm) were studied, using the time domain simulation tool based on finite integration technique (CST Microwave Studio). A gold square patch of 60 nm × 60 nm area and 25 nm thickness was placed on top of the dielectric spacer layer coated gold ground plane, as shown in Fig. 6.1. The dielectric spacer material was chosen to be aluminum oxide with a refractive index of 1.76, which can be deposited by atomic layer deposition. The material property of the gold was modeled from experimental value [33]. The periodic boundary condition was used to simulate an infinite antenna array with a period of 300 nm.

Figure 6.2 shows the simulation result of patch antenna array, where the electric field of a patch antenna is well confined in the vertical gap between the patch antenna and the ground plane on resonance. However, the radiation efficiency of patch antenna is very poor and deteriorates even further when the gap spacing is reduced. This can be explained as follows: the image current in the bottom ground plane causes a destructive interference with the radiation of patch antenna, which is similar to the case of a dipole antenna array on ground plane. As a result, the mismatch between radiation and absorption quality factors increases as the gap spacing is reduced below 2 nm; this suppresses the increasing ratio of the field enhancement, as shown in Fig. 6.2(b) and 6.2(c).

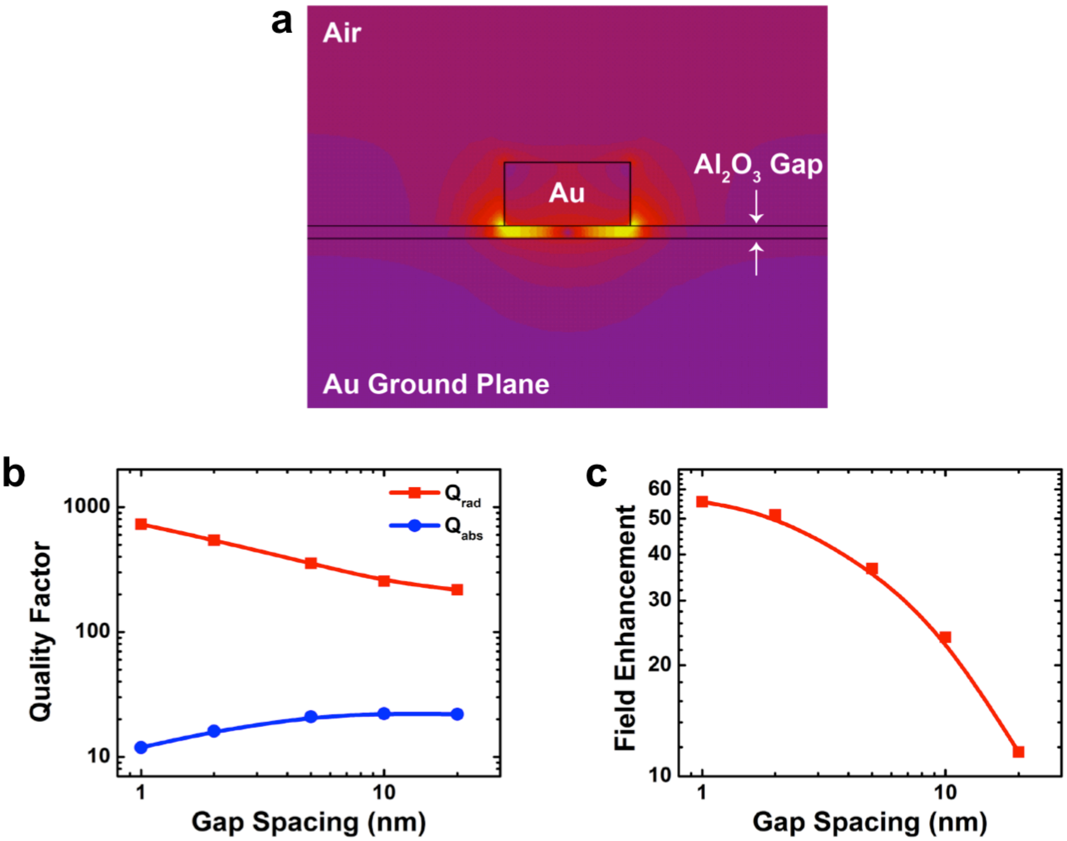

Figure 6.38 Simulation of patch antenna. a, Electric field profile of Au patch antenna. Patch antennas with dimensions of 50 nm square size, 25 nm thickness, and 5 nm Al_2O_3 gap were simulated with periodic boundary condition of 300 nm pitch. **b,** Plot of calculated radiation and absorption quality factors as a function of gap spacing. **c,** Plot of electric field enhancement as a function of gap spacing. Patch antenna arrays with various gap spacings (1, 2, 5, 10, and 20 nm) were simulated. Due to the growing mismatch between radiation and absorption quality factors, the increasing ratio of the field enhancement is suppressed as the gap is reduced below 2 nm.

6.3 Fabrication of Patch Antenna

Optical patch antenna arrays were fabricated using typical high-resolution electron-beam lithography and a subsequent lift-off process. For preparation of gold ground plane, a 100-nm-thick layer of thermal oxide was grown on top of a bare silicon wafer. A 10-nm-thick titanium layer was deposited as the adhesion layer by an electron-beam evaporator, which was followed by the evaporation of a 100 nm thick gold layer with the evaporation rate of ~2 Å/s. The thermal oxide layer between the silicon wafer and the ground plane was introduced to prevent the formation of eutectic bonding between the silicon and gold during the subsequent deposition step at the elevated temperature, which might have roughen the surface of gold ground plane.

The aluminum oxide spacer layer on top of the gold ground plane was deposited by atomic layer deposition (ALD). In ALD process, the thickness of deposited layer is determined by the number of reaction pulse cycles. The ALD recipe of deposition rate 0.1 nm/cycle at 300°C was used for to deposit the aluminum oxide layers. At this step, samples with different aluminum oxide thicknesses of 1, 2, and 5 nm were prepared to investigate the antenna performance as a function of gap spacing.

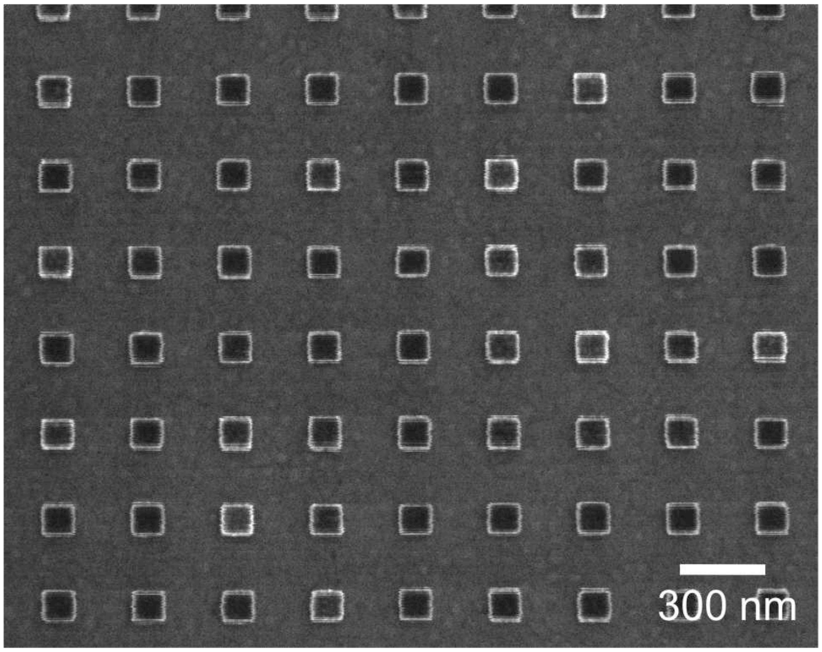

Figure 6.39 SEM image of fabricated patch antenna array.

On top of these substrates, patch antenna arrays were patterned by e-beam lithography. A 70-nm-thick PMMA layer was spun on the substrate for the lithography and patch antenna arrays with a 300-nm period, and various square patch sizes. Then, 2 nm germanium and 25 nm gold layers ware evaporated with the deposition rate of ~1 Å/s and ~2 Å/s, respectively, followed by lift-off step in acetone. A representative SEM image of a fabricated patch antenna array is shown in Fig. 6.3.

6.4 Experimental Measurement

6.4.1 Reflectance Measurement

Reflectance spectra from fabricated patch antenna arrays were measured to characterize antenna resonance. For the white light illumination, light from a halogen lamp was focused using a 50× objective lens and illuminated on a patch antenna array. The reflected light from the sample was collected through the same lens and guided using a multi-core optical fiber to a spectrometer with liquid nitrogen-cooled CCD camera. The reflectance was calculated by dividing the reflection spectrum from the antenna array with the reflection spectrum from the area without antenna arrays.

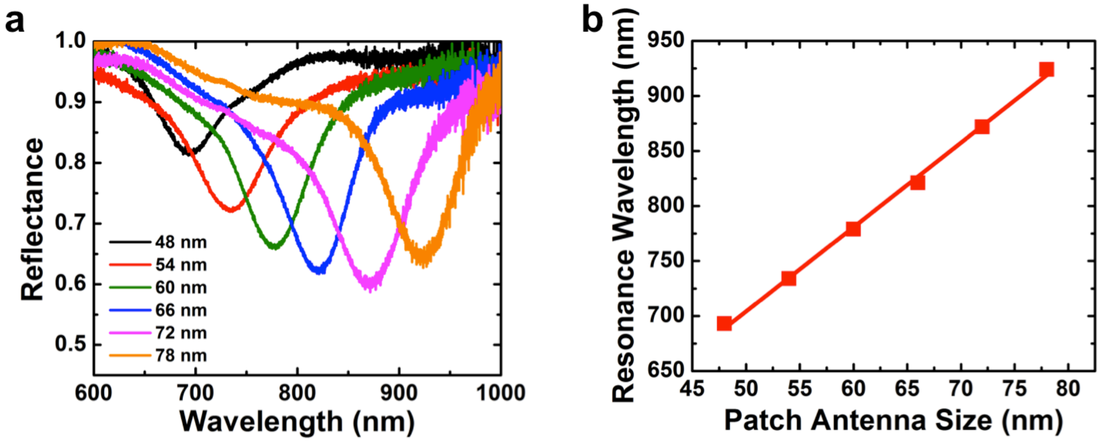

Figure 6.40 Reflectance measurement of patch antenna arrays. a, Reflectance spectra from patch antenna arrays with various patch antenna sizes. **b,** Plot of resonance wavelength as a function of patch antenna size. These spectra were measured from patch antenna arrays on top of 5 nm thick dielectric spacer coated ground plane.

Reflectance spectra measured from patch antenna arrays on the 5-nm-thick spacer-coated ground plane are shown in Fig. 6.4(a). Patch antenna arrays show apparent resonant characteristics; as expected, the resonance wavelength is red-shifted with increasing the patch size. Figure 6.4(b) shows that the resonance wavelength depends linearly on the size of patch antenna.

As shown in Section 5.3.2, the magnitude of the reflectance dip is closely related to quality factors, which is given by

$$1 - R = 4\frac{A_{em}}{A_i}\frac{Q}{Q_{rad}}\frac{Q}{Q_{abs}} \qquad (6.123)$$

This quantity is maximized when the Q-matching condition is achieved. However, the patch antenna exhibited poor radiation efficiency upon reduction of the gap to the nanometer-scale; this results in a huge mismatch between radiation and absorption Q, degrading the magnitude of reflectance dip. Figure 6.5 = compares the reflectance spectra obtained from 1- and 5-nm patch antenna arrays. The 5-nm gap patch antenna has a reflectance dip ~3.6 times larger than that of the 1-nm gap patch antenna. To compare this experimental result with previous simulations, we calculated the term $Q^2/Q_{rad}Q_{abs}$ in Eq. (6.1) using the quality factors obtained from the numerical simulation [see Fig. 6.2(b)]. We find that $Q^2/Q_{rad}Q_{abs}$ is calculated to be $11.7^2/(729\times11.9) = 0.0158$ and $19.8^2/(355\times21.0) = 0.0526$ for 1- and 5-nm gap patch antenna, respectively. Therefore, the theoretical calculation predicts that the ratio of reflectance dip is 0.0526/0.0158 = 3.33, which agrees well with the experimental result (~3.6).

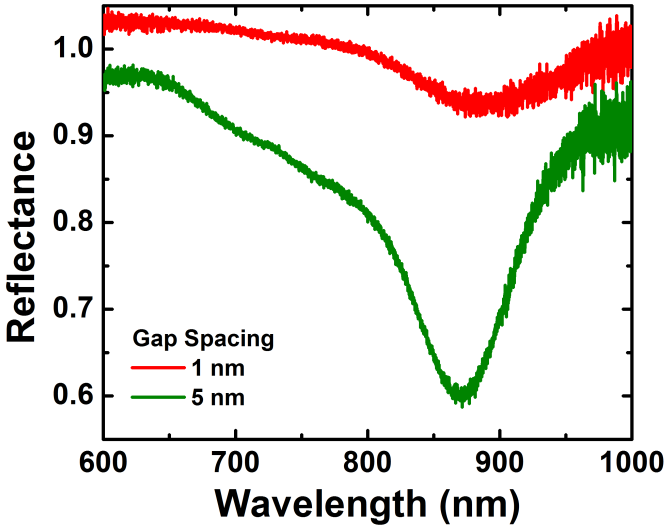

Figure 6.41 Comparison of reflectance spectra measured from 1 and 5 nm gap patch antenna arrays.

6.4.2 SERS Measurement

Surface-enhanced Raman signal of a *trans*-1,2-bis (4-pyridyl) ethylene (BPE) molecule was measured from patch antenna arrays. For the sample treatment, fabricated patch antenna arrays were incubated for two hours in a 6=mM BPE solution. After having been rinsed by methanol for one minute, samples were dried using a nitrogen gun. For the SERS measurement, a 785-nm laser was focused on the samples using 10× objective lens. The SERS signal obtained from the antenna arrays was collected by the same objective lens and sent to the spectrometer for a 10-sec integration.

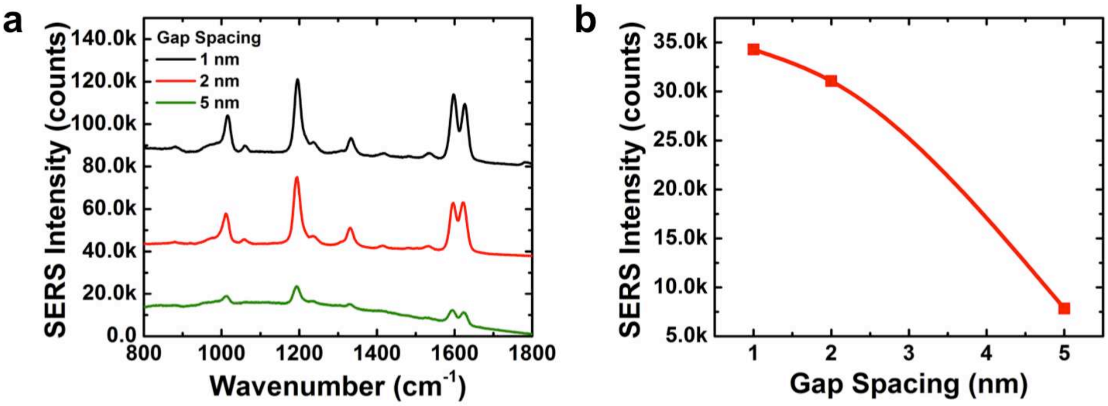

Figure 6.42 SERS measurement from patch antenna arrays. a, Measured BPE SERS spectra from fabricated gold patch antenna arrays with various gap spacings. **b,** 1200 cm^{-1} peak SERS intensity as a function of the gap spacing. The SERS signal is enhanced as the gap spacing is reduced.

Figure 6.6(a) shows the SERS spectra measured from the patch antenna arrays of 1-, 2-, and 5-nm gap spacings. Since a patch antenna experiences resonance-shift with varying gap size, we selected the best SERS signal from the optimum patch size for each gap spacing. The 1200 cm^{-1} Raman peak was chosen to compare the SERS intensity measured from the patch antenna arrays with different gaps. As shown in Fig. 6.6(b), the SERS signal was measured to be five times stronger as the gap spacing was reduced from 5 nm to 2 nm. However, the only a 10% increase of the SERS signal was observed when the gap spacing was reduced to 1 nm from 2 nm. This trend is expected given the poor radiation efficiency of the patch antenna with the nanometer-scale gap. The SERS enhancement factor from the 1-nm gap patch antenna was calculated to be 1.5×10^7, which is about an order of magnitude improved compared to the dipole antenna presented in Chapter 5. This implies that the extremely small gap (1 nm) overcomes the poor radiation efficiency of the patch antenna and contributes to the improvement provided by the SERS enhancement.

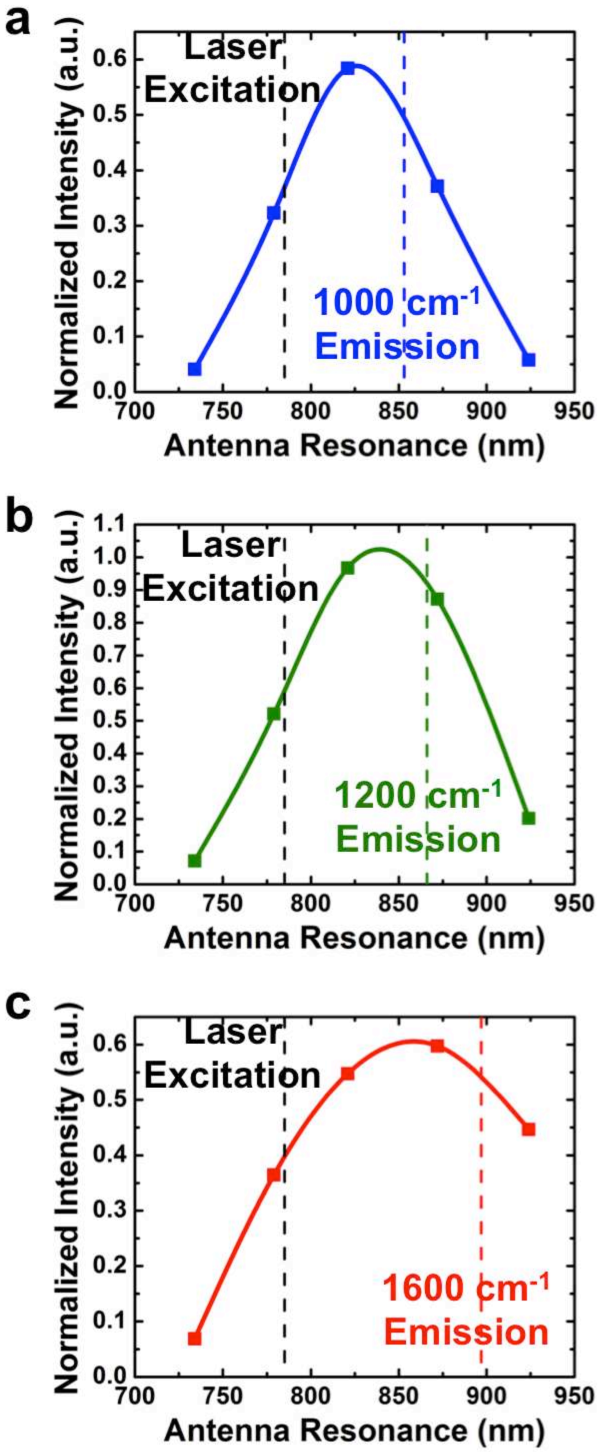

Figure 6.43 Measured SERS intensity as a function of antenna resonance. a, BPE SERS signal of 1000 cm^{-1} Stokes shift peak. **b,** 1200 cm^{-1} Stokes shift peak. **c,** 1600 cm^{-1} Stokes shift peak. SERS signal counts were normalized by the number of molecule on the patch antenna surface assuming monolayer-coating.

The patch antenna design can be also useful in investigating the correlation between the SERS enhancement and antenna resonance. The spectral response of an optical antenna array is often broadened by dimensional variation of individual antennas in the array. For example, the resonance of a dipole antenna is critically dependent on the dimensions of its length and gap. The resonances of individual antennas vary depending on variations in fabrication. This dimensional variation is more significant for the antenna gap, which usually requires being fabricated at the technical resolution limit. The patch antenna design is limited by this fact because the formation of extremely uniform gap is possible by atomic layer deposition. Therefore, a patch antenna array can exhibit a well-defined single resonance without the serious fabrication challenges, as shown in Fig. 6.4(a). Using this factor unique to the patch antenna array, next we discuss the effect of antenna resonance on the SERS enhancement.

It is clear from Fig. 6.5 that the resonance of patch antenna can be tuned by changing their lateral dimension. Here, we investigated SERS signals measured from patch antenna arrays as a function of antenna resonance. The BPE molecule has three main Stokes shift peaks at 1000 cm^{-1}, 1200 cm^{-1}, and 1600 cm^{-1} wavenumbers. As shown in Fig. 6.7, the SERS intensities of these peaks measured from the patch antenna arrays were plotted as a function of antenna resonance. The positions of the excitation laser wavelength and Stokes shift peaks are marked with dashed lines in the plots. Here, the SERS signal intensity was normalized by the number of BPE molecules assuming monolayer coating for fair comparison between patch antennas of different sizes. As expected, a weak SERS signal is observed when the resonance of antenna is far from both the excitation and emission wavelengths. The SERS intensity was optimized when the antenna resonance was placed close to the middle of the excitation and emission wavelengths, indicating that the resonance of an optical antenna must be carefully tuned for SERS applications.

6.5 Optical Patch Antenna for Colorimetric Biochemical Sensor

6.5.1 Nanoparticles for Biochemical Sensing

Metal nanoparticles have been studied as an application for the optical detection of sensitive biochemical sensing as they can efficiently scatters and absorbs light at a certain wavelength depending on the materials and dimensions of the nanoparticles [Fig. 6.8(a)]. For sensing applications, the spectral response of nanoparticles is analyzed with the change of their environment. The shift of nanoparticle resonance provides the information of sensing specimen [82], [31]. In a number of cases using of this approach, equipment for spectral analysis such as a spectrometer is required for the precise detection of the resonance shift. For real-life applications [such as point-of-care testing (POCT)], the potential impact would be much strong if the detection scheme did not require specialized measurements like spectrum analysis. One of the methods to address this issue is colorimetric sensing from a nanoparticle. Even though the scattering cross section of single particle is too tiny to represent a certain color detectable by the human eye, a large number of nanoparticles in solution can represent their characteristic colors [Fig. 6.8(b)].

Recently, sensitive ELISA sensing by gold nanoparticles has been reported using this approach [83]. However, the solution phase of nanoparticles can cause technical difficulties when the sensor is integrated in the on-chip microfluidic device. To address this challenge, a spatially arranged nanoparticle array as shown in Fig. 6.8(c) was considered. To realize this idea, the scattering and absorption cross sections of an individual particle must be optimized since the number of nanoparticles in 2D array is much smaller compared to that of nanoparticle solutions. Here, we employed the patch antennas to demonstrate efficient color representation of 2D optical antenna array by optimizing light coupling. A similar methodology has been reported to represent colors at the optical diffraction limit [84].

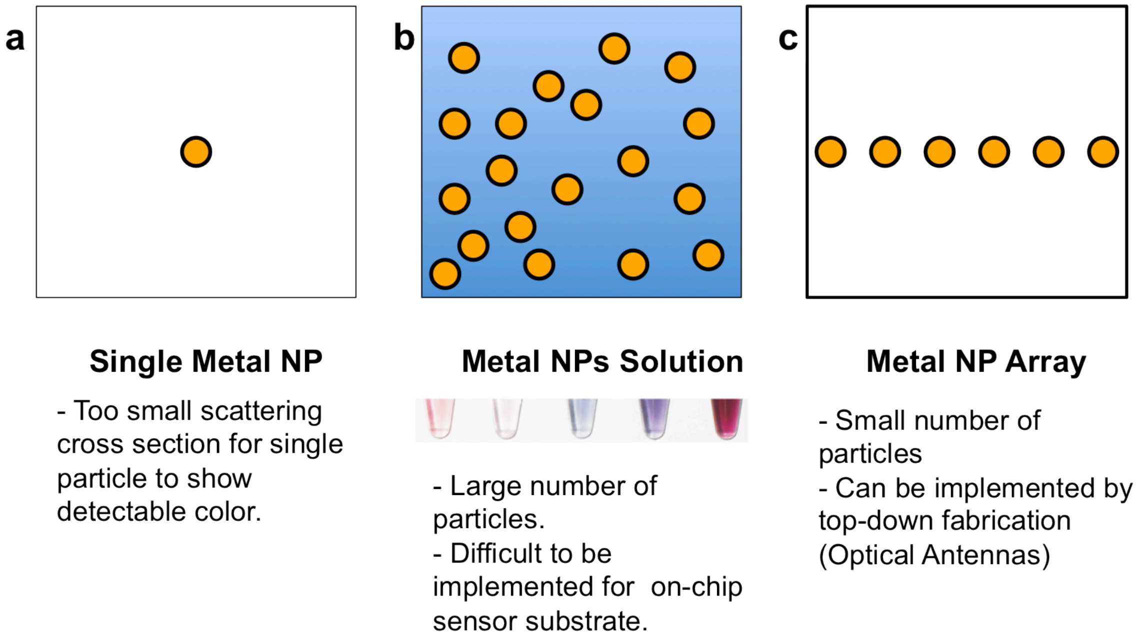

Figure 6.44 Schematic of metal nanoparticles. a, Single metal nanoparticle. **b,** Metal nanoparticles in solution. **c,** Metal nanoparticle array.

In the previous sections, we focused on the developed a patch antenna with high field enhancement by exploiting nanometric-scale gap. However, the extremely small gap spacing results in the poor coupling of light due the huge mismatch between radiation and absorption quality factors. In the next section, we optimized the coupling of light by tuning the spacer thickness for Q-matching condition, which is similar to the approach presented in Chapter 5.

6.5.2 Simulation of Patch Antenna for Optimized Light Coupling

For clear color representation, the light coupling of the optical antenna must be optimized. The patch antenna array on ground plane was used to achieve this goal. The gold ground plane increased the antenna cross section by improving the radiation directivity. Note that scattering and absorption cross sections of patch antenna array without the ground plane are too small to emit strong color [see the inset in Fig. 6.9(a)]. In addition, the coupling of the antenna was maximized by engineering the radiation of optical antennas, which can be achieved by tuning the thickness of the dielectric layer. In order to find the optimum thickness of the dielectric spacer layer, numerical simulations of the patch antenna arrays have been investigated. Figure 6.9(a) shows the simulated reflectance spectra with various thicknesses of dielectric spacer layers. The reflectance dip of the antenna array was maximized when the thickness of aluminum oxide spacer was around 55 nm, as shown in Fig. 6.9(a) and Fig. 6.9(b).

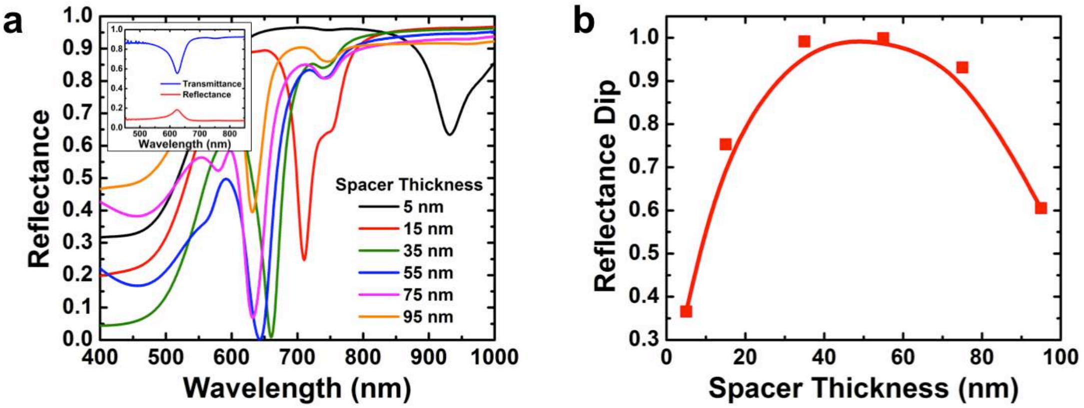

Figure 6.45 Schematic and reflectance simulation of patch antenna at visible frequencies. a, Simulated reflectance spectra from patch antenna arrays with various spacer thicknesses. **b,** Plot of the reflectance dip as a function of the spacer thickness. The inset in (**a**) shows the transmittance and reflectance of patch antenna array on dielectric substrate without ground plane for comparison. The reflectance dip is maximized when the spacer thickness is 55 nm.

6.5.3 Fabrication and Experimental Measurement

Optical patch antenna arrays were fabricated using the same fabrication process as described in Section 6.3. The only difference was the spacer thickness, which was chosen to be 55 nm as was done for the simulation for the optimized light coupling. Circular patch antennas of various sizes (36, 48, 60, 72, and 84 nm) and three different pitch distances (200, 300, and 400 nm) were fabricated to investigate the color representation of patch antenna arrays. The schematic of patch antenna arrays and the representative SEM image are shown in Fig. 6.10(a).

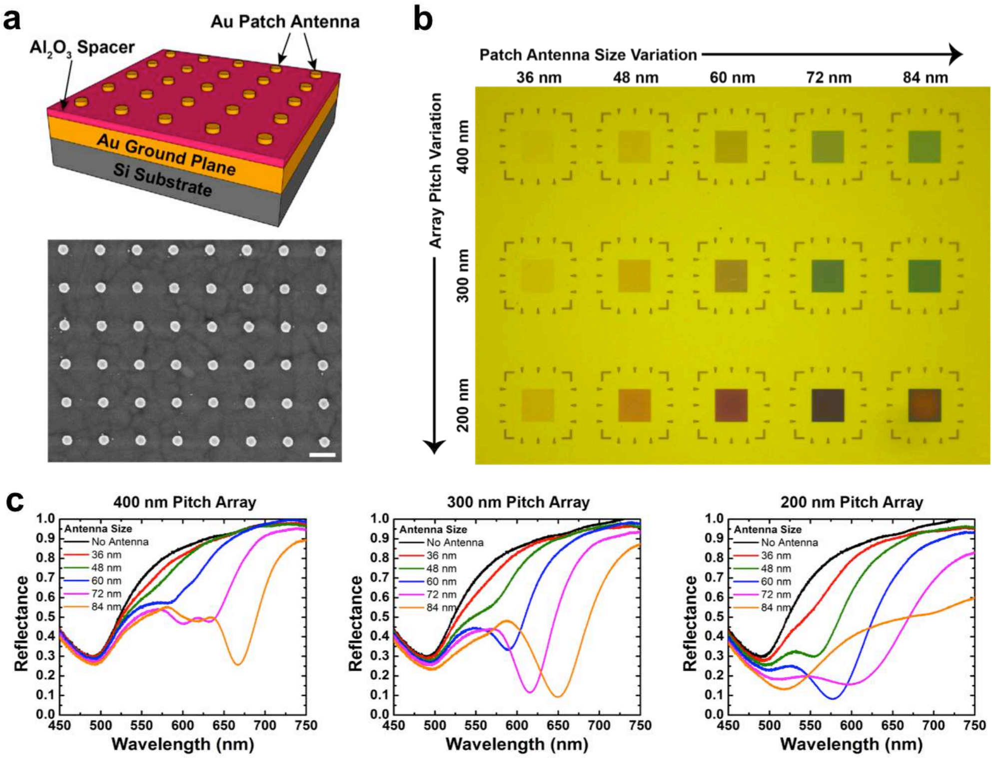

Figure 6.46 Optical patch antenna array for colorimetric sensing. a, Schematic picture of the gold patch antenna array and SEM picture of a fabricated antenna array. **b,** Optical image of fabricated antenna arrays with various antenna sizes and array pitches. **c**, Reflectance spectra measured from fabricated antenna arrays. The scale bar in the SEM image represents 200 nm.

Figure 6.10(b) shows the optical image of fabricated antenna arrays. Each antenna array has a field size of 30 μm × 30 μm. The antenna arrays of the same size patch antenna generally show similar colors, though the smaller pitch array has the stronger contrast. However, 200-nm pitch antenna arrays of 72- and 78-nm patch show different color trends from 300 and 400 nm pitch antenna arrays of the same size. This is probably because the inter-space for the large size antennas (72 and 78 nm) in the 200-nm pitch array is small enough to induce the interaction between individual antennas.

To study the spectral response, we measured the reflectance spectra from these antenna arrays. Figure 6.10(c) shows the measured spectra from the fabricated antenna arrays. Comparing the reflectance of same-sized antenna arrays but with different array pitches, the reflectance dip increases when the pitch dimensions decreases, whereas the antenna resonance does not significantly shift. However, the reflectance spectrum does not show a well-defined single resonance and exhibits broad dips when the antenna size becomes larger than 70 nm in a 200-nm array pitch. Therefore, the 300-nm array pitch is preferred for the colorimetric sensing application since it has a moderate strength of the color contrast and the expected resonance shift behavior with changes in the size of the antenna.

It has been recently reported that the resonance shift of metal nanoparticles by enzyme-guided crystal growth can be used as a plasmonic nanosensor with extremely high sensitivity [82]. A similar approach can be applied to the patch antenna design investigated here for the resonance shift by changing the antenna dimension [85]; this results in a color change of the antenna array. The simple shape and arrangement of the suggested patch antenna design raises the possibility of providing a large area fabrication using specialized nano-fabrication techniques such as nanoimprint lithography [86].

6.6 Summary

In this chapter, we discussed optical patch antennas to demonstrate that uniform and reproducible nanometer-scale gap spacing is critical for achieving efficient local field enhancement. The gap of a patch antenna is defined vertically by the thickness of the dielectric spacer layer. The dielectric spacer is deposited by atomic layer deposition, hence, the formation of sub-5nm gap is possible with the sub-nm accuracy in thickness control and with perfect uniformity. Strong SERS signals from BPE molecules have been measured from fabricated patch antenna arrays, with an enhancement factor of 1.5×10^7, which is about an order of magnitude improved than that measured from the dipole antenna array discussed in Chapter 5. The correlation between antenna resonance and SERS intensity was also investigated using patch antenna arrays, confirming that SERS signal can be maximized when the antenna resonance is positioned at the middle of excitation and emission wavelength, which agrees well with the previously reported result [87]. However, it should be noted that there exists a trade-off between mode volume and radiation efficiency when considering the patch antenna design. As the gap spacing is reduced to the nanometric scale, the radiation efficiency is dramatically decreased. This results in the huge mismatch between the radiation and absorption quality factors, and prevents improvement of local field enhancement even if the gap spacing is reduced even further.

CHAPTER 7

Optical Arch-Dipole Antenna

In Chapter 5 and 6, the dipole antenna and the patch antenna were introduced and demonstrated that both designs were capable of achieving efficient local field enhancement. The dipole antenna design offers a relatively simple way to engineer the radiation of the antenna by tuning the spacer thickness between the antenna and the ground plane. At the optimum spacer thickness, the amount of the antenna radiation is matched to the absorption, thus maximizing the local field enhancement of the antenna. However, field enhancement is critically dependent on the gap dimension of the antenna, and it is challenging to scale down the dipole antenna gap below 10 nm due to the technical limit of the fabrication resolution. The patch antenna design in Chapter 6 resolved this fabrication issue by defining the vertical gap with a thin spacer layer between the patch and the ground plane. However, as demonstrated, the radiation efficiency of the patch antenna is poor, because when the gap spacing is reduced to nanometer scale, it degrades the light coupling of the antenna.

In this chapter, we introduce a novel optical antenna design—the arch-dipole antenna—with 5-nm gap spacing fabricated using the CMOS process. In this process, the gap spacing of the arch-dipole antenna is determined by the thickness of a thin dielectric fin using deep-UV spacer lithography [88], [89]. Since the fin layer is deposited by atomic layer deposition (ALD), the thickness of the fin can be precisely controlled with sub-nm accuracy and good reproducibility. In this design, the optimum fin height is chosen to control the radiation of the arch-dipole antenna, which enables matched radiation and absorption quality factors for maximum field enhancement.

7.1 Arch-Dipole Antenna to Overcome Trade-off between Radiation Efficiency and Small Gap Spacing

In Chapter 5, the radiation characteristic of an optical dipole antenna was controlled by tuning the thickness of the dielectric spacer layer, and the field enhancement of the antenna was maximized using the optimum spacer thickness with matched quality factors (Q_{rad}=Q_{abs}). However, it is challenging to reduce the gap spacing of dipole antennas below 10 nm since optical antennas are typically fabricated by nanofabrication techniques such as e-beam lithography or focused ion beam (FIB) milling; these techniques have poor uniformity and reproducibility below 10 nm dimension. To address this fabrication issue, optical patch antennas, discussed in Chapter 6, were developed, which can be easily fabricated with uniform sub-5 nm gap. Since the dielectric spacer layer between the top nanopatch and the ground plane defines the antenna gap spacing, it can be easily reduced below 5 nm with sub-nm accuracy by atomic layer deposition (ALD). Unfortunately, although it is possible to reduce the gap of the patch antenna to nanometer scale, it results in poor radiation efficiency, which then results in the huge mismatch between Q_{rad} and Q_{abs}. Therefore, the field enhancement does not increase significantly despite the reduction in the gap spacing.

To overcome the trade-off between radiation efficiency versus the small gap spacing, a new antenna design "arch-dipole antenna" was developed, the primary focus of this paper. In the arch-dipole antenna, the two arms of a dipole antenna are connected by a tall narrow arch, as shown in Fig. 7.1. The antenna gap inside the arch can be defined by the thickness of a sacrificial dielectric layer using spacer lithography. The arch-dipole antenna design offers a robust method for uniform and reproducible fabrication of sub-5 nm gap spacing without sacrificing radiation efficiency.

The radiation efficiency of the arch-dipole antenna was controlled by the dimension of the arch height (gap height). By tuning the arch height dimension, the radiation was able to be matched to the absorption of the antenna. The numerical analysis will be discussed next.

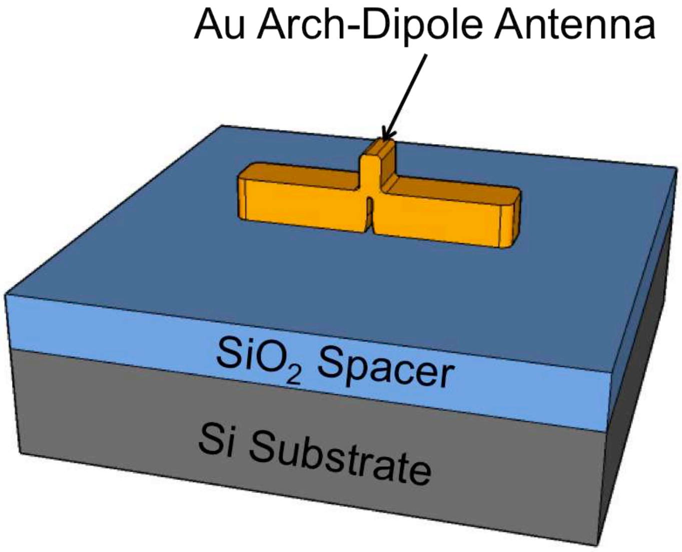

Figure 7.47 Schematic of optical arch-dipole antenna. The gap spacing of the arch-dipole antenna is defined by the thickness of a sacrificial dielectric layer.

7.2 Numerical Simulation of Arch-Dipole Antenna

To understand the characteristics of the arch-dipole antenna, the time domain simulations of a gold arch-dipole antenna array was investigated, with the following dimensions: 210 nm length, 50 nm width, 40 nm thickness, and 5 nm gap as shown in Fig. 7.2(a). A dipole antenna array with same length, width, thickness and gap dimensions was also simulated for comparison. The field enhancement plot shown in Fig. 7.2(b) shows that the arch-dipole antenna had two resonant modes dependent on the current direction in the arch, whereas a normal dipole antenna had a single fundamental mode. The field enhancements of the two arch-dipole antenna modes were higher than the normal dipole antenna with the same gap spacing since the *Q* matching condition was achieved for the arch-dipole antenna by tuning the arch height. Here, the higher frequency mode was selected (the arch current in the opposite direction relative to the antenna arm current) because the antenna dimensions were easier to fabricate (they were longer in length for the desired resonance). The field distribution of two modes is shown in Fig. 7.2(c). Note that the current distribution (represented by white arrows) around the arch is different in two modes.

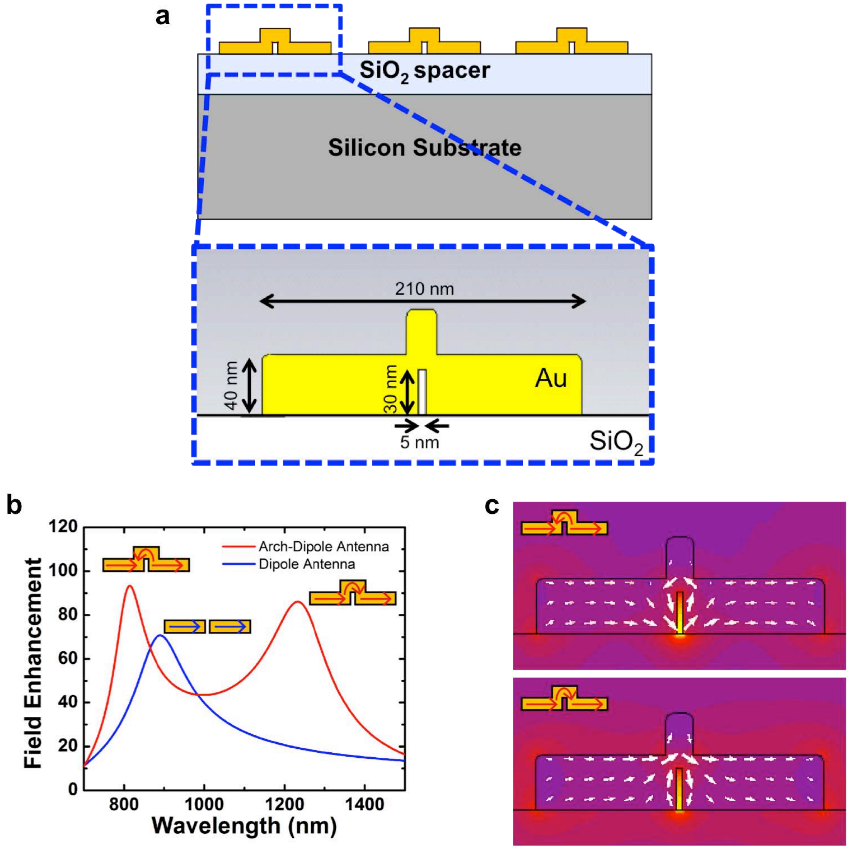

Figure 7.48 Numerical simulation of gold arch-dipole antenna array. a, Schematic of the simulated structure. 210 nm long, 50 nm wide, and 40 nm thick gold arch-dipole antennas with 5 nm gap and 30 nm arch height were simulated. Periodic boundary condition was used to calculate an antenna array with 600 nm pitch. **b,** Electric field enhancement of arch-dipole antenna (red curve). Standard dipole antenna with same gap and length was also simulated for comparison (blue curve). Arch-dipole antenna has two modes depending on the current direction in the arch. **c,** Electric field magnitude profile of simulated arch-dipole antennas. White arrows in antennas represent the current distribution.

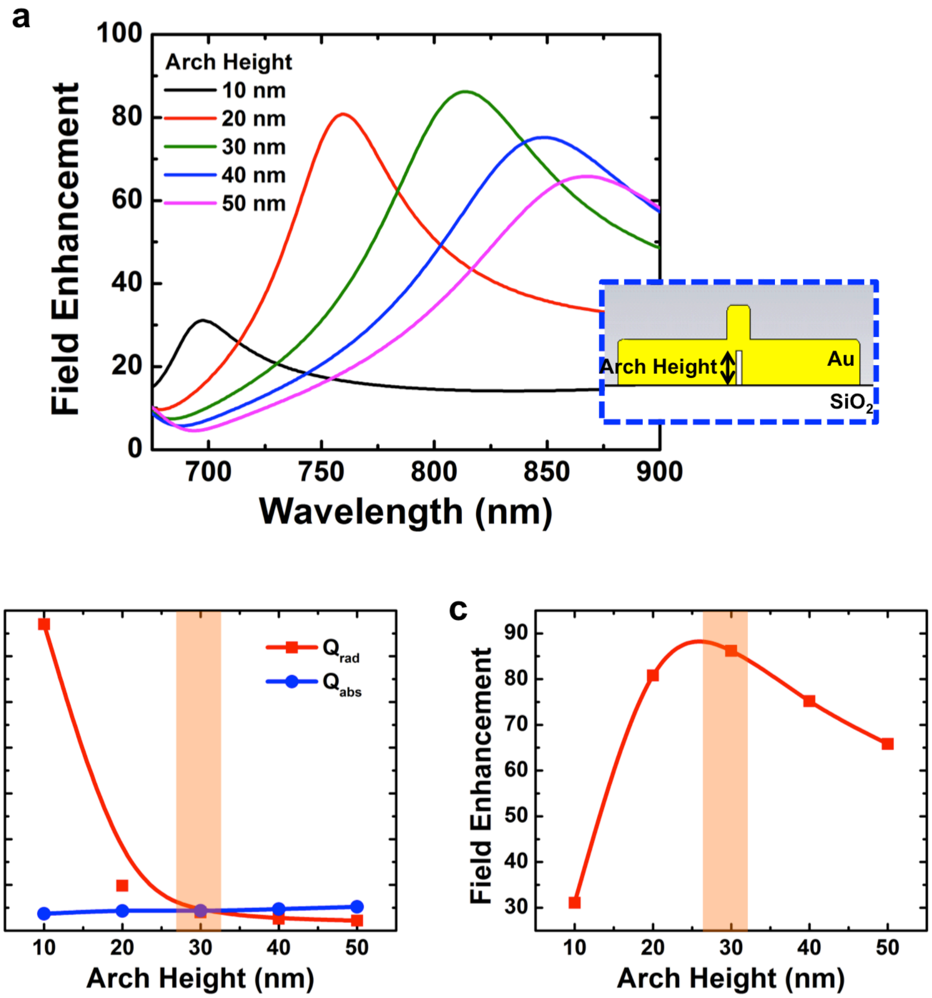

Figure 7.49 Numerical simulation of arch-dipole antenna array with arch height variations. a, Field enhancement spectra of arch-dipole antenna arrays with arch height variations. **b,** Radiation and absorption quality factors as a function of arch height. **c,** Electric field enhancement as a function of arch height. profile of simulated arch-dipole antennas. White arrows in antennas represent the current

distribution. The field enhancement has a maximum peak at the optimum arch height (30 nm) for Q-matching condition (Q_{rad}=Q_{abs}).

The arch-dipole antennas with various arch heights were simulated to estimate the effect of the arch height dimension for the antenna characteristics. Figure 7.3(a) shows the field enhancement of arch-dipole antenna with various arch heights. Radiation and absorption quality factors (Q_{rad} and Q_{abs}) were also calculated from the simulations. As shown in Fig. 7.3(b), the radiation of the antenna improved as the arch height increased. As a result, the field enhancement is maximized when Q_{rad} is matched to Q_{abs} at the arch height of 30 nm [Fig. 7.3 (c)].

7.3 Fabrication of Arch-Dipole Antenna

A deep-UV spacer lithography was used to define the gap spacing and the arch height of the antenna. The fabrication process flow of arch-dipole antenna array is illustrated in Fig. 7.4.

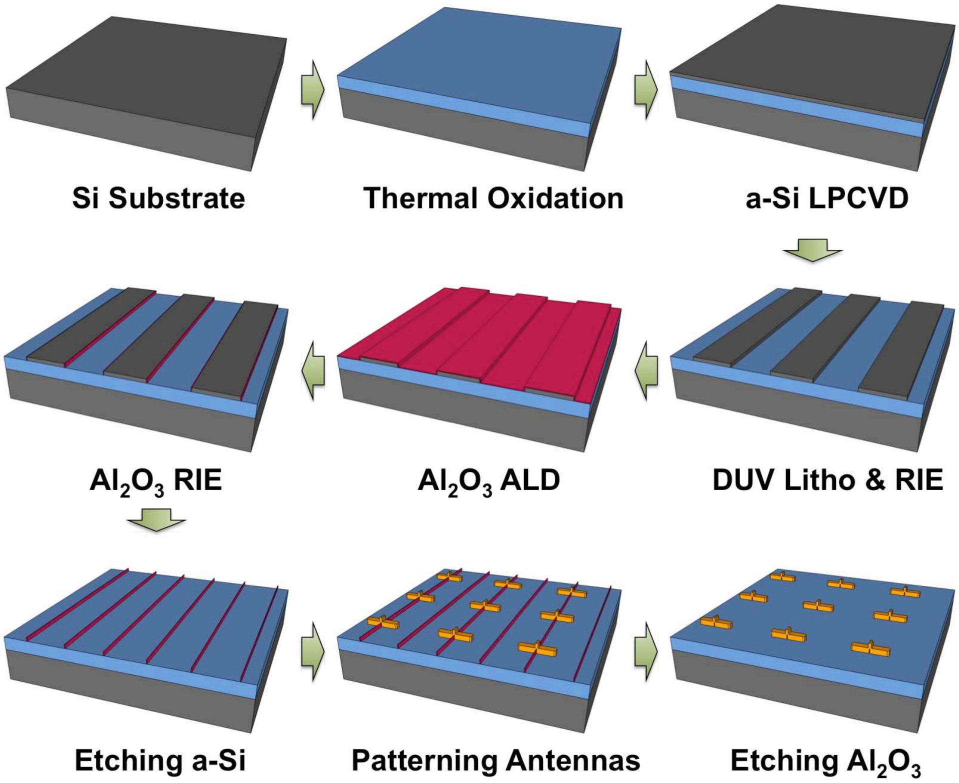

Figure 7.50 Fabrication process flow for arch-dipole antenna array.

Initially, a 100 nm layer of wet thermal oxide was grown at 1000 °C on top of a silicon wafer. A 30-nm-thick amorphous silicon layer was deposited by the LPCVD as a sacrificial layer. The thickness of this a-Si layer determines the arch height of the antenna. For deep UV (DUV) optical lithography, a 390 nm thick Rohm Hass positive UV210-0.6 (DUV resist) layer was spin-coated on top of the wafer, followed by DUV exposure of 600 nm period grating ridge patterns (300 nm line width) using ASML DUV 5500/300 stepper. Then, the a-Si layer is etched by a Lam Research 9400 TCP (Transformer Coupled Plasma) etcher to the following specifications: 50 sccm Cl_2, 150 sccm HBr, 15 mTorr, 300 W TCP RF power, and 120 W Bias RF power for the main etch step, and 100 sccm HBr, 1 sccm O_2, 100 sccm He, 80 mTorr, 200 W TCP RF power, and 150 W Bias RF power for the over etch step. After stripping the photoresist by oxygen plasma, the wafer was cleaned in piranha and RCA1 to remove the etching by-product. These anisotropic etching step and post-etch cleaning step are very important because the vertical and clean sidewall profile of a-Si grating ridge is critical for the free-standing nano-fin process. The comparison of nano-fins fabricated with and without the post-etch cleaning step is shown in Fig. 7.5.

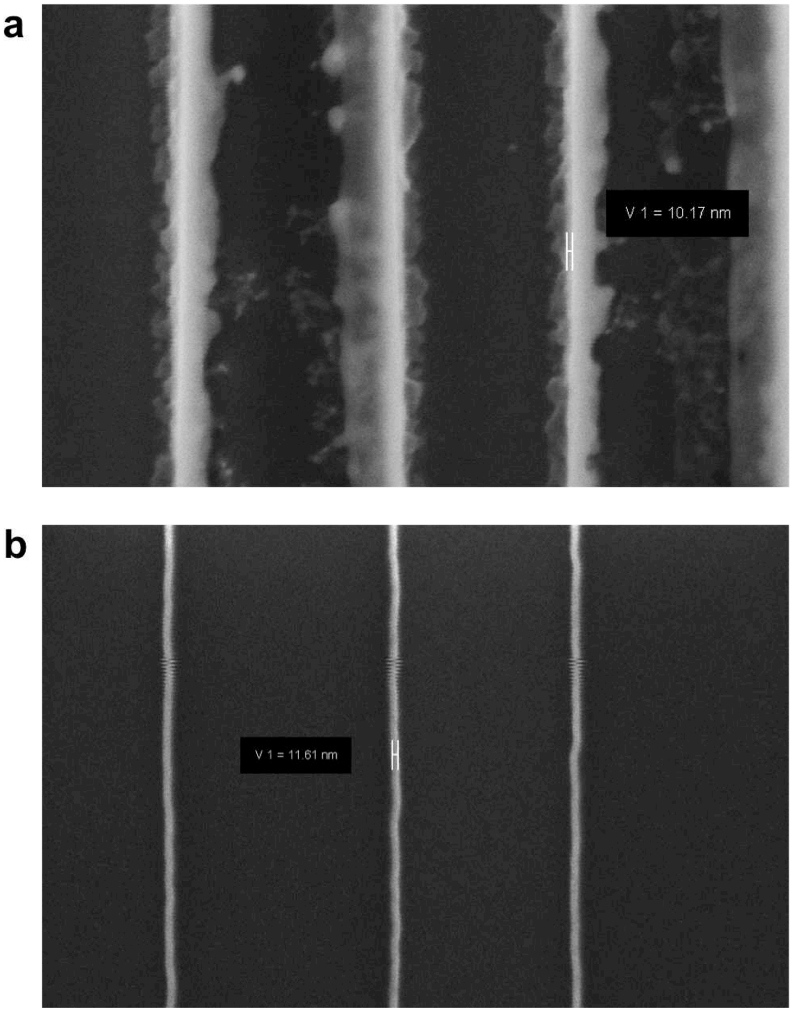

Figure 7.51 SEM images of fabricated nano-fins with and without the post-etch cleaning step. a, Nano-fin fabricated without the post-etch cleaning step. **b,** Nano-fin fabricated with the post-etch cleaning step.

After cleaning, a 5 nm thick aluminum oxide layer was deposited by a Picosun Sunale R150 atomic layer deposition (ALD) tool. Since the atomic layer deposition guarantees conformal and uniform dielectric layer with sub-nm thickness control, sub-10 nm Al_2O_3 layers are easily reproduced using this technique. Then, the Al_2O_3 layer is etched away from the top using a Lam Research 9600 TCP etcher with the condition of 45 sccm Cl_2, 60 sccm BCl_3, 8 mTorr, 700 W TCP RF power, and 100 W Bias RF power. This anisotropic etching removes the horizontal parts of Al_2O_3 layer and leaves only the vertical parts on the sidewall of a-Si sacrificial ridges. Subsequent selective etching of a-Si sacrificial ridges by xenon difluoride (XeF_2) resulted in 5 nm wide and 30 nm tall nano-fins standing on top of the wafer.

A 70 nm thick layer of PMMA was spin-coated on top of the wafer, and the array of rectangular antenna patterns (~ 200 nm length and ~ 50 nm width) was aligned on nano-fins using Crestec CABL-9510CC high-resolution electron beam lithography system. After developing, a 40 nm thick gold layer was deposited by e-beam evaporator, followed by standard lift-off process using acetone. This antenna-patterning step is replaceable with photolithography for wafer-scale fabrication since the dimensions of antenna rectangles (150 ~ 300nm length and 50 ~ 100 nm width) are feasible size by lithography using current CMOS technology.

Finally, Al_2O3 fins were etched away to open air-gaps in the arch-dipole antennas. For the selective etching of Al_2O_3, the sample was immersed in 67 °C phosphoric acid for five minutes.

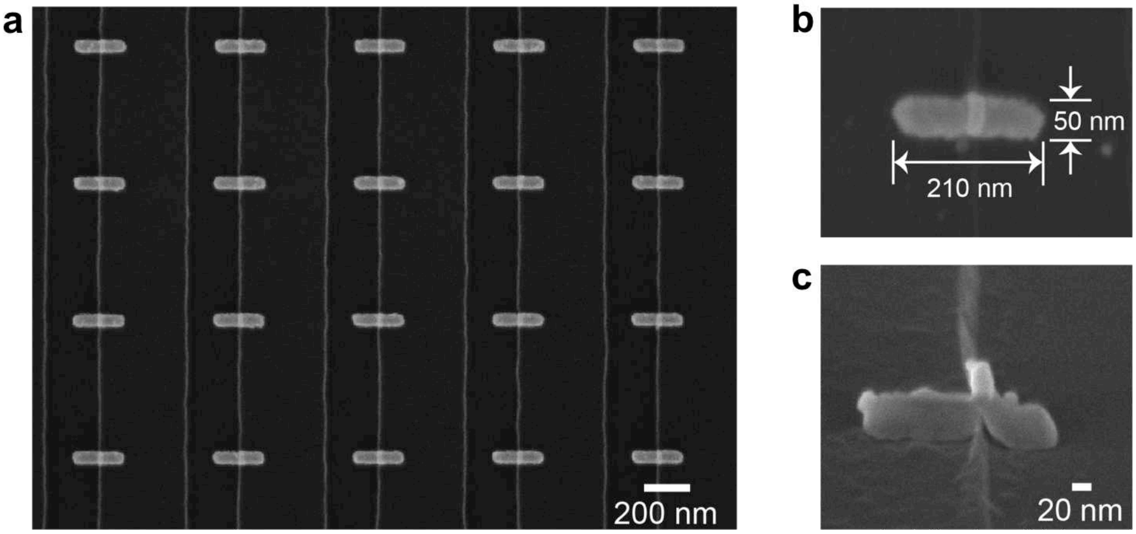

Figure 7.52 SEM images of fabricated arch-dipole antenna arrays. a, Fabricated arch-dipole antenna array before etching Al_2O_3 fins. **b,c,** SEM images of an arch-dipole antennas after etching Al_2O_3 fins with top view (**b**) and perspective view (**c**).

7.4 Experimental Measurement

7.4.1 Reflectance Measurement

The antenna resonances were characterized by reflectance measurements. Figure 7.7(a) shows the reflectance spectrum from the arch-dipole antenna array with 210 nm length, 50 nm width, 40 nm thickness, and 5 nm gap, which are comparable dimensions to the simulated antenna array. For the reflectance measurement, white light from a halogen lamp was focused by 50x objective lens and illuminated on an arch-dipole antenna array. The reflected light was collected through the same objective lens and then sent to the spectrometer. Two kinds of CCD cameras were used to obtain an improved spectral response for the wide wavelength range. A Si CCD camera was used to measure reflectance for the wavelength range from 500 nm to 950 nm, and an InGaAs CCD camera was used for the range from 950 nm to 1500 nm. The reflectance measurement clearly shows two main antenna modes of the arch-dipole antenna around 800 nm and 1300 nm, as predicted from the simulation [Fig. 7.2(b)].

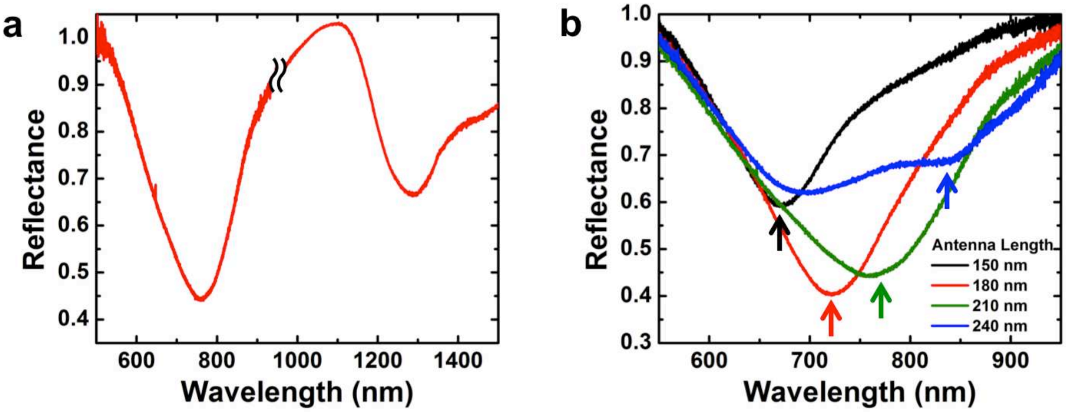

Figure 7.53 Reflectance measured from arch-dipole antenna arrays. a, Reflectance measured from 210 nm length arch-dipole antenna array. Si CCD camera was used for the wavelength range from 500 to 950 nm, and InGaAs CCD camera for the range from 950 to 1500 nm. **b,** Reflectance spectra for the higher frequency mode (using Si CCD camera) from arch-dipole antenna arrays with

various lengths. The resonance dip exhibits a red-shift with increasing antenna length.

For the resonance tuning, antenna arrays with various antenna lengths (150, 180, 210, and 240 nm) were fabricated, and the reflectance spectra were measured to characterize the resonance shift of the higher frequency mode. The measured reflectance spectra are plotted in Fig. 7.7(b). A red-shift of the antenna resonance can be clearly seen with increasing antenna length.

7.4.2 SERS Measurement

For SERS measurements, trans-1,2-bis (4-pyridyl) ethylene (BPE) was again used as the target molecule. As discussed in the previous chapters, the samples were subjected to a similar procedures, with the arch-dipole antennas coated in BPE molecules. Figure 7.8(a) shows the measured SERS spectra from antenna arrays with various antenna lengths. The antenna arrays with short lengths (150 nm and 180 nm) exhibited weak SERS signals since the resonance wavelengths were far from the excitation laser wavelength. The measured SERS signals increased as the resonance of the antenna arrays moved close to the excitation wavelength and Stokes shifted wavelength with longer antenna lengths (210 nm and 240 nm). The best SERS enhancement of 1200 cm^{-1} Raman peak was measured to be 1.8×10^{8}, which is two orders of magnitude better than the dipole antenna discussed in Chapter 5.

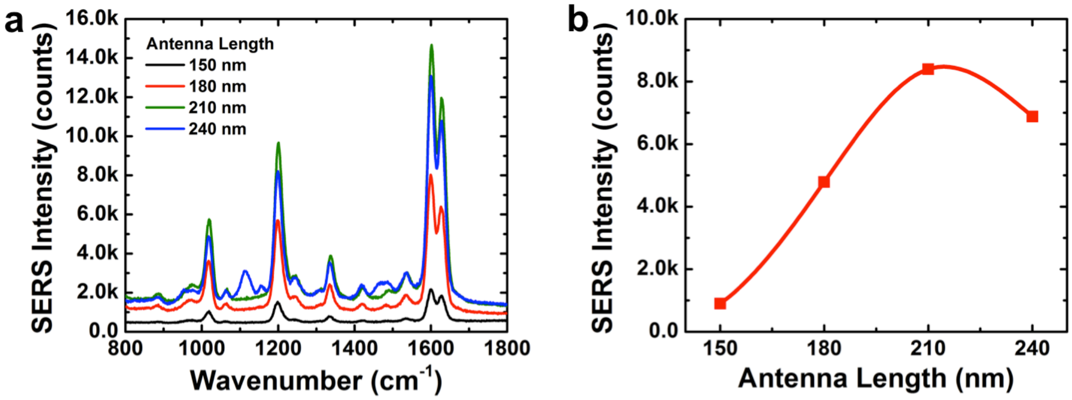

Figure 7.54 SERS spectra measured from arch-dipole antenna arrays. a, BPE SERS spectra measured from arch-dipole antenna arrays with various antenna lengths. **b,** 1200 cm^{-1} peak SERS intensity plot as a function of antenna length. The strongest SERS signals were observed from antenna arrays (210 nm and 240 nm

long antenna arrays) of which resonances were close to excitation laser wavelength and Stokes shifted wavelength.

The effect of the excitation polarization was also investigated with various angles of polarized excitation, as shown in Fig. 7.9. The strongest SERS signal was observed when the polarization of the excitation was parallel to the antenna arms; the signal deceased as the excitation polarization became more perpendicular to the antenna arm axis. The strong dependence on the antenna length and the excitation polarization confirm that the SERS signals resulted from the optical antennas.

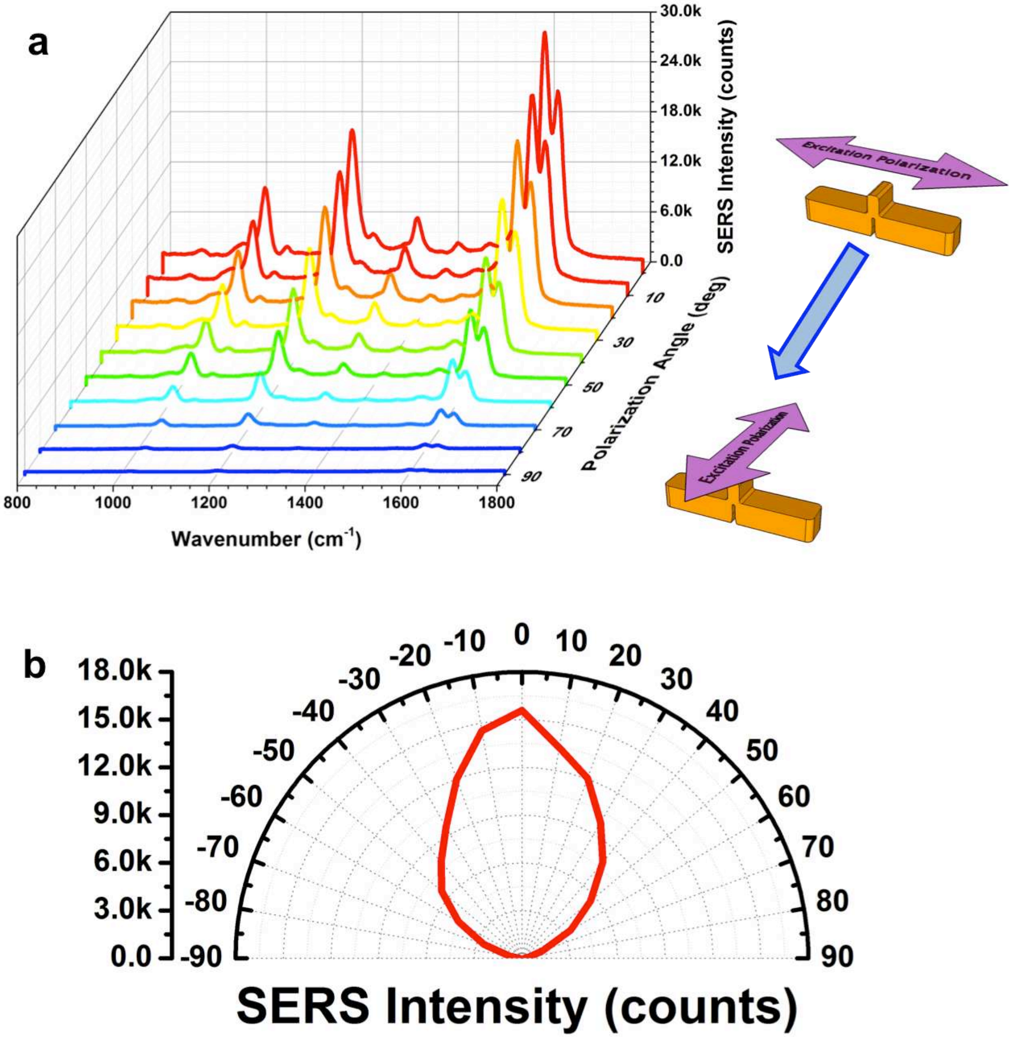

Figure 7.55 SERS comparison with different excitation polarization. a, BPE SERS spectra measured with various excitation polarizations. **b,** 1200 cm^{-1} peak SERS intensity plot as a function of excitation polarization angle respect to the antenna arms.

7.4.3 Effect of Arch Position on Arch-Dipole Antenna

The effect of the arch position on the arch-dipole antenna is investigated next. Position variations of the arch can be demonstrated by intentional alignment offset during the antenna patterning step. Figure 7.10(a) shows three different arch-dipole antenna arrays with identical dimensions (210 nm length, 50 nm width, and 40 nm thickness) except for the arch position. These arrays have different positions on the arches, which are located at the center, 40 nm off from center, and 80 nm off from the center of the antenna. Reflectance measurement was used to characterize the resonances of the arch-dipole antenna arrays. The primary focus was on the higher frequency mode between the two main modes of arch-dipole antenna since the higher mode has a resonance close to the Raman excitation and emission wavelength. The antenna array with the centered arch has a single resonance with a big reflectance dip. However, the resonance splits into two separate modes as the arch position starts to diverge from the center due to the asymmetric antenna arm length [Fig. 7.10(b)]. The strongest SERS signal was observed from the arch-dipole antenna array with the centered arch because of the tuned resonance for exaction of the laser wavelength. The SERS signals from antenna arrays with the off-centered arch degraded as the antenna resonances moved away from the excitation and emission of wavelengths, as shown in Fig. 7.10(c).

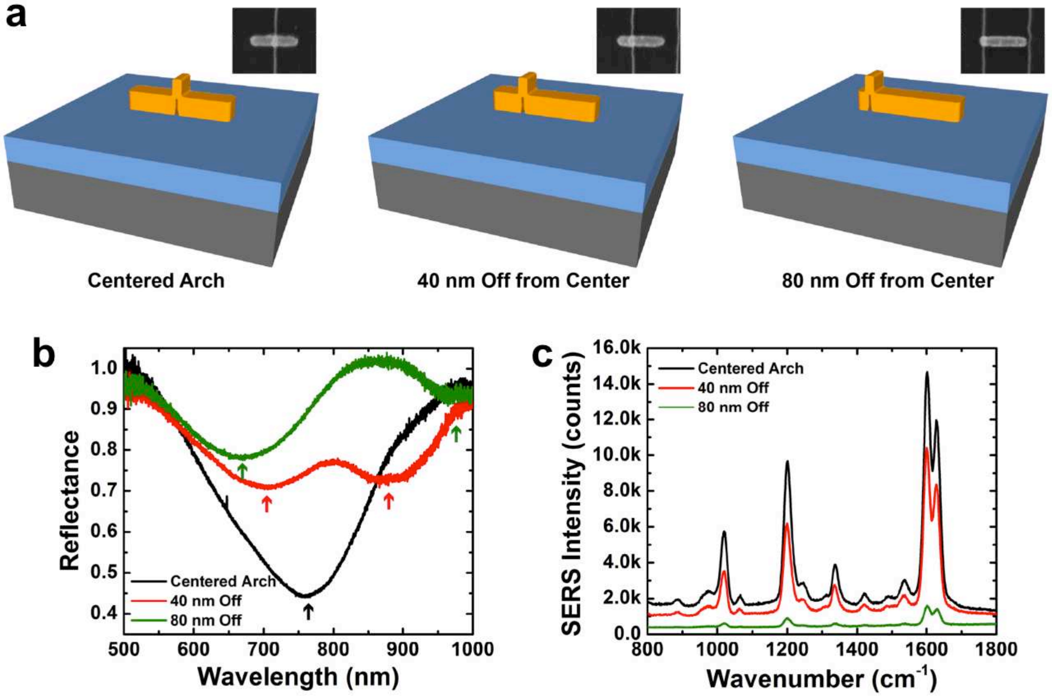

Figure 7.56 Effect of arch position variations on arch-dipole antenna. a, Schematics of arch-dipole antennas with arch position variations: centered arch, arch of 40 nm off from center, and arch of 80 nm off from center. Insets show SEM

images of corresponding arch-dipole antennas. **b,** Reflectance measurements of arch-dipole antenna arrays with arch position variations. **c,** SERS measurements of arch-dipole antenna arrays with arch position variations.

7.5 Summary

This chapter introduced a new antenna design—the arch-dipole antenna—which can be readily fabricated with a uniform gap spacing below 5 nm. Since the critical dimensions of arch-dipole antennas can be precisely controlled with sub-nm accuracy, the arch-dipole antenna can be physically realized with a small gap (sub-5 nm) and Q matching condition. The dipole antenna design (see Chapter 5) achieves the Q matching condition by optimizing the spacer thickness between the antenna array and the ground plane; however, reducing the gap spacing below 10 nm is challenging using typical nanofabrication techniques such as e-beam lithography and focused ion beam milling. In contrast, the patch antenna can be easily implemented with extremely small gaps; however, the poor radiation efficiency and the mismatched Q factors degrade the antenna performance. The arch-dipole antenna offers an efficient way to achieve small mode volume and Q matching condition without trade-off in performance. As a result, the SERS enhancement factor from the arch-dipole antenna is up to two orders of magnitude stronger compared to the other two antenna designs. The gap spacing is the most critical dimension for the enhancement and can be defined by deep UV spacer lithography; therefore, wafer-scale SERS substrate with sub-5 nm gap optical antennas can be mass-produced in current CMOS foundries.

CHAPTER 8

Conclusion

This dissertation first discussed the basic theories underlying radio frequency antenna and how these theories might be applied to optical antenna. This necessitated a review the material property of metal at optical frequencies and why metal can confine the electromagnetic fields on their surface. Then, we saw how metallic nanoparticles interact with a light by scattering. Next we found that the interference between incident wave fields and re-radiated (scattered) wave fields results in the light-matter interaction. Then we devised and fabricated three antenna and subjected them to experimentation to evaluate their efficient local field enhancement.

However, the interaction between the electromagnetic wave and a conductor is not only applied at optical frequencies. Actually, people have been using devices to transduce propagating electromagnetic waves into the electric signals or vice versa at radio frequencies for broadcasting or communication. These devices are called antennas. The theory for RF antennas is of long standing and continues to be improved upon. The success of the theory has made it possible to take advantage of well-established antenna theory and extend this theory to optical antennas. Although there remain serious difference in terms of materials properties and the change of operating frequencies, but there are also some similarities that we should exploit. With this in mind, a review of the fundamentals of the theories underpinning antenna has revealed that several of these basic concepts can also be applied to optical antennas, such as radiation pattern, directivity, antenna effective aperture, antenna circuit model, and so on.

Next, we explored the distinctive features of optical antennas in receiving and transmitting operations. In receiving mode, an optical antenna captures a propagating electromagnetic wave and focuses the energy with strong local fields into a sub-wavelength region beyond the diffraction limit of light. In transmitting mode, an optical antenna increases the local density of states of photons and enhances the vacuum field. As a result, the spontaneous emission rate of an emitter placed at the high field region of the antenna is significantly enhanced. Therefore, local field enhancement of an optical antenna is an important design parameter for the optimum performance for both receiving and transmitting. The comprehensive design strategy of efficient optical antennas required deriving theoretically the field enhancement in terms of two frameworks: the coupled-mode theory and the antenna circuit model; these two approaches converged to an identical result. Successful derivation of the equation for field enhancement demonstrated that the marching of radiation and absorption quality factors and the small gap spacing were critical parameters

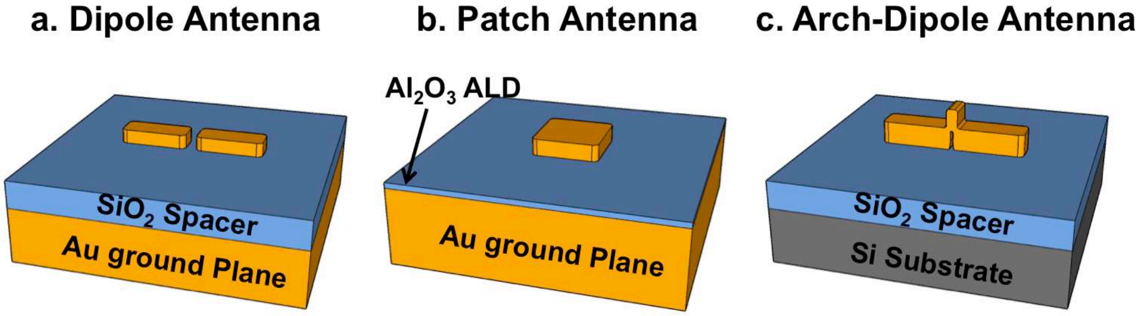

Figure 8.57 Schematics of optical antenna designs. a, Dipole antenna on ground plane for matched quality factors. **b,** Patch antenna for sub-5 nm gap spacing. **c,** Arch-dipole antenna for matched quality factors and 5 nm gap spacing.

To demonstrate experimentally the efficient field enhancement of optical antennas, three different designs of optical antennas were fabricated and are shown in Fig. 8.1. For the experimental verification of field enhancement, SERS experiments from these antenna designs were compared after being subjected to identical conditions, such as the target molecule, the coating method for molecules, the measurement set up, and the enhancement calculation. The dipole antenna design can achieve the Q matching condition by optimizing the spacer thickness between the antenna array and the ground plane; however, reducing the gap spacing below 10 nm is challenging when using typical nanofabrication techniques such as e-beam lithography and focused ion beam milling. In contrast, the patch antenna can be easily implemented with extremely small gaps; however, the poor radiation efficiency and the mismatched Q factors degrade the antenna performance. The arch-dipole antenna offers an efficient way to achieve small gap spacing and Q matching condition without any trade-offs in performance. Since the critical dimensions of arch-dipole antennas can be precisely controlled with sub-nm accuracy, fabrication of the arch-dipole antenna is possible, with both a small gap (sub-5 nm) and Q matching condition. As a result, the SERS enhancement factor from the arch-dipole antenna is two orders of magnitude stronger compared to the other two antenna designs. Since the gap spacing is the most critical dimension for the enhancement, it can be defined by deep UV spacer lithography, and wafer-scale SERS substrate with sub-5 nm gap optical antennas can be mass-produced in current CMOS foundries.

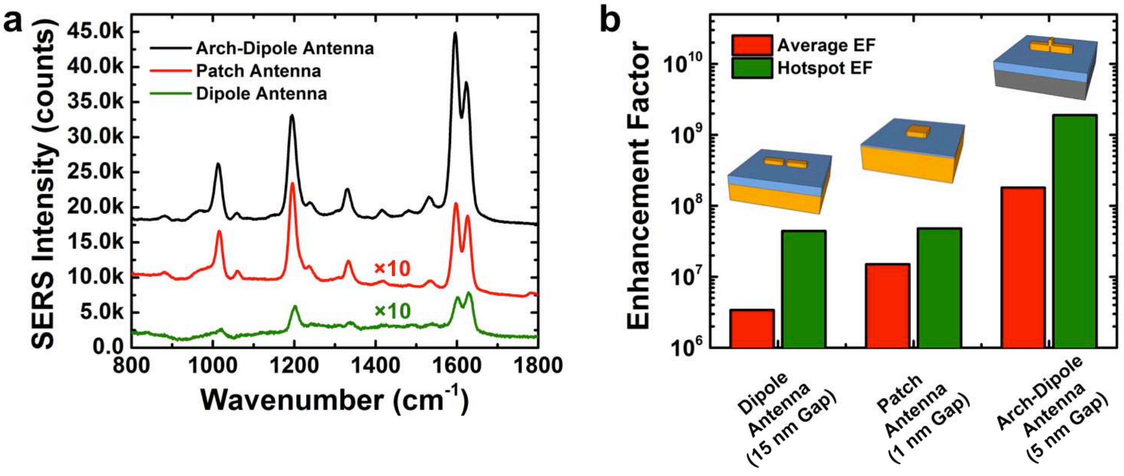

Figure 8.58 Comparison of measured SERS signals and calculated enhancement factors from dipole antenna, patch antenna, and arch-dipole antenna. a, SERS signals measured from different optical antenna designs. SERS spectra from dipole antenna array and patch antenna array were multiplied by 10 to make it more visible. **b,** Calculated SERS enhancement factors. Average enhancement factors were calculated assuming monolayer coating of BPE molecules on entire antenna surface. Hotspot enhancement factors were calculated from molecules coated on the sidewalls of antenna gap.

The last few years has seen the publication of many articles on the subject of optical antenna. Although these studies have achieved significant gains in broadening the understanding of optical antennas and the range of possible applications, designing efficient optical antennas with extremely small gap spacings and large area fabrication capabilities has remained a challenge, thereby limiting their practical application. The research presented herein has successfully outlined a strategy that conquers the previous issues that limited the widespread application of optical antenna. Although issues still remain to be resolved, such as impedance mismatching between the antenna and the target analyte or the quantum emitter source (atom or molecule), we are convinced that these issues will be solved in the near term as the field continues to attract bright researchers, and the expectation that new developments in this field are eminent is a realistic expectation.

REFERENCES

[1] E. H. Synge, “A suggested method for extending microscopic resolution into the ultra-microscopic region.,” *Philos. Mag.*, vol. 6, no. 35, pp. 356–362, Aug. 1928.

[2] J. Wessel, “Surface-enhanced optical microscopy,” *J. Opt. Soc. Am. B*, vol. 2, no. 9, pp. 1538–1541, Sep. 1985.

[3] U. C. Fischer and D. W. Pohl, “Observation of Single-Particle Plasmons by Near-Field Optical Microscopy,” *Phys. Rev. Lett.*, vol. 62, no. 4, pp. 458–461, Jan. 1989.

[4] T. Kalkbrenner, M. Ramstein, J. Mlynek, and V. Sandoghdar, “A single gold particle as a probe for apertureless scanning near-field optical microscopy,” *Journal of Microscopy*, vol. 202, no. 1, pp. 72–76, 2001.

[5] L. Novotny and S. J. Stranick, “Near-Field Optical Microscopy and Spectroscopy with Pointed Probes*,” *Annual Review of Physical Chemistry*, vol. 57, no. 1, pp. 303–331, 2006.

[6] L. O. Hocker, D. R. Sokoloff, V. Daneu, A. Szoke, and A. Javan, “Frequency Mixing in the Infrared and Far-Infrared using a Metal-To-Metal Point Contact Diode,” *Applied Physics Letters*, vol. 12, no. 12, pp. 401–402, Jun. 1968.

[7] B. Twu and S. E. Schwarz, “Properties of infrared cat-whisker antennas near 10.6 μ,” *Applied Physics Letters*, vol. 26, no. 12, pp. 672–675, Jun. 1975.

[8] T.-L. Hwang and S. E. Schwarz, “An antenna-coupled photovoltaic detector,” *Applied Physics Letters*, vol. 31, no. 2, pp. 101–104, Jul. 1977.

[9] S. E. Schwarz and B. T. Ulrich, “Antenna-coupled infrared detectors,” *Journal of Applied Physics*, vol. 48, no. 5, pp. 1870–1873, May 1977.

[10] S. Wang, “Antenna properties and operation of metal-barrier-metal devices in the infrared and visible regions,” *Applied Physics Letters*, vol. 28, no. 6, pp. 303–305, Mar. 1976.

[11] P. Mühlschlegel, H.-J. Eisler, O. J. F. Martin, B. Hecht, and D. W. Pohl, “Resonant Optical Antennas,” *Science*, vol. 308, no. 5728, pp. 1607–1609, Jun. 2005.

[12] L. Tang, S. E. Kocabas, S. Latif, A. K. Okyay, D.-S. Ly-Gagnon, K. C. Saraswat, and D. A. B. Miller, “Nanometre-scale germanium photodetector enhanced by a near-infrared dipole antenna,” *Nat Photon*, vol. 2, no. 4, pp. 226–229, Apr. 2008.

[13] P. Ghenuche, S. Cherukulappurath, T. H. Taminiau, N. F. van Hulst, and R. Quidant, “Spectroscopic Mode Mapping of Resonant Plasmon Nanoantennas,” *Phys. Rev. Lett.*, vol. 101, no. 11, p. 116805, Sep. 2008.

[14] M. Schnell, A. García-Etxarri, A. J. Huber, K. Crozier, J. Aizpurua, and R. Hillenbrand, “Controlling the near-field oscillations of loaded plasmonic nanoantennas,” *Nature Photonics*, vol. 3, no. 5, pp. 287–291, 2009.

[15] T. H. Taminiau, R. J. Moerland, F. B. Segerink, L. Kuipers, and N. F. van Hulst, “λ/4 Resonance of an Optical Monopole Antenna Probed by Single Molecule Fluorescence,” *Nano Lett.*, vol. 7, no. 1, pp. 28–33, Jan. 2007.

[16] T. H. Taminiau, F. D. Stefani, F. B. Segerink, and N. F. van Hulst, "Optical antennas direct single-molecule emission," *Nature Photonics*, vol. 2, no. 4, pp. 234–237, 2008.

[17] R. Esteban, T. V. Teperik, and J. J. Greffet, "Optical Patch Antennas for Single Photon Emission Using Surface Plasmon Resonances," *Phys. Rev. Lett.*, vol. 104, no. 2, p. 026802, Jan. 2010.

[18] J. Li, A. Salandrino, and N. Engheta, "Shaping light beams in the nanometer scale: A Yagi-Uda nanoantenna in the optical domain," *Phys. Rev. B*, vol. 76, no. 24, p. 245403, Dec. 2007.

[19] A. G. Curto, G. Volpe, T. H. Taminiau, M. P. Kreuzer, R. Quidant, and N. F. van Hulst, "Unidirectional Emission of a Quantum Dot Coupled to a Nanoantenna," *Science*, vol. 329, no. 5994, pp. 930–933, Aug. 2010.

[20] T. Kosako, Y. Kadoya, and H. F. Hofmann, "Directional control of light by a nano-optical Yagi–Uda antenna," *Nature Photonics*, vol. 4, no. 5, pp. 312–315, 2010.

[21] L. Cao, J.-S. Park, P. Fan, B. Clemens, and M. L. Brongersma, "Resonant Germanium Nanoantenna Photodetectors," *Nano Lett.*, vol. 10, no. 4, pp. 1229–1233, Apr. 2010.

[22] E. Cubukcu, E. A. Kort, K. B. Crozier, and F. Capasso, "Plasmonic laser antenna," *Applied Physics Letters*, vol. 89, no. 9, pp. 093120 –093120–3, Aug. 2006.

[23] M. Eggleston, A. Lakhani, L. Zhang, E. Yablonovitch, and M. C. Wu, "Optical antenna based nanoLED," in *2011 IEEE Photonics Conference (PHO)*, 2011, pp. 177 –178.

[24] K. J. Russell, T.-L. Liu, S. Cui, and E. L. Hu, "Large spontaneous emission enhancement in plasmonic nanocavities," *Nature Photonics*, vol. 6, no. 7, pp. 459–462, 2012.

[25] M. P. Busson, B. Rolly, B. Stout, N. Bonod, and S. Bidault, "Accelerated single photon emission from dye molecule-driven nanoantennas assembled on DNA," *Nature Communications*, vol. 3, p. 962, Jul. 2012.

[26] W. A. Challener, C. Peng, A. V. Itagi, D. Karns, W. Peng, Y. Peng, X. Yang, X. Zhu, N. J. Gokemeijer, Y.-T. Hsia, G. Ju, R. E. Rottmayer, M. A. Seigler, and E. C. Gage, "Heat-assisted magnetic recording by a near-field transducer with efficient optical energy transfer," *Nat Photon*, vol. 3, no. 4, pp. 220–224, Apr. 2009.

[27] E. J. Sánchez, L. Novotny, and X. S. Xie, "Near-Field Fluorescence Microscopy Based on Two-Photon Excitation with Metal Tips," *Phys. Rev. Lett.*, vol. 82, no. 20, pp. 4014–4017, May 1999.

[28] H. G. Frey, S. Witt, K. Felderer, and R. Guckenberger, "High-Resolution Imaging of Single Fluorescent Molecules with the Optical Near-Field of a Metal Tip," *Phys. Rev. Lett.*, vol. 93, no. 20, p. 200801, Nov. 2004.

[29] J. M. Gerton, L. A. Wade, G. A. Lessard, Z. Ma, and S. R. Quake, "Tip-Enhanced Fluorescence Microscopy at 10 Nanometer Resolution," *Phys. Rev. Lett.*, vol. 93, no. 18, p. 180801, Oct. 2004.

[30] J. N. Anker, W. P. Hall, O. Lyandres, N. C. Shah, J. Zhao, and R. P. V. Duyne, "Biosensing with plasmonic nanosensors," *Nature Materials*, vol. 7, no. 6, pp. 442–453, 2008.

[31] N. Liu, M. L. Tang, M. Hentschel, H. Giessen, and A. P. Alivisatos, "Nanoantenna-enhanced gas sensing in a single tailored nanofocus," *Nature Materials*, vol. 10, no. 8, pp. 631–636, 2011.

[32] D. P. Fromm, A. Sundaramurthy, A. Kinkhabwala, P. J. Schuck, G. S. Kino, and W. E. Moerner, "Exploring the chemical enhancement for surface-enhanced Raman scattering with Au bowtie nanoantennas," *The Journal of Chemical Physics*, vol. 124, no. 6, pp. 061101–061101–4, Feb. 2006.

[33] P. B. Johnson and R. W. Christy, "Optical Constants of the Noble Metals," *Phys. Rev. B*, vol. 6, no. 12, pp. 4370–4379, Dec. 1972.

[34] W. L. Barnes, A. Dereux, and T. W. Ebbesen, "Surface plasmon subwavelength optics," *Nature*, vol. 424, no. 6950, pp. 824–830, Aug. 2003.

[35] T. Søndergaard and S. I. Bozhevolnyi, "Strip and gap plasmon polariton optical resonators," *physica status solidi (b)*, vol. 245, no. 1, pp. 9–19, 2008.

[36] J. A. Dionne, L. A. Sweatlock, H. A. Atwater, and A. Polman, "Planar metal plasmon waveguides: frequency-dependent dispersion, propagation, localization, and loss beyond the free electron model," *Phys. Rev. B*, vol. 72, no. 7, p. 075405, Aug. 2005.

[37] J. A. Dionne, L. A. Sweatlock, H. A. Atwater, and A. Polman, "Plasmon slot waveguides: Towards chip-scale propagation with subwavelength-scale localization," *Phys. Rev. B*, vol. 73, no. 3, p. 035407, Jan. 2006.

[38] L. Novotny and B. Hecht, *Principles of Nano-Optics*. Cambridge University Press, 2006.

[39] H. C. V. D. Hulst, *Light scattering: by small particles*. Courier Dover Publications, 1957.

[40] V. Giannini, A. I. Fernández-Domínguez, S. C. Heck, and S. A. Maier, "Plasmonic Nanoantennas: Fundamentals and Their Use in Controlling the Radiative Properties of Nanoemitters," *Chem. Rev.*, vol. 111, no. 6, pp. 3888–3912, Jun. 2011.

[41] S. Silver, *Microwave Antenna Theory and Design*. IET, 1949.

[42] C. A. Balanis, *Antenna Theory: Analysis and Design, 3rd Edition*, 3rd ed. Wiley-Interscience, 2005.

[43] W. L. Stutzman and G. A. Thiele, *Antenna Theory and Design, 2nd Edition*, 2nd ed. Wiley, 1997.

[44] S. Ramo, J. R. Whinnery, and T. V. Duzer, *Fields and Waves in Communication Electronics*, 3rd ed. John Wiley & Sons, Inc., 1994.

[45] H. Haus, *Waves and fields in optoelectronics*. Englewood Cliffs NJ: Prentice-Hall, 1984.

[46] R. E. Hamam, A. Karalis, J. D. Joannopoulos, and M. Soljaccaronicacute, "Coupled-mode theory for general free-space resonant scattering of waves," *Phys. Rev. A*, vol. 75, no. 5, p. 053801, May 2007.

[47] F. Wang and Y. R. Shen, "General Properties of Local Plasmons in Metal Nanostructures," *Phys. Rev. Lett.*, vol. 97, no. 20, p. 206806, Nov. 2006.

[48] E. Purcell, "Spontaneous emission probabilities at radio frequencies," in *Physical Review*, 1946, vol. 69, p. 681.

[49] P. Goy, J. M. Raimond, M. Gross, and S. Haroche, "Observation of Cavity-Enhanced Single-Atom Spontaneous Emission," *Phys. Rev. Lett.*, vol. 50, no. 24, pp. 1903–1906, Jun. 1983.

[50] Z. Zhang, L. Yang, V. Liu, T. Hong, K. Vahala, and A. Scherer, "Visible submicron microdisk lasers," *Applied Physics Letters*, vol. 90, no. 11, p. 111119, 2007.

[51] O. Painter, R. K. Lee, A. Scherer, A. Yariv, J. D. O'Brien, P. D. Dapkus, and I. Kim, "Two-Dimensional Photonic Band-Gap Defect Mode Laser," *Science*, vol. 284, no. 5421, pp. 1819 –1821, Jun. 1999.

[52] K. Nozaki, S. Kita, and T. Baba, "Room temperature continuous wave operation and controlled spontaneous emission in ultrasmall photonic crystal nanolaser," *Opt. Express*, vol. 15, no. 12, pp. 7506–7514, Jun. 2007.

[53] L. Novotny, "Effective Wavelength Scaling for Optical Antennas," *Phys. Rev. Lett.*, vol. 98, no. 26, p. 266802, Jun. 2007.

[54] W. Zhang, H. Fischer, T. Schmid, R. Zenobi, and O. J. F. Martin, "Mode-Selective Surface-Enhanced Raman Spectroscopy Using Nanofabricated Plasmonic Dipole Antennas," *The Journal of Physical Chemistry C*, vol. 113, no. 33, pp. 14672–14675, 2009.

[55] A. Alù and N. Engheta, "Input Impedance, Nanocircuit Loading, and Radiation Tuning of Optical Nanoantennas," *Phys. Rev. Lett.*, vol. 101, no. 4, p. 043901, Jul. 2008.

[56] A. Alu and N. Engheta, "Tuning the scattering response of optical nanoantennas with nanocircuit loads," *Nat Photon*, vol. 2, no. 5, pp. 307–310, May 2008.

[57] P. J. Schuck, D. P. Fromm, A. Sundaramurthy, G. S. Kino, and W. E. Moerner, "Improving the Mismatch between Light and Nanoscale Objects with Gold Bowtie Nanoantennas," *Phys. Rev. Lett.*, vol. 94, no. 1, p. 017402, Jan. 2005.

[58] D.-K. Lim, K.-S. Jeon, H. M. Kim, J.-M. Nam, and Y. D. Suh, "Nanogap-engineerable Raman-active nanodumbbells for single-molecule detection," *Nat Mater*, vol. 9, no. 1, pp. 60–67, Jan. 2010.

[59] W. Zhu, M. G. Banaee, D. Wang, Y. Chu, and K. B. Crozier, "Lithographically Fabricated Optical Antennas with Gaps Well Below 10 nm," *Small*, vol. 7, no. 13, pp. 1761–1766, 2011.

[60] A. Ahmed and R. Gordon, "Single Molecule Directivity Enhanced Raman Scattering using Nanoantennas," *Nano Lett.*, vol. 12, no. 5, pp. 2625–2630, May 2012.

[61] D. Wang, W. Zhu, Y. Chu, and K. B. Crozier, "High Directivity Optical Antenna Substrates for Surface Enhanced Raman Scattering," *Advanced Materials*, vol. 24, no. 32, pp. 4376–4380, 2012.

[62] D.-H. Kwon and D. M. Pozar, “Optimal Characteristics of an Arbitrary Receive Antenna,” *Antennas and Propagation, IEEE Transactions on*, vol. 57, no. 12, pp. 3720–3727, Dec. 2009.

[63] R. E. Collin, “Limitations of the Thevenin and Norton equivalent circuits for a receiving antenna,” *Antennas and Propagation Magazine, IEEE*, vol. 45, no. 2, pp. 119– 124, Apr. 2003.

[64] A. Alu and S. Maslovski, “Power Relations and a Consistent Analytical Model for Receiving Wire Antennas,” *Antennas and Propagation, IEEE Transactions on*, vol. 58, no. 5, pp. 1436–1448, May 2010.

[65] Y. Chu, M. G. Banaee, and K. B. Crozier, “Double-Resonance Plasmon Substrates for Surface-Enhanced Raman Scattering with Enhancement at Excitation and Stokes Frequencies,” *ACS Nano*, vol. 4, no. 5, pp. 2804–2810, May 2010.

[66] T. S. van Zanten, M. J. Lopez-Bosque, and M. F. Garcia-Parajo, “Imaging Individual Proteins and Nanodomains on Intact Cell Membranes with a Probe-Based Optical Antenna,” *Small*, vol. 6, no. 2, pp. 270–275, 2010.

[67] E. K. Lau, A. Lakhani, R. S. Tucker, and M. C. Wu, “Enhanced modulation bandwidth of nanocavity light emitting devices,” *Opt. Express*, vol. 17, no. 10, pp. 7790–7799, May 2009.

[68] A. Kinkhabwala, Z. Yu, S. Fan, Y. Avlasevich, K. Mullen, and MoernerW. E., “Large single-molecule fluorescence enhancements produced by a bowtie nanoantenna,” *Nat Photon*, vol. 3, no. 11, pp. 654–657, Nov. 2009.

[69] L. Novotny and N. van Hulst, “Antennas for light,” *Nature Photonics*, vol. 5, no. 2, pp. 83–90, 2011.

[70] T. J. Seok, A. Jamshidi, A. Lakhani, K. Yu, H. Choo, O. Miller, E. Yablonovitch, and M. C. Wu, “Characterization of Extended Width Optical Dipole Antennas,” in *Conference on Lasers and Electro-Optics*, 2010, p. CFI4.

[71] K. Ray, M. D. Mason, C. Yang, Z. Li, and R. D. Grober, “Single-molecule signal enhancement using a high-impedance ground plane substrate,” *Appl. Phys. Lett.*, vol. 85, no. 23, p. 5520, 2004.

[72] Q. Min, Y. Pang, D. J. Collins, N. A. Kuklev, K. Gottselig, D. W. Steuerman, and R. Gordon, “Substrate-based platform for boosting the surface-enhanced Raman of plasmonic nanoparticles,” *Opt. Express*, vol. 19, no. 2, pp. 1648–1655, Jan. 2011.

[73] Logeeswaran VJ, N. P. Kobayashi, M. S. Islam, W. Wu, P. Chaturvedi, N. X. Fang, S. Y. Wang, and R. S. Williams, “Ultrasmooth Silver Thin Films Deposited with a Germanium Nucleation Layer,” *Nano Letters*, vol. 9, no. 1, pp. 178–182, Jan. 2009.

[74] M. Fleischmann, P. J. Hendra, and A. J. McQuillan, “Raman spectra of pyridine adsorbed at a silver electrode,” *Chemical Physics Letters*, vol. 26, no. 2, pp. 163–166, May 1974.

[75] D. L. Jeanmaire and R. P. Van Duyne, “Surface raman spectroelectrochemistry: Part I. Heterocyclic, aromatic, and aliphatic amines adsorbed on the anodized silver electrode,” *Journal of Electroanalytical Chemistry and Interfacial Electrochemistry*, vol. 84, no. 1, pp. 1–20, Nov. 1977.

[76] K. Kneipp, Y. Wang, H. Kneipp, L. T. Perelman, I. Itzkan, R. R. Dasari, and M. S. Feld, “Single Molecule Detection Using Surface-Enhanced Raman Scattering (SERS),” *Phys. Rev. Lett.*, vol. 78, no. 9, p. 1667, Mar. 1997.

[77] S. Nie and S. R. Emory, “Probing Single Molecules and Single Nanoparticles by Surface-Enhanced Raman Scattering,” *Science*, vol. 275, no. 5303, pp. 1102 – 1106, Feb. 1997.

[78] D.-K. Lim, K.-S. Jeon, J.-H. Hwang, H. Kim, S. Kwon, Y. D. Suh, and J.-M. Nam, “Highly uniform and reproducible surface-enhanced Raman scattering from DNA-tailorable nanoparticles with 1-nm interior gap,” *Nat Nano*, vol. 6, no. 7, pp. 452–460, Jul. 2011.

[79] Y. Fang, N.-H. Seong, and D. D. Dlott, “Measurement of the Distribution of Site Enhancements in Surface-Enhanced Raman Scattering,” *Science*, vol. 321, no. 5887, pp. 388 –392, Jul. 2008.

[80] N. Félidj, J. Aubard, G. Lévi, J. R. Krenn, M. Salerno, G. Schider, B. Lamprecht, A. Leitner, and F. R. Aussenegg, “Controlling the optical response of regular arrays of gold particles for surface-enhanced Raman scattering,” *Phys. Rev. B*, vol. 65, no. 7, p. 075419, Feb. 2002.

[81] Y. Chu and K. B. Crozier, “Experimental study of the interaction between localized and propagating surface plasmons,” *Opt. Lett.*, vol. 34, no. 3, pp. 244–246, Feb. 2009.

[82] L. Rodríguez-Lorenzo, R. de la Rica, R. A. Álvarez-Puebla, L. M. Liz-Marzán, and M. M. Stevens, “Plasmonic nanosensors with inverse sensitivity by means of enzyme-guided crystal growth,” *Nature Materials*, vol. 11, no. 7, pp. 604–607, 2012.

[83] R. de la Rica and M. M. Stevens, “Plasmonic ELISA for the ultrasensitive detection of disease biomarkers with the naked eye,” *Nature Nanotechnology*, 2012.

[84] K. Kumar, H. Duan, R. S. Hegde, S. C. W. Koh, J. N. Wei, and J. K. W. Yang, “Printing colour at the optical diffraction limit,” *Nature Nanotechnology*, vol. 7, no. 9, pp. 557–561, 2012.

[85] N. R. Jana, L. Gearheart, and C. J. Murphy, “Evidence for Seed-Mediated Nucleation in the Chemical Reduction of Gold Salts to Gold Nanoparticles,” *Chem. Mater.*, vol. 13, no. 7, pp. 2313–2322, Jul. 2001.

[86] D. Morecroft, J. K. W. Yang, S. Schuster, K. K. Berggren, Q. Xia, W. Wu, and R. S. Williams, “Sub-15 nm nanoimprint molds and pattern transfer,” 2009, vol. 27, pp. 2837–2840.

[87] J. Zhao, J. A. Dieringer, X. Zhang, G. C. Schatz, and R. P. Van Duyne, “Wavelength-Scanned Surface-Enhanced Resonance Raman Excitation Spectroscopy,” *J. Phys. Chem. C*, vol. 112, no. 49, pp. 19302–19310, Dec. 2008.

[88] Y.-K. Choi, T.-J. King, and C. Hu, “A spacer patterning technology for nanoscale CMOS,” *IEEE Transactions on Electron Devices*, vol. 49, no. 3, pp. 436 – 441, Mar. 2002.

[89] Y.-K. Choi, J. Zhu, J. Grunes, J. Bokor, and G. A. Somorjai, “Fabrication of Sub-10-nm Silicon Nanowire Arrays by Size Reduction Lithography,” *J. Phys. Chem. B*, vol. 107, no. 15, pp. 3340–3343, Apr. 2003.